2022

CHARACTERIZING RIVERINE CARBON: A SPATIOTEMPORAL STUDY OF ORGANIC AND INORGANIC CARBON VARIABILITY AND EVALUATION OF METHODS FOR QUANTIFYING pCO2

Fischer Larson Young

Recommended Citation

Young, Fischer Larson, "CHARACTERIZING RIVERINE CARBON: A SPATIOTEMPORAL STUDY OF ORGANIC AND INORGANIC CARBON VARIABILITY AND EVALUATION OF METHODS FOR QUANTIFYING pCO2" (2022). *Graduate Student Theses, Dissertations, & Professional Papers*. 12023.
https://scholarworks.umt.edu/etd/12023

CHARACTERIZING RIVERINE CARBON: A SPATIOTEMPORAL STUDY OF ORGANIC AND INORGANIC CARBON VARIABILITY AND EVALUATION OF METHODS FOR QUANTIFYING pCO_2

By

FISCHER LARSON YOUNG

B.S. Environmental Science, Western Washington University, Bellingham, Washington, 2016

Dissertation

presented in partial fulfillment of the requirements
for the degree of

Doctor of Philosophy
in Chemistry, Analytical/Environmental

The University of Montana
Missoula, MT

December 2022

Approved by:

Ashby Kinch,
Graduate School Dean

Dr. Michael DeGrandpre, Chair
Department of Chemistry and Biochemistry

Dr. Chris Palmer
Department of Chemistry and Biochemistry

Dr. Lu Hu
Department of Chemistry and Biochemistry

Dr. H. Maurice Valett
Department of Biological Sciences

Dr. Ben Colman
Department of Ecosystem and Conservation Science

Young, Fischer L., Ph.D., Autumn 2022 *Chemistry, Analytical/Environmental*

Characterizing Riverine Carbon: A spatiotemporal study of organic and inorganic carbon variability and evaluation of methods for quantifying pCO_2

Chairperson: Dr. Michael DeGrandpre

Carbon is a critical component of aquatic ecosystems. For inland waters, carbon is a basal resource for biological communities and is a key component of trophic transfer through ingestion and respiration processes. Additionally, carbon acts as a key biogeochemical tracer that can track chemical, physical, and biological processes from the terrestrial landscape to inland waters to the ocean. Riverine carbon, however, can be challenging to characterize and interpret due to the complexity of its sources and sinks along a riverine continuum. Included in this work are the biogeochemically relevant forms of carbon such as dissolved inorganic carbon (DIC), the partial pressure of carbon dioxide (pCO_2), and dissolved organic carbon (DOC). Together, these forms of carbon along with spectrophotometric pH, temperature, total alkalinity, and ionic strength were measured and analyzed to evaluate a novel method for quantifying freshwater pCO_2 and to assess the spatial and temporal variability of inorganic and organic carbon along the upper Clark Fork River (UCFR), MT, USA.

Overall, the method for calculating pCO_2 showed a ~4-fold improvement in accuracy, compared to an infrared reference, when using an indicator-based pH instead of electrochemical pH. Moreover, this method was validated through a 19-d field application in the UCFR. This method was then used to calculate pCO_2 on 275 discrete samples to estimate the air-water CO_2 flux along the UCFR. The UCFR was a source of CO_2 to the atmosphere with a river-wide average air-water CO_2 flux of 80 ± 140 mmol m^{-2} d^{-1} ($n = 275$). The magnitude of the air-water CO_2 flux was primarily driven by riverine pH, discharge, and season. Additionally, DOC variability along the UCFR was assessed through the Carbon Processing Domain framework where stream reaches were designated by functional space. DOC dynamics were strongly linked to changes in discharge, characteristic of a snowmelt dominated system, where reaches along the UCFR occupied diluter, enhancer, compiler, conduit, and consumer domains dependent on season, reach, and hydraulic loads. This work characterized the carbon dynamics of ~215 km of the UCFR from ~3500 discrete samples over 4 years to better understand carbon sources, sinks, and variability along the UCFR.

Acknowledgements

Through this journey and pursuit of knowledge there are dozens of individuals I would like to thank. Foremost, I thank my research advisor, Dr. Michael DeGrandpre for his support, candor, guidance, and for taking a chance on me when I first joined the Chemistry Department. He has helped me develop both broad and specific skillsets that will aid me in my future endeavors for which I am immensely grateful. His flexibility and trust in me to work from home from the start of the COVID-19 pandemic through the completion of my degree allowed me to take an active role in parenting my two young children—time I would have lost otherwise. Thank you.

Cory Beatty and Qipei Shangguan, thank you for your day-to-day help from sensor deployments to laboratory troubleshooting to whiteboard discussions and keeping me company on those long days and nights in lab. I also had the privilege of meeting and talking with other DeGrandpre group members as they were leaving/graduating. Thank you to them for their advice and help getting my feet underneath me as I started this adventure.

Thank you to everyone (past and present) that I had the privilege of engaging with in the Dr. Maury Valett and Dr. Ben Colman laboratories. I really felt a sense of community between our three labs that I will always cherish and remember fondly. A special thanks to Claire Utzman for being a great friend, work colleague, and for helping organize sampling events that led to much of the data in this dissertation. Additionally, a special thanks to Dr. Maury Valett and Dr. Ben Colman for their continued support, countless discussions, and allowing me to use their laboratories and lab vehicles to analyze and collect samples, respectively.

Thank you to Dr. Chris Palmer and Dr. Lu Hu for their continued support, guidance, advice, and perspectives during my degree program that helped develop my skills as an independent researcher. Also thank you to Dr. Juliana D'Andrilli, Dr. Marc Peipoch, and Dr. Rob Payn for stimulating discussions and for helping shape me into the scientist I am today. Thank you to all my friends and family, far and wide, for their loving support; and to my mother, father, and sister for always being there and believing in me. You all helped me get here.

Lastly, and arguably most importantly, I would like to thank my family – Josie, Maisie, and Freyja. Josie, raising two kids together while I pursued a doctoral degree (with a global pandemic in the middle) was no easy feat. I am grateful that I had you to help navigate those waters. Thank you for your unwavering patience, love, and respect for me that drove me to the finish line. I am forever in your debt. Maisie and Freyja, thank you for loving me so deeply and for being the strong-willed goofballs that you are. Your comedic relief in a time that was so uncertain for so long meant the world to me; please do not ever change.

Table of Contents

Page #

Chapters

IV. Carbon Processing Domains: Seasonal and spatial controls on organic carbon in a montane river……………………………………………………………..67

List of Figures

Appendix A

Appendix B

Appendix C

List of Tables

Appendix A

Appendix C

Code

Appendix A

Chapter 1

Introduction

Overview

Carbon is a critical component of aquatic ecosystems. For inland waters, carbon is generally categorized into two primary groups: inorganic carbon and organic carbon. These groups can be further divided into particulate, colloidal, and dissolved fractions. However, for the work described here only dissolved forms of inorganic and organic carbon are described. Dissolved inorganic carbon (DIC) includes key chemical species such as carbon dioxide (CO_2), bicarbonate (HCO_3^-), and carbonate (CO_3^{-2}) (Stumm and Morgan, 2008; Middleburg, 2019). These species originate from the dissolution of geogenic sources (i.e., limestone), air-water gas exchange with the atmosphere, and from the biologically mediated oxidation of organic matter (i.e., heterotrophic, and autotrophic respiration). Dissolved organic carbon (DOC) in inland waters is either produced from endogenous processing (i.e., photosynthetic exudates) or is brought to the system via exogenous transport (i.e., transport of terrestrially sourced organic matter). DOC is a basal resource for biological communities and is a key component of trophic transfer (Drakare et al. 2002). As such, DIC and DOC are critical components of aquatic ecosystems as they elucidate several important biogeochemical processes including metabolism, gas exchange, floodplain connectivity, and hydrologic transport.

In addition to their ecological importance, these carbon pools are a significant part of the global carbon budget (Raymond et al. 2000; Cole et al. 2007; Raymond et al. 2013; Hotchkiss et al. 2015). The focus on these systems is attributed to the continued progression of climate change (IPCC, 2022) and the fraction to which inland waters have been shown to contribute key greenhouse gases (GHG), namely carbon dioxide (CO_2) and methane (CH_4), to the atmosphere (Choi et al. 1998; Cole and Caraco, 2001; Duvert et al. 2018; Rocher-Ros et al. 2020; Karlsson et al. 2021). Raymond et al. (2013) provides an estimate of global air-water CO_2 flux from inland waters to be 1.8 Pg C yr^{-1} while current estimates of global riverine DOC and DIC fluxes to the coastal oceans are 0.24 and 0.41 Pg C yr^{-1}, respectively (Li et al. 2017). Thus, indicating the relative importance of inland carbon cycling to the global carbon budget and that continued research of freshwater carbon dynamics and GHGs is needed as climate change progresses at an unprecedented rate (IPCC, 2022).

Due to the dynamic nature of inland waters, inorganic carbon parameters vary spatially and temporally due to changes in allochthonous inputs, floodplain connectivity, gas exchange, and instream processing (Raymond et al. 1997; Worrall and Lancaster, 2005; Parker et al. 2007; Lynch et al. 2010; Rocher-Ros et al. 2019; Shangguan et al. 2021). DIC, pH, A_T, and the partial pressure of CO_2 (pCO_2) often have strong diel (24-hr) cycles that follow sunlight, temperature, and primary productivity (Lynch et al. 2010; Shangguan et al. 2021). These diel cycles have characteristically large ranges, spanning hundreds of μatm and μmol L^{-1} for pCO_2 and DIC, A_T, respectively, while the diel pH range can be over one pH unit (Shangguan et al. 2021; Young et al. 2022). Additionally, seasonal and interannual variability also illicit strong responses in these parameters due to changes in river discharge, temperature, groundwater and tributary influences, sunlight, nutrients, and the succession of primary producers (Raymond et al. 2000; Lynch et al. 2010; Cory et al. 2014; Peter et al. 2014; Minor et al. 2019). Furthermore, this temporal variability in inorganic carbon is compounded by spatial differences driven by similar processes (i.e., river discharge, temperature, allochthonous inputs, and primary production).

Processes that impact the dynamics of inorganic carbon in rivers, discussed above, can also drive DOC dynamics. For example, many studies have shown that discharge is a key driver of DOC variability and significantly controls the flux of DOC from the terrestrial landscape to the river (Evans and Davies, 1998; Godsey et al. 2009; Mast et al. 2016; Raymond et al. 2016; O'Donnell and Hotchkiss, 2019; Shogren et al. 2021). Further, the magnitude of DOC loading to a system (e.g., volumetric flow multiplied by concentration) can depend on antecedent floodplain conditions, such as droughts (Tunaley et al. 2016). Similar to inorganic carbon, DOC has also been shown to have a diel cycle in freshwater systems due to photo-oxidation, biological uptake and release, and temperature (Spencer et al. 2007; Parker et al. 2010; Tunaley et al. 2016; Johnson, 2021; Oviedo-Vargas et al. 2022). The diel cycle of DOC, however, seems to be less predictable than the diel cycle of inorganic carbon where DOC could have no peaks during 24-hr or multiple (Spencer et al. 2007; Johnson, 2021). Additionally, the diel range of DOC in freshwater systems, if present at all, is relatively small compared to inorganic carbon with a range of ~80 to ~300 μmol L^{-1} in temperate systems (Kaplan and Bott, 1982; Spencer et al. 2007; Parker et al. 2010; Johnson, 2021; Oviedo-Vargas et al. 2022). Seasonal changes in DOC, however, can be significantly larger than diel DOC variability (e.g., ~200 to ~1300 μmol L^{-1} from winter to spring; Mast et al. 2016). Additionally, spatial differences in biological communities and the quality of DOC also contribute to its variability in freshwater systems (D'Andrilli et al. 2015; Brailsford et al. 2019). A recent study by Valett et al. (2022) outlines a budgetary approach, known as Nutrient Processing Domains, geared towards providing insight into both discharge-driven processes and in situ biological uptake. The work presented in Chapter 4 employs this approach for DOC to better interpret its spatial and temporal variability and what biogeochemical process(es) significantly controls that variability.

Advancements in quantifying riverine carbon

Issues exist, however, for characterizing inorganic carbon dynamics in freshwater systems. Such issues include accurately quantifying the gas transfer velocity and dissolved CO_2 (i.e., $p$$CO_2$). Recent studies have outlined techniques to better estimate gas transfer velocities using the open-source R program, *streamMetabolizer* (Appling et al. 2018b). This approach utilizes a Bayesian statistical model to estimate gas transfer velocity from high-resolution in situ dissolved oxygen data. Conversely, issues with accurately calculating $p$$CO_2$ from pH and total alkalinity (A_T) in freshwater has been documented in several studies (Hunt et al. 2011, Abril et al. 2015, Liu et al. 2020; Young et al. 2022). To avoid issues involved with its calculation, $p$$CO_2$ can be measured directly using in situ sensors (Parker et al. 2007; Lynch et al. 2010; Rocher-Ros et al. 2020) or headspace equilibrium techniques coupled to nondispersive infrared (NDIR) analysis or gas chromatography (Cole and Caraco, 2001; Abril et al. 2015; Rocher-Ros et al. 2019; Aho et al. 2021). However, obtaining direct measurements of $p$$CO_2$ can be expensive and so most studies have relied on the analysis of collected samples. Thus, the work presented here details a novel methodological approach for accurately calculating freshwater $p$$CO_2$ from spectrophotometric pH and A_T (Young et al. 2022). Outlined in this approach is the consideration of freshwater ionic strength (μ) (commonly assumed to be negligible in freshwater systems, Hunt et al. 2011; Abril et al. 2015) for calculating pH, thermodynamic equilibrium constants, and $p$$CO_2$ (Young et al. 2022). As a result, these accurately calculated $p$$CO_2$ values can be used along with high quality gas transfer velocities estimated from *streamMetabolizer* to obtain accurate air-water CO_2 flux estimates based on discrete samples.

Compared to DIC, DOC is relatively simple to collect and analyze. Methods for its quantification and its quality characterization have been established for many years (U.S. EPA, 2005; Holmes et al. 2008; Dai et al. 2012; D'Andrilli et al. 2015). DOC concentrations are typically measured by acidifying sample with sulfuric acid and heating it with persulfate (U.S. EPA, 2005). This process oxidizes organic carbon into CO_2 which is then detected with an NDIR detector. Further, DOC cannot be measured in situ via autonomous sensor and instead is typically manually sampled and analyzed in a laboratory as described above. However, higher resolution proxy measures of DOC can be obtained from measures of fluorescent or colored dissolved organic matter from in situ spectrophotometers (i.e., s::can Spectrolyser UV-Vis, Messtechnik GmbH, Austria; Vaughan et al. 2017).

Study system

The work presented throughout this dissertation took place along the upper Clark Fork River (UCFR) located in Montana, USA. The UCFR is the ~215 km upper portion of the Clark Fork River (total length is ~500 km) with ongoing floodplain restoration with a legacy of heavy metal pollution produced by more than 125 years of copper and silver mining and smelting activities (Moore and Luoma, 1990; Nagorski, 2001; Parker et al. 2007; Moore and Langner, 2012). It is a productive, mid-order river characterized as a snowmelt dominated catchment (Moore and Luoma, 1990; Lynch et al. 2010; Moore and Langner, 2012). Further specifics regarding descriptions, sampling locations, and reaches are described in detail in each of the subsequent chapters.

The numerous studies referenced above have provided a vast amount of information regarding inorganic and organic carbon variability. However, few studies have had the time and resources to measure carbon variability along ~215 km of a single river for multiple years at daily, monthly, seasonal, and annual time scales. The study presented here provides inorganic and organic carbon information from roughly 4 years (48 months, 65 sampling events) for 13 mainstem and 3 tributary sampling locations along the upper Clark Fork River (UCFR), MT, USA. Approximately 5,600 total discrete data points and ~1700 high resolution autonomous sensor data points have been collected and calculated over this study period and spatial gradient. Of this dataset, ~3,500 discrete data points were used in the work described below. Complete records of the data are published on the Environmental Data Initiative (EDI) repository and are publicly available (DeGrandpre and Young, 2021a, 2021b, 2021c; DeGrandpre et al. 2021a, 2021b, 2021c; Young et al. 2022). The parameters included in this subset of data are A_T, pH, DIC, pCO$_2$, air-water CO$_2$ flux, DOC, and ancillary measurements (i.e., temperature, specific conductivity, μ) to better understand inorganic and organic carbon variability along the UCFR.

This dissertation is organized around three manuscripts focused on a methodological approach for calculating freshwater pCO$_2$ (Chapter 2) as well as the quantification and interpretation of freshwater inorganic carbon (Chapter 3) and organic carbon (Chapter 4) spatiotemporal variability. The methodological approach for calculating freshwater pCO$_2$ (Chapter 2) has been published in the journal *Limnology and Oceanography: Methods* and its reference is available in the *References* section (Young et al. 2022). The second manuscript focused on freshwater inorganic carbon and air-water CO$_2$ flux variability is under internal revision as part of the dissertation review. Additionally, the third manuscript focused on the spatial and temporal variability of freshwater DOC using the Carbon Processing Domain approach (Valett et al. 2022) is in advanced draft form. The appendices located at the end of this dissertation (Appendix A, B, and C) are analogous to the supplemental information document submitted alongside a manuscript for peer-review. Additional graphics and tables, however, have been included to provide further support for each chapter.

Chapter 2

Comparison of spectrophotometric and electrochemical pH measurements for calculating freshwater pCO_2

Introduction

Inland waters process and transport substantial amounts of terrestrially derived carbon (Hotchkiss et al. 2015). Most streams and rivers are sources of carbon dioxide (CO_2) to the atmosphere (Raymond et al. 2000; Wang and Cai, 2004; Chen et al. 2012), where they represent a substantial component in the global carbon cycle (Cole et al. 2007; Raymond et al. 2013; Hotchkiss et al. 2015). A common way of evaluating the magnitude of these CO_2 sources is by calculating the CO_2 exchange over a given area of freshwater (i.e., flux). Current challenges in quantifying air-water CO_2 fluxes include obtaining accurate gas transfer velocities and accurately quantifying dissolved CO_2, usually reported as the partial pressure of CO_2 (pCO_2) (Raymond et al. 2012; Duvert et al. 2018; Rocher-Ros et al. 2019; Ulseth et al. 2019). Recent studies have outlined techniques to increase the accuracy of gas transfer velocities (Appling et al. 2018a, 2018b; Rocher-Ros et al. 2021); however, debates continue about the best practices for obtaining accurate freshwater pCO_2 (Hunt et al. 2011; Abril et al. 2014; Liu et al. 2020).

Currently, freshwater pCO_2 is either measured directly or calculated. Researchers measure pCO_2 directly using in situ sensors (e.g., Parker et al. 2007; Lynch et al. 2010; Rocher-Ros et al. 2020) or headspace equilibrium techniques coupled to nondispersive infrared (NDIR) analysis or gas chromatography (Cole and Caraco, 2001; Johnson et al. 2009; Åberg and Wallin, 2014; Abril et al. 2015; Rocher-Ros et al. 2019; Aho et al. 2021). However, most freshwater studies rely on analysis of collected samples. The pCO_2 is then calculated from any two quantifiable inorganic carbon parameters i.e., total alkalinity (A_T), pH, or dissolved inorganic carbon (DIC). The two measured parameters are input into an equilibrium model that uses proton (i.e., A_T) and mass (i.e., DIC) balances and the thermodynamic equilibria for carbonic acid (H_2CO_3) (e.g., CO2SYS or PHREEQC) (Choi et al. 1998; Lewis and Wallace, 1998; Butman and Raymond, 2011; Parkhurst and Appelo, 2013; Abril et al. 2014, 2015).

Both A_T and pH are commonly monitored by government and research agencies around the world (Raymond et al. 2013; Stets et al. 2017; Wen et al. 2017; Coles et al. 2019; Liu et al. 2020) and these long-term datasets have been used to calculate $p\text{CO}_2$ and estimate global CO_2 emissions (Cole et al. 2007; Aufdenkampe et al. 2011). Studies have shown, however, that using A_T and electrochemical pH can result in overestimation of calculated $p\text{CO}_2$ leading to inflated estimates of global freshwater CO_2 emissions (Herczeg and Hesslein, 1984; Hunt et al. 2011; Abril et al. 2015; Liu et al. 2020). Freshwater $p\text{CO}_2$ can be overestimated by 10 to >100% when calculated from pH and A_T (Hunt et al. 2011; Abril et al. 2015; Liu et al. 2020). These erroneously high $p\text{CO}_2$ values are thought to be caused by systematically low electrode pH and the presence of non-carbonate species (e.g., organic acid anions) that can contribute to higher A_T values. This "excess A_T" overestimates $p\text{CO}_2$ because carbonate equilibrium models assume that freshwater A_T is all carbonate alkalinity. Other chemical species, like phosphate, could also contribute to A_T but are typically at negligible concentrations in freshwater compared to carbonate concentrations. Findings from Liu et al. (2020) revealed that organic acids can be a significant portion of A_T when A_T is less than ~1000 $\mu\text{mol L}^{-1}$ with errors in calculated $p\text{CO}_2$ of >40%. This error is significantly reduced (<8%), however, at higher A_T (e.g., >2000 $\mu\text{mol L}^{-1}$; Liu et al. 2020). Additionally, Liu et al. (2020) suggested empirical relationships based on ionic strength (μ) and dissolved organic carbon (DOC) to correct past electrochemical pH and A_T measurements, respectively. Even with the pH measurement correction, $p\text{CO}_2$ error was only reduced by ~40% (Liu et al. 2020), so there remains a need for more accurate pH measurements and more rigorous thermodynamic calculations of $p\mathrm{CO_2}$.

The inaccuracy of pH electrodes in freshwater is primarily due to changes in the liquid junction potential (Illingworth 1981; Herczeg and Hesslein, 1984; Davison and Woof, 1985; Stauffer, 1990; Raymond et al. 1997). Calibration of an electrode in standard buffer solutions (i.e., National Institute of Standards and Technology (NIST)) that have higher μ than freshwater (i.e., μ >0.01 M) commonly leads to systematically low pH in low μ conditions (Herczeg and Hesslein, 1984; Byrne et al. 1988; French et al. 2002; Liu et al. 2020). Spectrophotometric pH, which uses a colorimetric indicator to determine pH, has demonstrated improved accuracy compared with glass electrodes (Byrne et al. 1988; Yao and Byrne, 2001; French et al. 2002; Yuan and DeGrandpre, 2008; DeGrandpre et al. 2014; Lai et al. 2016; Minor et al. 2019). The accuracy has been reported to be <0.008 pH units for freshwater applications (Yuan and DeGrandpre 2008; Lai et al. 2016). Although spectrophotometric pH is commonly used for calculation of $p\mathrm{CO_2}$ in seawater where its utility has been extensively characterized (Byrne et al. 1988; Zhang and Byrne, 1996; Lueker et al. 2000; Byrne et al. 2010; DeGrandpre et al. 2014; Bockmon and Dickson, 2015; Takeshita et al. 2020), it has not been significantly used for calculation of freshwater $p\mathrm{CO_2}$ or for that matter, calculation of other freshwater equilibria (e.g., solubility). Freshwater measurements of spectrophotometric pH pose unique challenges, however, because of the uncertainty of μ effects and the potential perturbation of pH of poorly buffered freshwater by addition of indicator (Yuan and DeGrandpre, 2008). Therefore, it is important to evaluate the utility of spectrophotometric pH measurements more thoroughly for freshwater applications, especially for its use in calculating $p\mathrm{CO_2}$.

The recent availability of purified meta-cresol purple (*p*mCP) and characterization of its equilibrium constant at low μ has made this evaluation more opportune (Lai et al. 2016) where pH accuracy might vary due to different mCP impurities in commercial products (Liu et al. 2011). Over a decade ago, marine chemists discovered that dye impurities degrade the accuracy of seawater pH measurements and demonstrated improved accuracy by purifying the indicator (Yao et al. 2007; Liu et al. 2011). The effects of dye impurities on freshwater measurements have never been determined and so the uncertainty created by this problem has likely compromised the appeal of indicator-based pH measurements for freshwater. Additionally, μ is integral to this assessment because it can alter the inorganic carbon equilibria, i.e., the apparent dissociation constants increase with increasing μ (Stumm and Morgan, 2008). The effect of μ on freshwater CO_2 calculations has not been rigorously evaluated, however. Additionally, μ encompasses a range from ~0.1 mM to >10 mM in freshwater systems (Cormier et al. 2013), a range that significantly changes the apparent Henry's Law constant (K_H'), apparent dissociation constants (K_1', K_2', and K_W') and, as a result, calculated $p\mathrm{CO}_2$. Therefore, rigorously accounting for freshwater μ could improve carbonate equilibrium models and, accordingly, calculated $p\mathrm{CO}_2$ values.

To evaluate the freshwater applicability of spectrophotometric pH measurements, a laboratory study was conducted to compare spectrophotometric and electrochemical pH measurements for calculating freshwater $p\mathrm{CO}_2$ over a wide range of conditions (i.e., μ, A_T, and temperature). The experiments used a test tank where the $p\mathrm{CO}_2$ could be monitored while samples were simultaneously obtained for pH and A_T. Further, high frequency in situ spectrophotometric pH measurements were made in a local river to evaluate the accuracy of calculating $p\mathrm{CO}_2$ through a real-world application.

Materials and procedures

Laboratory tank study

Overview

A 130-L, temperature-controlled, well-mixed tank of a mixture of tap water and deionized (DI) water was sampled with $p\mathrm{CO_2}$ ranging from ~100-1600 µatm. The $p\mathrm{CO_2}$ levels were varied by 1) introducing air that was passed through a column of soda lime (Fisher Scientific, CAS # 8006-28-8) to drive the $p\mathrm{CO_2}$ below atmospheric levels (~100-400 µatm) or 2) introducing small volumes of high $\mathrm{CO_2}$ into the test tank headspace to increase the $p\mathrm{CO_2}$. A range of A_T from ~1800-3200 µmol L^{-1} and μ from ~5-9 mmol L^{-1} were created by dilution of tap water (undiluted tap water A_T = ~3200 µmol L^{-1}) in the tank with DI water. The tank temperature was set to 10, 15, or 20 °C. Most data were collected at 15 ºC with a limited number of measurements made at 10 and 20 ºC to determine performance over a broader temperature range. These conditions are like those found in a nearby river, the Clark Fork River (CFR), MT, USA, where we have worked extensively (Parker et al. 2007; Lynch et al. 2010; Shangguan et al. 2021), and other temperate and tropical freshwater rivers (Abril et al. 2015).

The tank $p\mathrm{CO_2}$ was quantified using a membrane equilibrator (Membrana, Liqui-Cel SP Series) attached to a pump and a $\mathrm{CO_2}/\mathrm{H_2O}$ infrared gas analyzer (LI-COR, LI-840A). The gas analyzer was zeroed with $\mathrm{CO_2}$-free air and then calibrated with two $\mathrm{CO_2}$ standards (359 and 1774 ppm) (Dickson et al. 2007). Sample collection began at the lowest $p\mathrm{CO_2}$ concentration in the test tank (~100 µatm) and continued sequentially in ~150-200 µatm steps until ~1600 µatm. The $p\mathrm{CO_2}$ was recorded on a one-minute interval and the measured mole fraction of $\mathrm{CO_2}$ was converted to $p\mathrm{CO_2}$ following Dickson et al. (2007). The overall tank $p\mathrm{CO_2}$ accuracy is estimated to be ~±5 µatm.

Samples for analysis of A_T and pH were collected to coincide with the equilibrator-infrared measurements. Triplicate samples were dispensed via a pump from the closed test tank to maintain $p\mathrm{CO}_2$ levels. Samples were collected in borosilicate glass bottles secured with greased hollow glass stoppers. The samples were kept on ice for ~5-15 min until spectrophotometric pH and A_T analysis. For the pH electrode measurements, two additional samples (one for each pH electrode measurement) were collected immediately after the previously mentioned triplicate samples and analyzed within 1-2 minutes of sample collection.

Spectrophotometric pH

Spectrophotometric pH measurements were made using a double beam spectrophotometer (Agilent, Cary 300) with 10 cm borosilicate glass cuvettes and temperature regulated cuvette holders (Lai et al. 2016). Each bottle was analyzed only once to prevent an increase in headspace that could allow gas exchange and alter the pH and $p\mathrm{CO}_2$. Triplicate spectrophotometric pH measurements were averaged for further analysis.

For freshwater pH analysis, *p*mCP was used because the negative logarithm of its acid dissociation constant (pK_a) is equal to 8.6607 at 25 ^{0}C at infinite dilution (μ = 0 mM) (Lai et al. 2016) and overlaps with the pH range observed in the CFR (e.g., 7.9 to 9.1) (Parker et al. 2007) and many other alkaline freshwater systems (Peter et al. 2014). The pK_a for purified phenol red has also been quantified at low μ and would be suitable for a lower pH range (pK_a = 8.0625 at 25 ^{0}C at infinite dilution) (Lai et al. 2016). Automated diagnostic checks were performed monthly on the spectrophotometer that included validation of wavelength accuracy, wavelength reproducibility, photometric noise, and baseline flatness, some of which have been shown to affect spectrophotometric pH measurement accuracy (DeGrandpre et al. 2014).

Spectrophotometric pH measurements were calculated on the free hydrogen ion scale ($pH_{free} = -\log[H^+]$, where $[H^+]$ is the hydrogen ion concentration) using the following equation (Yao and Byrne, 2001; Lai et al. 2016):

$$\mathrm{pH_{free}} = \mathrm{pK_a} + \log(\frac{\mathrm{R} - \mathrm{e_1}}{\mathrm{e_2} - \mathrm{Re_3}}) - 4\mathrm{A}(\frac{\sqrt{\mu}}{1 + \sqrt{\mu}} - 0.3\mu) \qquad (1)$$

where pK_a is the temperature dependent negative logarithm of the second dissociation constant of *p*mCP at infinite dilution. The indicator (I) *p*mCP exists in two forms in natural waters, the protonated (acid) form, HI^-, and the deprotonated (base) form, I^{2-}. Thus, R is the ratio of indicator absorbances (A_{578}/A_{434}) at the absorbance maxima of I^{2-} (578 nm) and HI^- (434 nm), e_1, e_2, and e_3 refer to the molar absorption coefficient ratios corresponding to HI^- and I^{2-} at 434 nm and 578 nm, and

$$\mathrm{A} = 0.5092 + (\mathrm{T} - 298.15) \times 8.5 \times 10^{-4} \qquad (2)$$

where T is the temperature in Kelvin. Due to minor changes in pH of the sample caused by the addition of indicator (Seidel et al. 2008; Yuan and DeGrandpre, 2008; Li et al. 2020), pH was calculated using a linear regression of the pH values recorded with addition of three 80 µL indicator aliquots. The magnitude of this perturbation correction was -0.005 ± 0.004 pH units (*n* = 84), similar to previously reported perturbation corrections (Yuan and DeGrandpre, 2008). This procedure gave absorbances within a range of 0.0930 to 1.4740. Example pH values with relevant parameters (i.e., molar absorptivity, absorbance, temperature, and pK_a) are summarized in Appendix A (Table S1). All sample measurements were temperature corrected to the tank water temperature using the equilibrium model CO2SYS (Lewis and Wallace, 1998) at infinite dilution (Millero 1979). This program uses an input (measurement) and output (tank) temperature, alkalinity, and input pH. Temperature corrections averaged -0.005 ± 0.004 pH units. The resulting temperature corrected pH was used for subsequent pCO_2 calculations and pH comparisons (see below). Additionally, pH values from the spectrophotometer were compared bimonthly to an NIST traceable phosphate buffer (pH 8.00 ± 0.02 at 25.1 ± 0.3 °C, μ = ~0.2 M) (Micro Essential Laboratory, Inc., Hydrion). The spectrophotometric pH measurements were converted to the National Bureau of Standards (NBS) scale (pH_{NBS}) (see below), and temperature corrected to 25.0 °C. Measurements showed good agreement with the pH buffer (average error of -0.006 ± 0.02 pH units, n = 12, at 25.1 ± 0.3 °C).

All spectrophotometric pH_{free} measurements were converted to pH_{NBS} using Eq. 3 (Stumm and Morgan 2008) to make them directly comparable with the electrochemical pH_{NBS} data. Note that in Eq. 3, z is equal to 1 (i.e., charge of the hydrogen ion).

$$\mathrm{pH_{NBS}} = \mathrm{pH_{free}} + \mathrm{A}z^2\left(\frac{\sqrt{\mu}}{1+\sqrt{\mu}} - 0.3\mu\right) \tag{3}$$

Eq. 3 indicates that pH_{free} and pH_{NBS} are related by the Davies term (i.e., $\mathrm{A}z^2(\frac{\sqrt{\mu}}{1+\sqrt{\mu}} - 0.3\mu)$). At zero ionic strength both pH values are equal; however, as ionic strength increases, the Davies term also increases, and consequently, pH_{NBS} becomes greater than pH_{free}.

Tap water ionic strength was determined assuming the reported average ion concentrations from the Missoula aquifer (AWQR 2020; Appendix A, Table S2) and using the following equation (Stumm and Morgan, 2008):

$$\mu = \frac{1}{2}\sum(c_i z_i^2) \tag{4}$$

where c_i and z_i are the concentration and charge of an ionic species, respectively. To determine the diluted tap water μ, we used a dilution factor derived from the undiluted and diluted specific conductivity and μ. Conductivity was measured using an in situ conductivity data logger (HOBO, Onset U24 Freshwater). The conductivity logger was calibrated with a 1000 $\mu S\ cm^{-1}$ conductivity standard (Bicca, Catalog # 2237). Discrete measurements of conductivity were also taken for quality control using a handheld water quality meter (YSI Inc., Pro1030), hereafter referred to as the YSI, that was calibrated in the same way as the in situ conductivity sensor. The undiluted and diluted calculated μ were used for all pH (Eqs. 1 and 3) and $p\mathrm{CO}_2$ calculations as described below.

Electrochemical pH

Glass pH electrode measurements were made with two different electrodes: 1) an electrode commonly used for pH measurements in the field (YSI Inc., Pro1030) and 2) a laboratory grade pH electrode (Metrohm AG, Ecotrode Plus), hereafter referred to as Metrohm. Both electrodes were calibrated with 4.00, 7.00, and 10.00 NIST traceable pH buffers (Micro Essential Laboratory, Inc., Hydrion) to align with literature methods (Hunt et al. 2011; Abril et al. 2014) and the U.S. Geological Survey (USGS) recommended method for calibration (Barnes 1964). All water samples and calibration buffers were stirred and both pH electrode measurements were made immediately upon collection after a one-minute stabilization period. Sample temperature was measured at the same time as pH measurements to a precision of ±0.1 °C. To test their accuracy and precision after calibration, results of replicate (n = 10) buffer pH (8.00 ± 0.02 at 25 °C) measurements were 7.99 ± 0.02 and 8.012 ± 0.009, for the YSI and Metrohm pH electrodes, respectively. During the study, the YSI and Metrohm pH electrodes had average response slopes of 98.1 ± 0.1% (n = 6) and 100.1 ± 0.7% (n = 18), respectively, of the theoretical response.

Electrochemical pH measurements were temperature corrected to the in situ tank temperature using the same approach as outlined above for spectrophotometric pH. YSI pH measurements were only evaluated at ~15 °C in the test tank because it was not available when tank measurements were being done at 10 and 20 °C.

Total alkalinity

Unfiltered samples were analyzed for A_T using an open cell titration system consisting of a syringe pump (Kloehn Co LTD), pH electrode (Metrohm AG, Ecotrode Plus), and pH meter (Fisher Scientific, AR 25). The electrode was conditioned for low ionic strength solutions by immersion in tap water for one hour prior to use. Titration data were processed using the non-modified Gran Plot titration method (Gran 1952) from pH 3.5 to 3.1. The HCl acid titrant ranged from 0.0997- 0.1002 N (Fisher Scientific) and the factory certified value was used in the analysis. A_T was analyzed on the bottle samples after spectrophotometric pH to minimize pH error from CO_2 exchange.

The automated titration system was tested monthly prior to sample analysis using an in-house alkalinity standard made from dried sodium carbonate (Na_2CO_3). The average difference between the standard and measured values was -1.0 ± 4.3 μmol L^{-1} ($n = 13$) (Appendix A, Figure S1). Consequently, very good “calibration-free” accuracy was achieved, and no offsets were added to the standard A_T values.

Dissolved organic carbon (DOC) was measured on tank samples to assess whether non-carbonate alkalinity (i.e., organic acid anions) could be significant. DOC was analyzed with an Aurora 1030W Total Organic Carbon Analyzer (Xylem Inc., OI Analytical) that uses heated persulfate wet chemical oxidation coupled with an NDIR detector (U.S. EPA, 2005).

Carbonate system equilibrium programs

Two commonly used equilibrium programs (CO2SYS and PHREEQC) (Lewis and Wallace, 1998; Parkhurst and Appelo, 2013) and an in-house MATLAB script (Appendix A) (hereafter referred to as CalcCO2_frompH) were used to assess the influence of μ on freshwater pCO_2 calculations. CO2SYS’s freshwater option sets $\mu = 0$ (infinite dilution) (Lewis and

Wallace, 1998) while PHREEQC (Parkhurst and Appelo, 2013) and CalcCO2_frompH can incorporate μ values. Carbonic acid thermodynamic equilibrium constants (K_1 and K_2) from Millero (1979) and Henry's law constant (K_H) from Weiss (1974) are used in CO2SYS and CalcCO2_frompH. CalcCO2_frompH accounts for changes in dissociation constants due to μ using the Davies equation (right side of Eq. 3) (i.e., apparent dissociation constants K_1', K_2', and K_H'; Appendix A). PHREEQC (version 3.4.0, Database used: wateq4f; Ball and Nordstrom, 1991), on the other hand, uses equilibrium constants from Plummer and Busenberg (1982). Over a temperature range of 0-30 °C, average percent differences between Millero (1979) and Plummer and Busenberg (1982) equilibrium constants (K_1 and K_2) were 0.15% ± 0.08% and 0.25% ± 0.09%, respectively. Further, the average percent difference between Weiss (1974) and Plummer and Busenberg (1982) Henry's law constant over the same temperature range was 0.18% ± 0.12%. These differences have a negligible effect on calculated $p\mathrm{CO}_2$ so the $p\mathrm{CO}_2$ from each equilibrium program can be directly compared. Input parameters for CO2SYS include in situ temperature, A_T, and in situ $\mathrm{pH}_{\mathrm{NBS}}$. PHREEQC uses the same input parameters as CO2SYS with the addition of μ that it estimates from A_T. To minimize the charge balance equation within PHREEQC, a counterion (sodium, Na^+, in this case) is used. Lastly, CalcCO2_frompH uses temperature, A_T, in situ $\mathrm{pH}_{\mathrm{free}}$, and the estimated μ explained above. $\mathrm{pH}_{\mathrm{free}}$ is used instead of $\mathrm{pH}_{\mathrm{NBS}}$ in CalcCO2_frompH to be consistent with the program's apparent dissociation constants.

Field application

Overview

In situ spectrophotometric pH measurements were made in the Clark Fork River (CFR), MT, USA to evaluate the accuracy of calculating $p\mathrm{CO}_2$ through a real-world application. Submersible Autonomous Moored Instruments (DeGrandpre et al. 1995; Martz et al. 2003;

Lynch et al. 2010) were deployed to measure spectrophotometric pH (SAMI-pH) and pCO_2 (SAMI-CO_2) directly in the CFR. A conductivity sensor for estimating μ was also deployed as described below. A conductivity-derived A_T was calculated from a linear relationship between specific conductivity and A_T obtained from data collected from 2017-2020 (discussed below). The calculated A_T was used with in situ pH_{free}, temperature, and μ to calculate pCO_2 using the CalcCO2_frompH program. This pCO_2 was then compared to the in situ pCO_2 measurements. A similar strategy is commonly used to compute seawater pCO_2, i.e., A_T is derived from a linear relationship with salinity and used with pH measurements to compute pCO_2 (Gray et al. 2012; DeGrandpre et al. 2019). In situ temperature was measured directly from the SAMI-CO_2 and SAMI-pH. Temperature between the two sensors showed good agreement (-0.5 ± 0.4 °C), so in situ temperature from the SAMI-pH was used for all sensor-related equilibrium calculations. Discrete bottle samples for A_T and spectrophotometric pH_{free} along with specific conductivity, pH_{NBS}, and temperature (YSI) were also collected four times during the deployment. This study took place from August 21, 2019 to September 9, 2019 during base flow river conditions on the CFR at Gold Creek (GC), MT, USA (46°35’24” N, 112°55’42” W).

Autonomous in situ pH and pCO_2 instruments

The in situ pH system is based upon spectrophotometric pH measurements of sample and colorimetric indicator (e.g., purified meta-cresol purple), where a pump and valve draw in samples and mix with indicator (Seidel et al. 2008). The weak-acid indicator can perturb the sample pH and so the SAMI-pH employs an automated indicator pH perturbation correction (Seidel et al. 2008; Yuan and DeGrandpre, 2008) like what was described above for discrete spectrophotometric pH measurements (Li et al. 2020). The in situ pCO_2 sensor also uses a colorimetric pH indicator (bromothymol blue) for spectrophotometric detection and operates by equilibration of ambient freshwater (or seawater) pCO_2 with the indicator contained in a gas-permeable membrane (DeGrandpre et al. 1995). Prior to the field deployment, both the pH and pCO_2 instruments were validated or calibrated in house, respectively. An NIST traceable pH 8.00 ± 0.02 at 25.0 ± 0.1 °C ($\mu = \sim 0.2$ M) phosphate buffer was used to check the SAMI-pH accuracy. The SAMI-pH values were converted to pH_{NBS} (Eq. 3) and showed good agreement with the phosphate buffer (average error of -0.007 ± 0.001 pH units, $n = 12$, at 25.05 ± 0.05 °C). The CO_2 sensor was calibrated over a range of 100-2000 µatm at 20.0 ± 0.1 °C for 10 days in the same test tank described above, using the LI-COR for pCO_2 validation (DeGrandpre et al. 1995). The SAMI-CO_2 has a response time of ~5 min and an estimated uncertainty of ~10 ± 1 µatm based on the standard deviation of residuals from the calibration fit ($n = 956$).

Conductivity and conductivity-derived alkalinity

The conductivity sensor (HOBO, Onset U24 Freshwater) was calibrated before deployment and assessed for sensor drift after deployment using the same method described above for the laboratory tests. Discrete measurements of conductivity were also taken using the YSI calibrated the same way as the in situ conductivity sensor. No sensor drift was evident but the entire in situ time series was corrected with a constant offset of -12.9 µS cm^{-1} based on the average difference between the in situ and discrete conductivity measurements.

The linear relationship using data collected from 2017-2020 at the deployment site ($n = 33$) between conductivity and A_T is shown in Figure 1. A_T correlates with conductivity because it is primarily bicarbonate (HCO_3^-) at this location and along the CFR (Appendix A, Figure S2) and is relatively conservative with a single source (i.e., groundwater) that is also diluted or concentrated proportionally from precipitation and evaporation, respectively. The residual error from this relationship ranged from -303 to 262 µmol L^{-1} with a standard deviation of ±130 µmol

L^{-1} (~5% uncertainty relative to the mean A_T). The contribution of A_T uncertainty to the calculated $p\text{CO}_2$ used for the field application is assessed below.

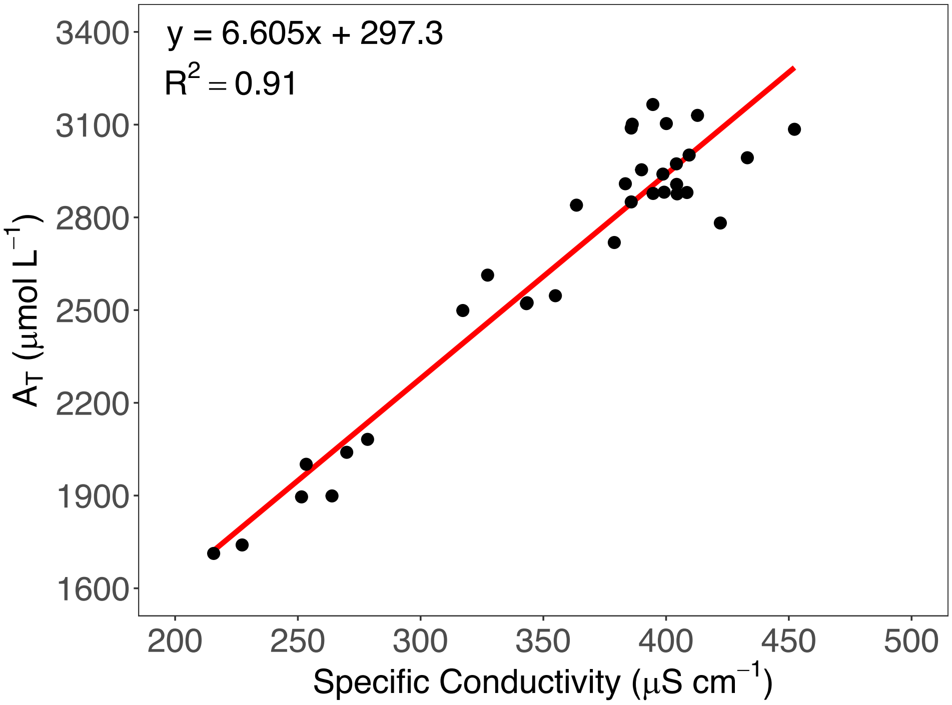

Figure 1. The relationship between A_T and specific conductivity obtained on the CFR at GC used to calculate A_T for $p\text{CO}_2$ computation. The red line is the linear best fit (n = 33). The average residual A_T is 0 ± 130 µmol L^{-1}.

Estimating riverine μ

In situ μ was estimated using a relationship between A_T and μ at Bearmouth, MT, USA on the CFR from Nagorski (2001):

$$\mu = (2.63 \times 10^{-6} * A_T) + 7.01 \times 10^{-4} \tag{5}$$

The Bearmouth sampling site is located on the CFR (46°42’16” N, 113°20’41” W) ~55 km downstream of the deployment site and has similar chemical composition (i.e., pH and A_T; Nagorski, 2001). To obtain Eq. 5, ionic strength was calculated from Eq. 4 from measured total ion concentrations (HCO_3^-, Ca^{2+}, K^+, Mg^{2+}, Na^+, SO_4^{2-}, SiO_3^{2-}) in surface water samples and linearly correlated with A_T (Nagorski, 2001). Equation 5 was then used to estimate μ during the deployment using the conductivity-derived A_T from Figure 1.

Data analysis

The primary statistical analyses used for this study were linear regression analysis and Student's T-Test ($\alpha = 0.05$). These tools allowed us to examine the significance of direct comparisons between pH measurements as well as calculated $p\mathrm{CO}_2$ values. Graphical visualization techniques, which include error and 1:1 plots, were also used to explore dataset-wide trends as they related to differences in pH measurements and $p\mathrm{CO}_2$ values.

Assessment

Laboratory study

Electrochemical and spectrophotometric pH comparisons

The tank experiment took place over a 7-month period where 35 tank samples were analyzed for pH and A_T. The overall measured $\mathrm{pH}_{\mathrm{NBS}}$ in the test tank ranged from 7.91 to 9.11 with an average pH of 8.40 ± 0.29. The standard deviation of the spectrophotometric pH replicates ranged from ±0.0001 to ±0.02 pH units ($n = 3$) over the range of $p\mathrm{CO}_2$ in the test tank (~100 to 1600 µatm). During the study, no replicate samples were taken for electrochemical pH measurements (i.e., Metrohm and YSI). However, an independent assessment of the precision of each electrode found the Metrohm ($n = 6$) and YSI ($n = 6$) pH precisions to be ±0.005 and ±0.05 pH units, respectively. Note that the digital resolution of the Metrohm and YSI pH meters are ±0.001 and 0.01, respectively.

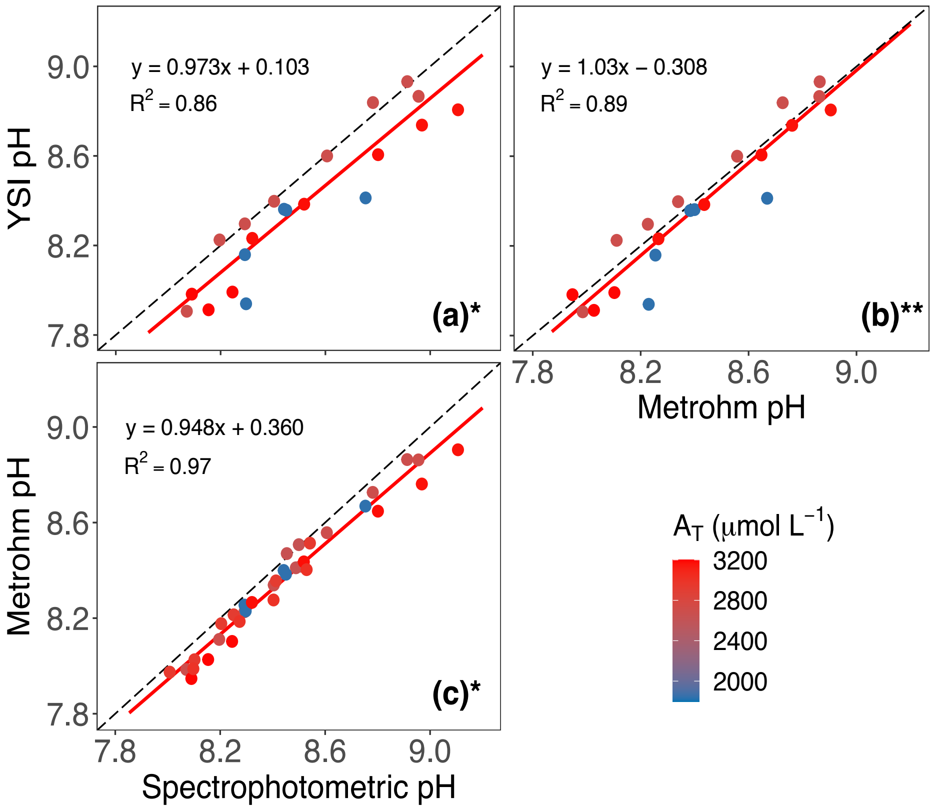

Figure 2. A comparison of in situ electrochemical and spectrophotometric pH_{NBS} measured in the test tank (15.2 ± 2.2 °C). The pH was varied by changing the pCO_2 and A_T (see *Methods*). **(a)** YSI pH electrode versus spectrophotometric pH data. **(b)** YSI pH electrode versus the Metrohm pH electrode data. **(c)** Metrohm pH electrode versus spectrophotometric pH data. Data points are colored by measured A_T in the test tank and range from 1841–3195 µmol L^{-1}. The 1:1 line (black dashed line) and linear regression (red line) are also shown with the equation and the R^2 in the upper left of each plot. An * or ** indicate that the x and y axis variables are statistically different ($p<0.05$) or not ($p>0.05$), respectively. Error bars for the spectrophotometric pH values have been omitted because the range of the error is too small to be seen on the x-axis range (0.00017 - 0.016 pH units).

Figure 2 shows that spectrophotometric pH_{NBS} and electrochemical pH_{NBS} data fall below the 1:1 line indicating that both electrode pH data are lower than the corresponding spectrophotometric pH measurements ($p<0.001$; Table 1). The pH electrode data are uniformly scattered around the 1:1 line (Figure 2b) and there is no statistical difference between the two electrochemical pH datasets ($p>0.05$; Table 1, Figure 2b). Additionally, the slopes derived from the linear regressions between spectrophotometric and electrochemical pH are statistically different from 1.0 (Figure 2a,c; $p<0.001$). The slopes <1.0 appear to arise from systematically larger pH differences at higher pH (i.e., pH >8.7; Figure 2a,c).

The coefficients of determination (R^2) for each pH comparison were found to be 0.86, 0.89, and 0.97 for Figure 2a,b,c, respectively (Table 1). These values further illustrate differences in random errors between the electrochemical and spectrophotometric pH measurements. The lower R^2 values appear to be due to larger random errors from the YSI pH electrode (Table 1, Figure 2a,b) reflecting the replicate precision discussed above. The standard deviation of the residuals for each regression analysis were ±0.12, ±0.11, and ±0.05 pH units (Figure 2a,b,c, respectively), with the larger residual standard deviations corresponding to the regressions involving the YSI pH electrode.

Table 1. The average (±SD) differences for each regression analysis and R^2 values for the three pH techniques of spectrophotometric (Spec), Metrohm, and YSI found in Figure 2. An * or ** indicate that the comparison is either statistically different or not, respectively, with an $\alpha = 0.05$.

Average Differences (±SD)	Spec – Metrohm* (*n* = 35)	0.084 ± 0.050	$R^2 = 0.97$
	Spec – YSI* (*n* = 21)	0.13 ± 0.12	$R^2 = 0.86$
	Metrohm – YSI** (*n* = 21)	0.036 ± 0.11	$R^2 = 0.89$

Calculated pCO_2

Table 2. The average (±SD) and range of calculated pCO_2 and pCO_2 error (compared to the measured pCO_2) between the three pH techniques calculated from CO2SYS at infinite dilution. The average percent error of each pH technique relative to the measured pCO_2 is also reported.

		Spectrophotometric (n = 34)	Metrohm (n = 34)	YSI (n = 20)
Calculated pCO_2 (µatm)	Average (±SD)	683 ± 417	825 ± 522	826 ± 643
	Range	130-1660	203-2065	172-2240
pCO_2 Error (µatm)	Average (±SD)	58 ± 33	203 ± 125	277 ± 284
	Range	-30-110	65-553	25-973
Percent Error (%)	Average (±SD)	14 ± 9	40 ± 21	62 ± 51

The pCO_2 errors calculated from the pH_{NBS} data in Figure 2 were assessed over a pCO_2 range of 101-1593 µatm. The pCO_2 was calculated using CO2SYS at infinite dilution, discussed above, to be able to focus solely on how pH measurements affect calculated pCO_2. Later, a thermodynamically rigorous comparison is made to illustrate deviations in calculated pCO_2 due to μ. The pCO_2 error dependence on pCO_2 levels is shown in Figure 3. The error in calculated pCO_2 using the Metrohm and YSI pH electrodes generally increased with increasing pCO_2 (Figure 3a,b), whereas the error in calculated pCO_2 from spectrophotometric pH appears relatively consistent with increasing pCO_2 (Figure 3c). Spectrophotometric, Metrohm, and YSI pH had average pCO_2 errors (calculated – measured) of 58 ± 33 µatm, 203 ± 125 µatm, and 277 ± 284 µatm, respectively (Table 2). Additionally, the average percent errors from spectrophotometric, Metrohm, and YSI pH are 14 ± 9%, 40 ± 21%, and 62 ± 51%, respectively (Table 2). Metrohm and YSI calculated pCO_2 also displayed the largest absolute errors of 553 and 973 µatm, respectively (Table 2). Further, temperature did not appear to affect pCO_2 error regardless of the pH used (Figure 3b,c). The systematically high pCO_2 values from the electrode measurements (Figure 3a,b, Table 2) supports that the pH bias shown in Figure 2 is due to errors in the electrode pH. The precision of calculated pCO_2 among the three pH techniques was also assessed. The pCO_2 precision from the two pH electrodes was ±125 and ±284 for Metrohm and YSI pH, respectively; compared to ±33 µatm for spectrophotometric pH (Table 2, SD of pCO_2 errors). From Figure 3 data, it is evident that pCO_2 calculated using spectrophotometric pH is both more accurate and precise compared to pCO_2 calculated from electrochemical pH (Figure 3c, Table 2), especially at higher pCO_2 levels.

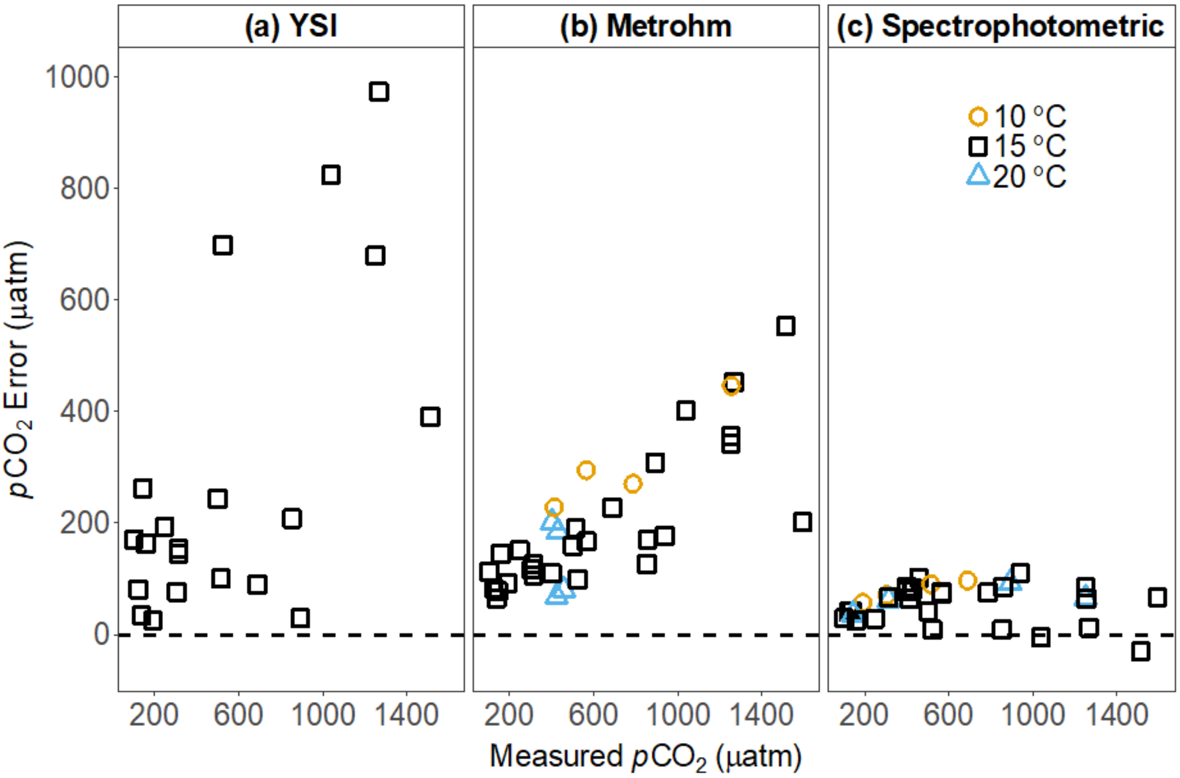

Figure 3. The pCO_2 error (calculated - measured) versus measured pCO_2. Spectrophotometric (n = 34), Metrohm (n = 34), and YSI (n = 20) pH_{NBS} data are used to calculate pCO_2 using the equilibrium program CO2SYS at infinite dilution. The dashed black line represents zero error. Measured A_T values ranged from 1841–3195 µmol L^{-1}. Different symbols represent different in situ tank temperatures. Calculated pCO_2 from the (b) Metrohm and (c) spectrophotometric pH measurements were analyzed at 10 °C (n = 4), 15 °C (n = 26) and 20 °C (n = 4) whereas calculated pCO_2 from the (a) YSI pH electrode was only analyzed at 15 °C (n = 20).

It is important to mention, here, that the tank DOC ranged from ~8-42 µmol L^{-1} (n = 6) during the study. Following the conclusions in Liu et al. (2020), that states that in more alkaline waters (e.g., pH = 7-8.5 and $A_T > 1000$ μmol L^{-1}) low in DOC (e.g., <350 μmol L^{-1}) the contribution of "excess A_T" from organic acid anions is negligible. Therefore, the tank water DOC was assumed to be too low to significantly contribute to the measured A_T, and consequently, the calculated pCO_2.

Assessment of μ and associated pCO_2 error

The importance of μ was initially underestimated in our pCO_2 accuracy evaluations as μ in freshwater systems is typically assumed to be zero (e.g., Hunt et al. 2011; Stets et al. 2017). We noticed that the calculated pCO_2 error would change depending on 1) the μ used to calculate in situ pH (Eq. 1,3) and 2) if μ was used to calculate apparent equilibrium constants (i.e., K_1', K_2', and K_H'). This led to the μ sensitivity tests using four different programs, CO2SYS at infinite dilution, PHREEQC, CalcCO2_frompH_1, and CalcCO2_frompH_2, which illustrate different approaches for using μ (Figure 4, Table 3). CalcCO2_frompH_1 and CalcCO2_frompH_2 pCO_2 values were calculated using spectrophotometric pH and A_T with calculated μ from the Missoula Aquifer (AWQR 2020) and from the Griffin and Jurinak (1973) relationship, respectively. The relationship from Griffin and Jurinak (1973) correlates μ with conductivity, but it is derived from soil water and river samples, making its comparison to CalcCO2_frompH_1 useful for broad scale applicability in other systems. Spectrophotometric pH_{free} measurements were used in CalcCO2_frompH_1 and CalcCO2_frompH_2. To be consistent with the pH scales, spectrophotometric pH_{NBS} values were used in both CO2SYS (infinite dilution) and PHREEQC. pCO_2 values calculated with CO2SYS were included to be able to compare to how pCO_2 is conventionally calculated in the literature and are the same values presented in Figure 3c. Additionally, PHREEQC calculates μ within its program from the input A_T (i.e., $[HCO_3^-]$) and counterion used to achieve charge balance (e.g., $[Na^+]$), neglecting other ions potentially present in waters. Thus, the μ used for the apparent dissociation constants are lower in PHREEQC compared to CalcCO2_frompH_1 and CalcCO2_frompH_2 (Table 3). Further, the average and standard deviation of μ presented in Table 3 reflect the differences in

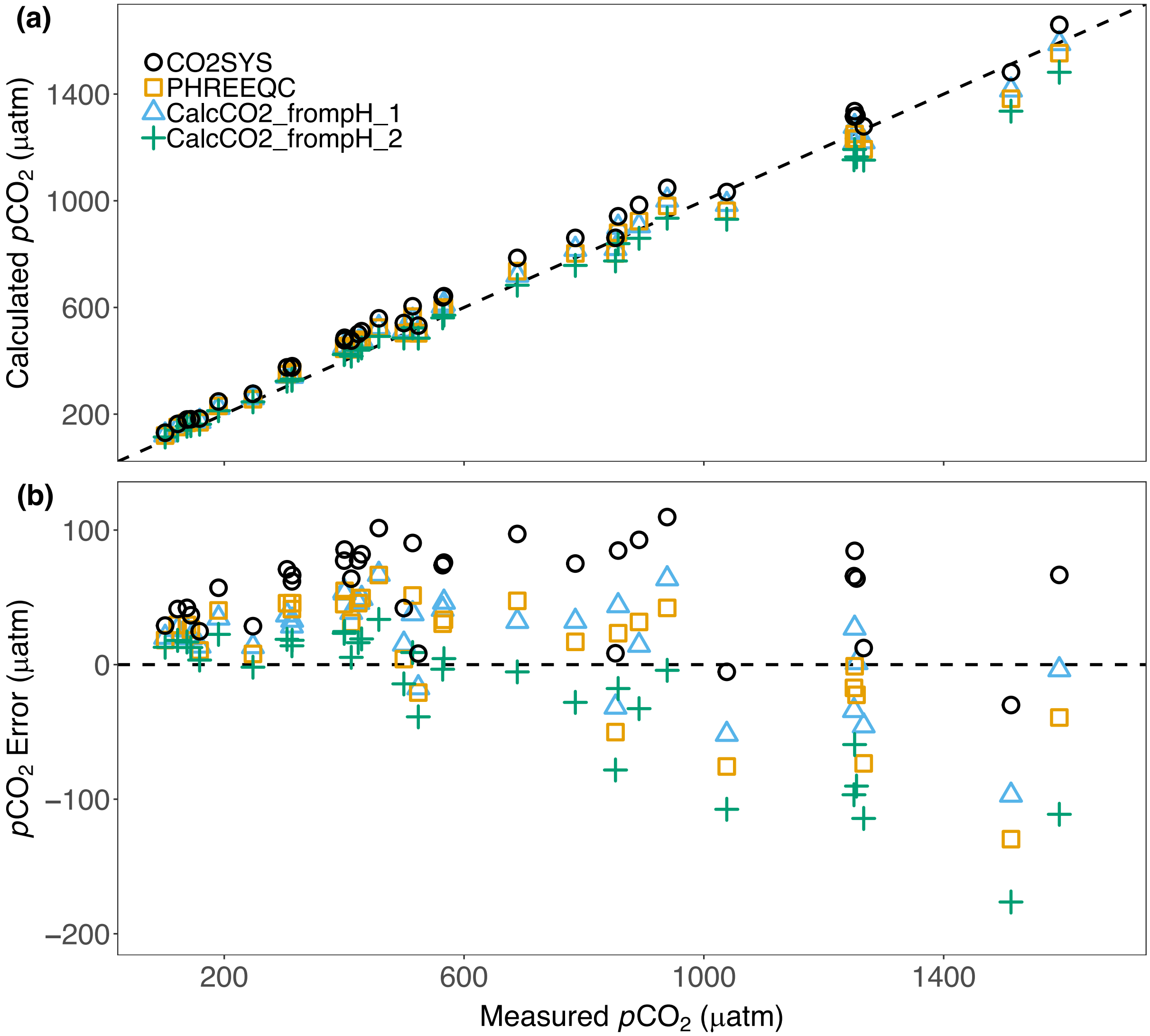

Figure 4. (a) The comparison of pCO$_2$ calculated from spectrophotometric pH and A$_T$ using different equilibrium models to measured pCO$_2$. The dashed black line represents the 1:1 line. pH$_{free}$ or pH$_{NBS}$ were used to be consistent with the pH scales in each program. **(b)** The pCO$_2$ error (calculated - measured) versus measured pCO$_2$ (n = 136). The black dashed line represents zero error.

the approaches used for estimating μ. Different approaches explicitly assume different ionic species concentration.

Table 3. The average (±SD) $p\mathrm{CO}_2$ error (|calculated - measured $p\mathrm{CO}_2$|) and range using different μ in CO2SYS (infinite dilution), PHREEQC, and CalcCO2_frompH. CalcCO2_frompH_1 and CalcCO2_frompH_2 use μ calculated from AWQR (2020) and Griffin and Jurinak (1973), respectively. μ averages (±SD) are included in the header and represent the μ used to calculate the apparent dissociation constants. Averages were taken from absolute values to avoid biases from large positive and negative values. The range is not reported in absolute values to illustrate the true range of $p\mathrm{CO}_2$ error.

	CO2SYS (n = 34) μ = 0 mM	PHREEQC (n = 34) μ = 2.8 ± 0.4 mM	CalcCO2_frompH_1 (n = 34) μ = 7.4 ± 1.2 mM	CalcCO2_frompH_2 (n = 34) μ = 4.2 ± 0.7 mM
Average (±SD)	58 ± 29	38 ± 24	35 ± 19	37 ± 42
Range	-30-110	-130-67	-97-67	-176-34

The different calculated $p\mathrm{CO}_2$ values are compared to the measured $p\mathrm{CO}_2$ using a 1:1 plot (Figure 4a) where most values appear to follow the 1:1 line with minimal spread. However, when looking at the $p\mathrm{CO}_2$ error, a "fanning-out" pattern becomes clear as you go from low to high $p\mathrm{CO}_2$ levels (Figure 4b). The $p\mathrm{CO}_2$ calculated from CO2SYS at infinite dilution generally overestimated $p\mathrm{CO}_2$ while the $p\mathrm{CO}_2$ calculated using apparent dissociation constants (CalcCO2_frompH and PHREEQC) generally underestimated $p\mathrm{CO}_2$ at higher levels (Figure 4b). Compared to the average error from PHREEQC, CalcCO2_frompH_1, and CalcCO2_frompH_2, the average error calculated from CO2SYS is significantly larger ($p<0.01$). The average error from PHREEQC, CalcCO2_frompH_1, and CalcCO2_frompH_2 is not significantly different from each other ($p>0.05$). Recall that CO2SYS and CalcCO2_frompH use the same equilibrium constants; thus, at infinite dilution these two programs calculate the same $p\mathrm{CO}_2$ values when using the same pH scale. The differences in calculated $p\mathrm{CO}_2$ between CO2SYS and CalcCO2_frompH arise in part because of the differences between $\mathrm{pH}_{\mathrm{NBS}}$ and $\mathrm{pH}_{\mathrm{free}}$ (Eq. 3). The error in calculated $p\mathrm{CO}_2$ gets further compounded by differences in infinite dilution dissociation constants (i.e., CO2SYS) and apparent dissociation constants (i.e., CalcCO2_frompH). Moreover, we see an increase in calculated $p\mathrm{CO}_2$ with increasing μ using $\mathrm{pH}_{\mathrm{free}}$ and CalcCO2_frompH as noted by the decreasing error from CalcCO2_frompH_2 to CalcCO2_frompH_1 (Figure 4b, Table 3). The increase in calculated $p\mathrm{CO}_2$ from higher μ is a result of the covariation between $\mathrm{pH}_{\mathrm{free}}$ and the apparent dissociation constants within CalcCO2_frompH. Conversely, we see a decrease in calculated $p\mathrm{CO}_2$ with higher μ using $\mathrm{pH}_{\mathrm{NBS}}$ (CO2SYS compared to PHREEQC; Figure 4b, Table 3).

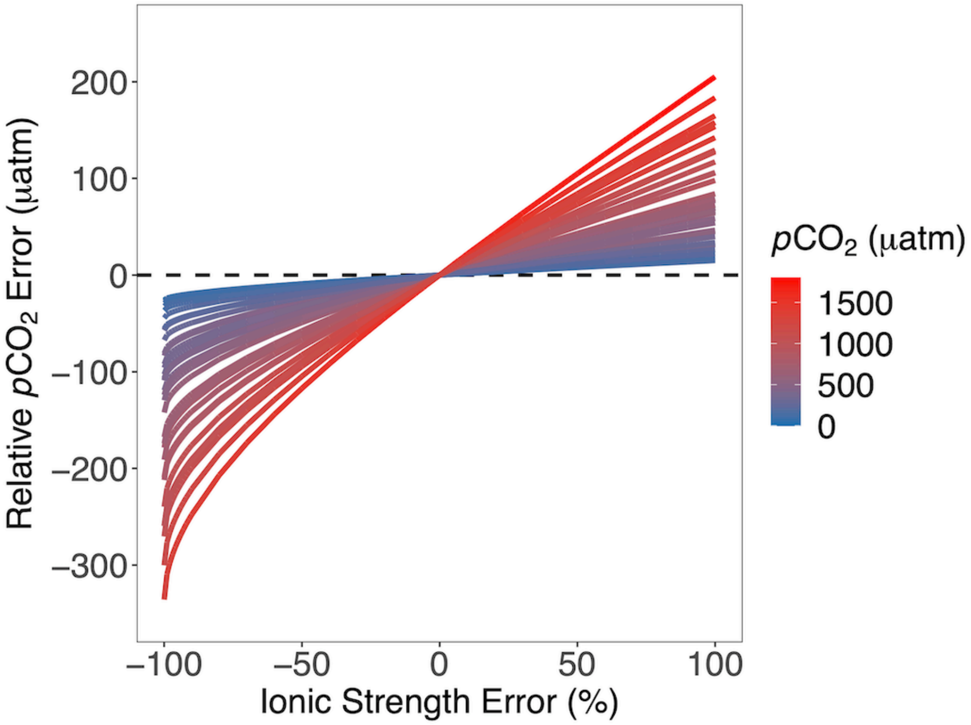

Figure 5. Modeled relative $p\mathrm{CO}_2$ error for percent error in μ where individual lines are colored by calculated $p\mathrm{CO}_2$ (µatm). Only the spectrophotometric $\mathrm{pH}_{\mathrm{free}}$ dataset was used for this model, thus, the $p\mathrm{CO}_2$ calculated from spectrophotometric $\mathrm{pH}_{\mathrm{free}}$ lies at 0% ionic strength error and zero $p\mathrm{CO}_2$ error. The black dashed line represents zero calculated $p\mathrm{CO}_2$ error. All model calculations of $p\mathrm{CO}_2$ were done using the CalcCO2_frompH script at in situ tank temperatures.

To further evaluate μ effects on calculated pCO_2 error, the pCO_2 error was modeled as a function of μ percent error. The pCO_2 calculated from spectrophotometric pH_{free} and its associated μ (calculated from AWQR 2020) were used as the reference dataset (dataset in Figure 4; CalcCO2_frompH_1). The reference spectrophotometric pH_{free} values were adjusted by using the Davies term (right side of Eq. 3) to account for the modeled μ percent error. Figure 5 illustrates the range for calculated pCO_2 error from zero ionic strength (e.g., -100% ionic strength error) to double the reference ionic strength (e.g., +100% ionic strength error; μ = 14.8 mM) over the range of pCO_2 found during the tank study. The relative error is also a function of pCO_2 where high pCO_2 error is associated with high pCO_2 levels and large μ error (Figure 5). Further, if μ is assumed to be zero (i.e., -100% ionic strength error) as is commonly done in freshwater CO_2 studies (Stets et al. 2017), the uncertainty in calculated pCO_2 error is ~20%. Moreover, at a -50% μ error relative to CalcCO2_frompH_1 (i.e., CalcCO2_frompH_2, Table 3), the average modeled pCO_2 error (from absolute values) was not statistically different from the CalcCO2_frompH_2 error (Table 3) ($p>0.05$).

Field application

The time-series from the field study are shown in Figure 6. Riverine pH_{free} and temperature measured from the SAMI-pH during the deployment ranged from 8.11 to 8.83 (average of 8.41 ± 0.21) and 1.7 to 21.3 ºC (average of 12.7 ± 4.6 ºC), respectively (Figure 6a,b). Conductivity-derived A_T (Figure 6c), specific conductivity (Appendix A, Figure S3), and μ (Appendix A, Figure S3) ranged from 2490 to 3440 µmol L^{-1} (average = 3050 ± 113 µmol L^{-1}), 394.4 to 465.4 µS cm^{-1} (average = 424.4 ± 8.7 µS cm^{-1}), and 7.3 to 9.7 mM (average = 8.7 ± 0.3 mM), respectively. The average diel range of pH was ~0.6 pH units and the average diel range of pCO_2 was ~900 µatm (Figure 6a,d). The average difference between discrete pH and SAMI-pH measurements was -0.003 ± 0.028 pH units for spectrophotometric pH and -0.09 ± 0.06 pH units for YSI pH. The average difference between discrete A_T and conductivity-derived A_T was -14 ± 11 μmol L^{-1}. Further, the pCO$_2$ calculated from spectrophotometric and YSI pH discrete samples

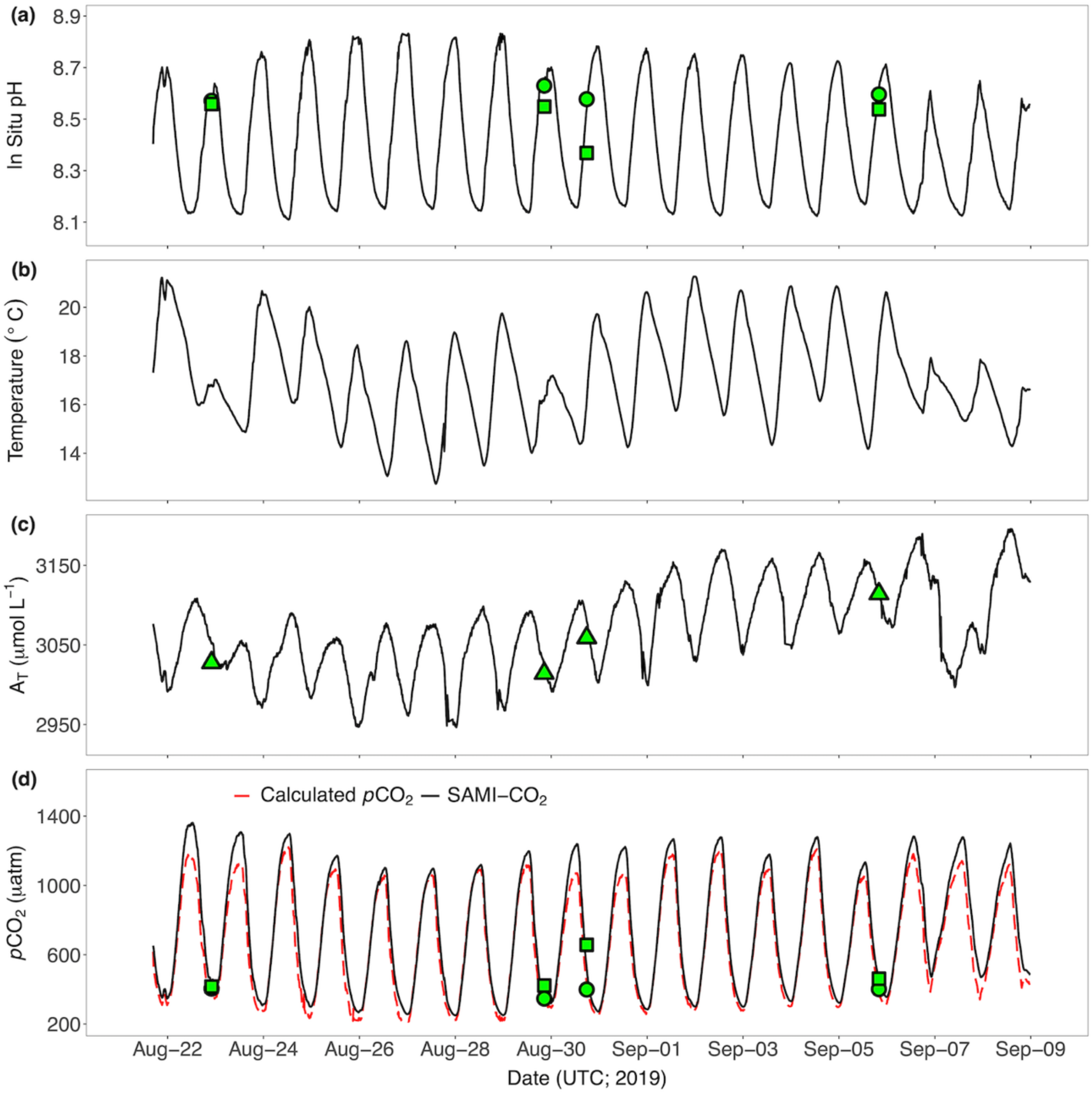

Figure 6. A 19-d in situ time series from the CFR of **(a)** spectrophotometric pH$_{free}$, **(b)** temperature, **(c)** conductivity-derived A_T, and **(d)** measured pCO$_2$ (SAMI-CO$_2$; solid black line) and calculated pCO$_2$ (SAMI-pH and conductivity-derived A_T; red dashed line). Discrete samples of measured pH and calculated pCO$_2$ using spectrophotometric pH (green circles) and YSI pH (green squares) are also shown in **(a)** and **(d)**, respectively. Discrete A_T samples are represented by green triangles in **(c)**. The date and time displayed is UTC during the year 2019.

had average differences of -66 ± 39 and 35 ± 71 μatm, respectively, when compared to SAMI-CO_2 measurements (Figure 6d).

The in situ pH_{free} (Figure 6a; Eq. 1) data was used with conductivity-derived A_T (Figure 1 and Figure 6c), μ (Appendix A, Figure S3; Eq. 5) and temperature (Figure 6b) to calculate pCO_2

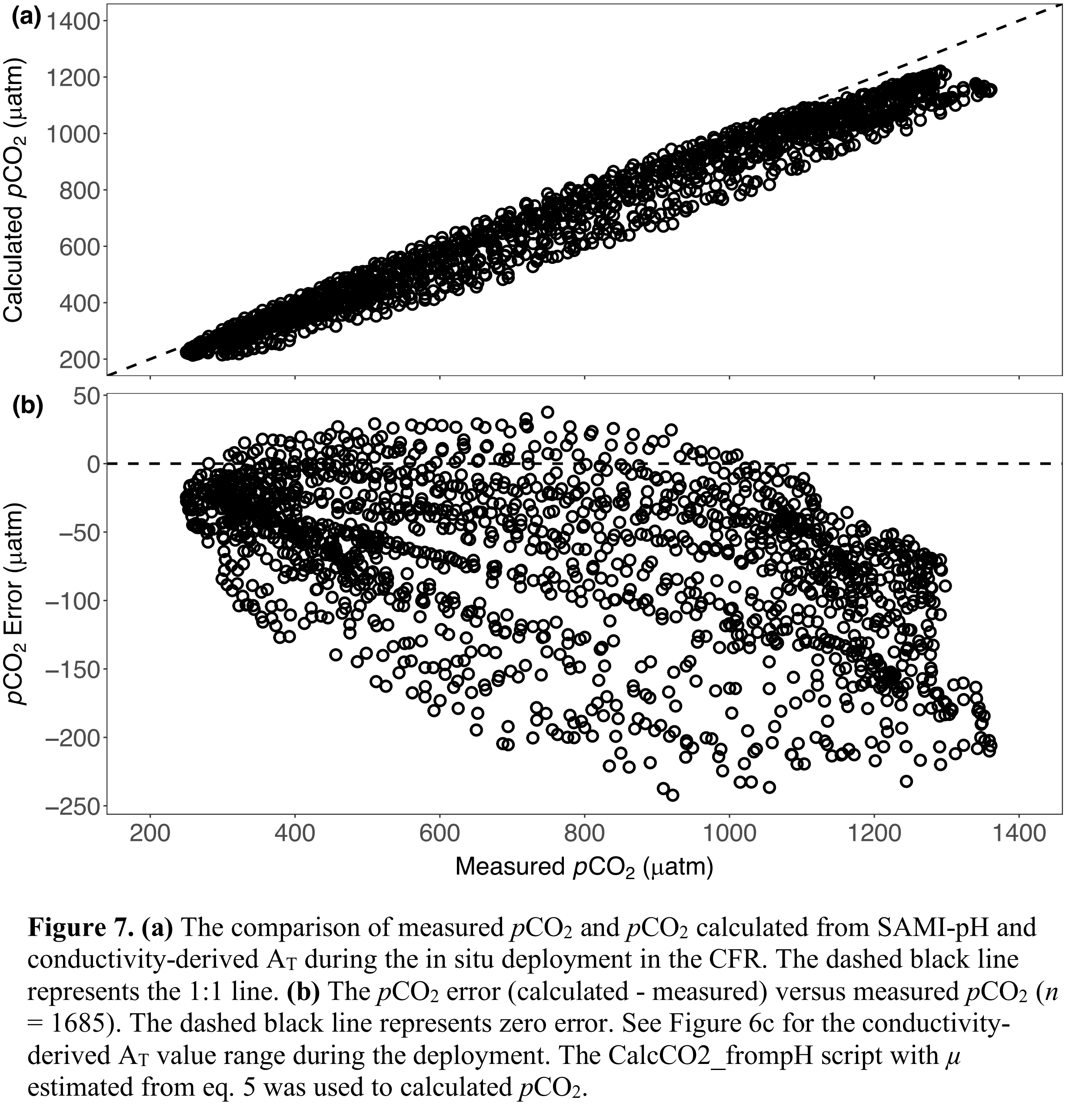

Figure 7. (a) The comparison of measured pCO_2 and pCO_2 calculated from SAMI-pH and conductivity-derived A_T during the in situ deployment in the CFR. The dashed black line represents the 1:1 line. **(b)** The pCO_2 error (calculated - measured) versus measured pCO_2 (n = 1685). The dashed black line represents zero error. See Figure 6c for the conductivity-derived A_T value range during the deployment. The CalcCO2_frompH script with μ estimated from eq. 5 was used to calculated pCO_2.

(Figure 6d). The average difference between the calculated and measured pCO$_2$ is -70 ± 57 µatm with an average percent error of 10 ± 7% (Figure 7). We found that the error in calculated pCO$_2$ during the field application was pCO$_2$ dependent e.g., the average error was -55 ± 52 µatm at pCO$_2$ <1000 µatm and -102 ± 55 µatm at pCO$_2$ >1000 µatm (Figure 7b). This error can be partially explained by uncertainty in the conductivity-derived A_T where the residual uncertainty from the Figure 1 linear fit is ±130 µmol L^{-1}. It is important to note that the uncertainty of the A_T (Appendix A, Figure S1) and specific conductivity (<5 µS cm^{-1}) measurements is much less than the uncertainty reported by the linear least-squares regression (Figure 1). This suggests that the scatter of this relationship is caused by biogeochemical factors and not measurement error. Instead, this relatively large uncertainty could be driven by evapotranspiration which creates diel inputs of groundwater (Dodds et al. 2017; Shangguan et al. 2021). Additionally, there appears to be a repeating clockwise pattern in pCO$_2$ error (i.e., hysteresis) (Figure 7b). Further discussion of potential mechanisms that may explain this pattern are provided below.

Discussion

It is evident in Figures 2 and 3, Tables 1 and 2, and the statistics stated in the *Assessment* that spectrophotometric pH has significantly better replicate precision than electrochemical pH and, based on its application for calculation of pCO$_2$, significantly better accuracy. Spectrophotometric pH is based on highly reproducible and accurate optical absorbances in contrast to the pH electrode potential that is affected by many environmental and instrumental factors (e.g., ionic strength gradient, buffer composition, reference potential, etc.). The conclusions presented here support findings of past studies that electrode pH is systematically low in low ionic strength solutions (Illingworth 1981; Herczeg and Hesslein, 1984; Davison and Woof, 1985) stemming from the liquid junction of the reference electrode.

The spectrophotometric pH accuracy and precision translates into greatly improved estimation of $p\mathrm{CO_2}$ from pH and A_T. The large differences in $p\mathrm{CO_2}$ calculated from the two pH electrodes show that, while electrode performance might be adequate under some circumstances, it is difficult to control and predict even in a controlled laboratory study with carefully calibrated electrodes. Figure S4 (Appendix A) provides further field-based evidence of this where electrochemical pH is more variable compared to spectrophotometric pH over time.

This study also found that accounting for μ in the equilibrium constants and $\mathrm{pH_{free}}$ can improve calculated $p\mathrm{CO_2}$ accuracy (Figure 4). The $p\mathrm{CO_2}$ error is reduced using the best available μ (Table 3, CalcCO2_frompH_1) compared to the common practice of using CO2SYS at infinite dilution (Table 3). Further, theoretical calculations indicate that changes in μ can alter equilibrium constants and impact calculated $p\mathrm{CO_2}$ (Figure 5). Moreover, theoretical calculations (Figure 5) were also able to predict a similar average error that was observed for CalcCO2_frompH_2.

The average percent error in calculated $p\mathrm{CO_2}$ from spectrophotometric $\mathrm{pH_{free}}$ (using CalcCO2_frompH) from the tank study and field application is 8 ± 6% and 10 ± 7%, respectively. The field application using in situ sensors demonstrated that spectrophotometric pH can be employed in a real-world application and produce similar results found in a controlled laboratory setting. As discussed above, the error in calculated $p\mathrm{CO_2}$ during the field application was $p\mathrm{CO_2}$ dependent (Figure 6 and Figure 7). Errors were largest at high $p\mathrm{CO_2}$ levels which occurred at night due to respiration (Figure 6d and Figure 7). Further, error in the conductivity-derived A_T relationship likely contributed significantly to the observed $p\mathrm{CO_2}$ error from the field application. As discussed above, the residual uncertainty in the relationship between specific conductivity and A_T (Figure 1) ranged from -303 to 262 $\mu\mathrm{mol\ L^{-1}}$ with a standard deviation of residuals of ±130 µmol L^{-1}. The large residuals are mostly driven by the data with high specific conductivity and high A_T (Figure 1), measurements that are common during base flow conditions. Because the field study took place during base flow conditions, uncertainties in the conductivity-derived A_T time series could contribute to the observed differences between calculated and measured pCO_2 (Figure 6d and Appendix A, Figure S5). To examine this idea, the standard deviation of residuals (±130 µmol L^{-1}) was added to and subtracted from the entire conductivity-derived A_T time-series (Figure 6c) to create upper and lower bounds (Appendix A, Figure S5). These limits were then used to calculate pCO_2, as described previously. Figure S5 (Appendix A) reveals that for most of the diel cycles, error in the conductivity-derived A_T can explain a significant part of the difference between calculated and measured pCO_2, where the original calculated pCO_2 error (Figure 6d) is significantly different from the uncertainty corrected pCO_2 error (Appendix A, Figure S5; upper orange ribbon boundary) ($p < 0.001$). The average pCO_2 error and percent error were reduced to -34 ± 54 µatm ($n = 1685$) and 7 ± 6%, respectively, a 51% improvement in calculated pCO_2 error. As discussed above, evapotranspiration (ET) can drive A_T and conductivity diel cycles (Wilcock and Chapra, 2005; Shangguan et al. 2021) and is likely controlling the diel A_T in the CFR (Shangguan et al. 2021), with lower groundwater signals during the day (lower A_T) due to riparian groundwater uptake. Thus, ET accounts for the major uncertainty of the A_T-conductivity relationship during base flow (Figure 1). This proposed mechanism seems to explain most of the difference between the calculated and measured pCO_2 during the field application portion of this study (Figure 6 and Appendix A, Figure S5). Additionally, the error in calculated pCO_2 may be further attributed to photo-contamination and/or temperature effects within the pH and pCO_2 sensors. Figure 7b indicates a cyclic pattern between pCO_2 error and measured pCO_2. Upon further exploration, we found that this hysteresis pattern is driven by a diel signal (i.e., solar radiation, temperature) in the river that causes the sensor's blank intensities to change. We believe, however, that this error is minor compared to the conductivity-derived A_T uncertainty.

Lastly, accurate pCO_2 is critical for constraining air-water fluxes. Therefore, the observed percent uncertainty in computed pCO_2 ($8 \pm 6\%$) from spectrophotometric pH_{free}, A_T, and μ (see dataset in Figure 4; CalcCO2_frompH_1) presented in this study would translate to a similar percent uncertainty when estimating CO_2 gas fluxes. Thus, more accurate CO_2 gas flux estimates could be obtained from spectrophotometric pH than from electrochemical pH, which had an observed percent uncertainty in computed pCO_2 of >40% (Table 2).

Conclusion

The study clearly demonstrates the advantages of using spectrophotometric pH for freshwater pCO_2 calculations. pH is of course a master variable in aquatic systems and a wide array of freshwater research could potentially benefit from higher quality pH measurements. Spectrophotometric pH data might improve model calculations of metal speciation/complexation and toxicity modeling (Wang et al. 2016; Huang et al. 2017), calcium carbonate saturation (Müller et al. 2015; Khan et al. 2021), and net ecosystem production (Oren et al. 2006; Lynch et al. 2010; Kanuri et al. 2017). Highly reproducible pH measurements will also be valuable for monitoring long-term changes in pH due to CO_2 acidification or other long-term anthropogenic impacts in rivers and lakes (Butman and Raymond, 2011; Phillips et al. 2015; Arroita et al. 2019; Minor et al. 2019). Moreover, a "do-it-yourself" portable photometer developed for seawater (Yang et al. 2014; Wang et al. 2019), could make discrete freshwater measurements of spectrophotometric pH for the computation of pCO_2 easier in the field. It remains, however, that measuring freshwater pCO_2 directly rather than computing it from inorganic carbon parameters is preferred, as is true for seawater. Although, our focus is on riverine CO_2, these findings and subsequent conclusions apply to all freshwater systems.

Future experiments should expand the pCO_2 range to include much higher levels (e.g., 2000-10000 µatm), vary the temperature over a larger range (0-30 ºC), and evaluate at lower A_T (e.g., <1000 µmol L^{-1}; Liu et al. 2020). Organic acid concentrations could further increase pCO_2 error and should also be considered in future studies with spectrophotometric pH and A_T. An additional complicating factor with spectrophotometric pH is that colored dissolved organic matter could cause inaccurate absorbance readings at high concentrations and could therefore lead to inaccurate pH values (i.e., tenths of pH units too low in strongly colored waters, Müller et al. 2017). This might mostly be corrected by the blank but needs to be tested, nonetheless. Thus, at high DOC concentrations both A_T and spectrophotometric pH measurements could be biased. The findings from this study also indicate that inaccurate μ contributes significantly to calculated pCO_2 uncertainty and must be accounted for to minimize pCO_2 error. Additionally, a caveat to our conclusions regarding field measurements of spectrophotometric pH is that the CFR is a well buffered system and so the indicator pH perturbation is relatively small (as discussed in *Methods*). This perturbation effect could be larger in other, less buffered systems (<1000 µmol L^{-1}) even if they are corrected using established methods (Yuan and DeGrandpre, 2008; Lai et al. 2016).

CHAPTER 3

The temporal and spatial regulation of inorganic carbon and air-water CO_2 flux along a montane river

Introduction

Dissolved inorganic carbon (DIC) has multiple sources and sinks within riverine aquatic ecosystems making it a valuable biogeochemical tracer. These sources and sinks include chemical weathering of silicate and carbonate-rich rocks (Middleburg, 2019), net ecosystem production (NEP) (Oren et al. 2006; Lynch et al. 2010; Kanuri et al. 2017), allochthonous inputs from tributaries and groundwater (Worrall and Lancaster, 2005; Shangguan et al. 2021), exchange of carbon dioxide (CO_2) with the atmosphere (Raymond et al. 1997; Finlay et al. 2010), and calcium carbonate formation and dissolution (Heath et al. 1995; Chauvaud et al. 2003; Liu et al. 2004; Shangguan et al. 2021). Due to the autochthonous production of DIC and its allochthonous transport pathways (i.e., sources of CO_2 from groundwater and soils), most streams and rivers are sources of CO_2 to the atmosphere (Neal et al. 1998; Aucour et al. 1999; Raymond et al. 2000; Hope et al. 2001; Wang and Cai 2004; Ciasis et al. 2008; Chen et al. 2012). Rivers are also important conduits for carbon to the coastal oceans, consequently, they represent a significant component of the global carbon cycle (Cole et al. 2007; Raymond et al. 2013; Hotchkiss et al. 2015). River air-water CO_2 fluxes are typically calculated as the CO_2 exchange over a given area of freshwater (Eq. 6):

$$\mathrm{CO_2\ Flux} = \left(p\mathrm{CO}_{2\,(\mathrm{water})} - p\mathrm{CO}_{2\,(\mathrm{air})}\right) \times \mathrm{K}_{\mathrm{H}}^{`} \times k_{\mathrm{CO}_2} \quad (6)$$

where $pCO_{2\,(water)}$ is the partial pressure of CO_2 (pCO_2) from the water column, $pCO_{2\,(air)}$ is the converted wet pCO_2 of the atmosphere, and K_H\` and k_{CO2} are the apparent solubility of CO_2 and gas transfer velocity (k_{600}) normalized to the temperature dependent Schmidt (Sc) number for

CO_2, respectively. However, challenges exist for quantifying CO_2 fluxes that include accurate quantification of gas transfer velocities and pCO_2 (Raymond et al. 2012; Duvert et al. 2018; Rocher-Ros et al. 2019; Ulseth et al. 2019; Young et al. 2022). Recent studies, however, have outlined techniques to increase the accuracy of both gas transfer velocities (Appling et al. 2018a, 2018b; Rocher-Ros et al. 2021) and calculated freshwater pCO_2 (Liu et al. 2021; Young et al. 2022). Thus, utilizing these recent advances can improve air-water CO_2 flux estimates for freshwater systems and more accurately characterize freshwater inorganic carbon dynamics.

Inland waters (i.e., rivers, lakes, etc.) are dynamic in nature with many spatial and temporal factors controlling their structure and function. Because of this, inorganic carbon dynamics in inland waters can differ greatly. The spatial variability of inorganic carbon in rivers and streams can be controlled by several biogeochemical processes including instream processing (e.g., gross primary production (GPP) and ecosystem respiration (ER)), allochthonous inputs (e.g., groundwater and tributaries), and floodplain connectivity. Accurate quantification of these processes can explain the variability from upstream to downstream within a given river as well as across different rivers and catchments (Hotchkiss et al. 2015; Rocher-Ros et al. 2019; Ulseth et al. 2019). In addition to spatial variability, temporal variability is also critical to assess as inorganic carbon can vary daily, seasonally, and interannually at a single location (Parker et al. 2007; Lynch et al. 2010; Arroita et al. 2019; Aho et al. 2021). Temporal variability can stem from hydrologic (i.e., annual snowmelt, localized precipitation, baseflow), physical (i.e., temperature, gas exchange), and biological production (i.e., GPP, ER). Note that several processes described here overlap and contribute to both spatial and temporal variability. Thus, accurately characterizing inorganic carbon both spatially and temporally is critical for adequately interpreting inorganic carbon variability along a river continuum (Hotchkiss et al. 2015).

As discussed above, being able to accurately quantify freshwater pCO$_2$ is a major factor in understanding its spatiotemporal variability in freshwater systems. While pCO$_2$ can be measured directly (Parker et al. 2007; Lynch et al. 2010; Rocher-Ros et al. 2020), it is often calculated from two inorganic carbon parameters such as pH and alkalinity (Hunt et al. 2011; Liu et al. 2020; Young et al. 2022) as explained in more detail in the *Methods* section. A recent study from Young et al. (2022), demonstrated by comparing spectrophotometric pH and electrode pH for CO$_2$ calculation, that systematic errors in pH electrode data overestimate pCO$_2$ by as much as 60%. Past freshwater studies have also shown that pCO$_2$ is typically overestimated when calculated from A_T and electrochemical pH (Abril et al. 2014; Hunt et al. 2011; Liu et al. 2020). However, by employing the method outlined by Young et al. (2022) and including ionic strength in carbonate equilibria and pH measurements, error in calculating freshwater pCO$_2$ can be minimized.

Accurate gas transfer velocities (Eq. 6) are also important for obtaining accurate air-water CO$_2$ flux estimates. Gas transfer velocities can be obtained through the R modeling program *streamMetabolizer* (sM) (Appling et al. 2018a, 2018b; Rocher-Ros et al. 2021). This program uses high-resolution (e.g., hourly) dissolved oxygen (O$_2$) data and Bayesian statistical modeling to estimate GPP, ER, and gas transfer velocities. Another way to estimate gas transfer velocities is by measuring the decline of added tracer gases such as sulfur hexafluoride (SF$_6$) or argon (Ar) (Hall and Madinger, 2018). However, this method can be difficult due to uncertainties in scaling (e.g., SF$_6$ to O$_2$) caused by solubility effects in conditions of bubble-mediated gas transfer (Hall and Madinger, 2018). Therefore, by using sM to obtain gas transfer velocities and the method presented by Young et al. (2022) to calculate pCO$_2$, high quality (i.e., accurate and precise) air-water CO_2 fluxes can be calculated, and spatial and temporal inorganic carbon gradients can be better resolved.

In the context of global air-water CO_2 estimates, Raymond et al. (2013) presented ~7000 calculated $p$$CO_2$ values from electrode pH, alkalinity, and temperature from around the world and highlighted the potential bias of erroneously low pH values in their analysis. They concluded that the median global $p$$CO_2$ was ~3100 µatm and ranged from ~1300-4300 µatm (Raymond et al. 2013). These median values turn out to be much higher than the median value reported in the UCFR (500 µatm; see below) from $p$$CO_2$ calculated from spectrophotometric pH, alkalinity, and temperature. Following the approach outlined in Liu et al. (2020) to estimate a CO_2% error due to error in pH for the presented median $p$$CO_2$ from Raymond et al. (2013) and a rough estimated freshwater specific conductivity of 500 µS cm^{-1} (Griffith, 2014) we calculate a CO_2% error of ~30%. This error shifts the global median down to ~2200 µatm and the range to ~900 to 3000 µatm and places the median $p$$CO_2$ in the UCFR closer to the range of global values but still considerably lower. This exercise highlights the recent advancements in being able to correct past estimates of $p$$CO_2$ (e.g., Liu et al. 2020), but more importantly stresses the need for obtaining accurate calculated freshwater $p$$CO_2$ values. The latter being an ongoing issue that could be mediated by the accuracy provided by spectrophotometric pH measurements for application in freshwater inorganic carbon research.

The study presented here is the first long-term freshwater inorganic carbon (i.e., DIC, $p$$CO_2$, and CO_2 flux) time series calculated using spectrophotometric pH. Spectrophotometric pH and total alkalinity samples were collected along ~200 km of the upper Clark Fork River (UCFR), MT, USA monthly for 48 months. These measurements along with in situ temperature and ionic strength were used to calculate $p$$CO_2$ (Young et al. 2022). The CO_2 flux in the UCFR has been estimated previously by Lynch et al. (2010) at one location over several years. Here we extend the assessment to include contiguous measures at multiple sites over 200 km of river for four water years to characterize tendencies and variability in the CO2 flux between the river and atmosphere.

Material and methods

Overview

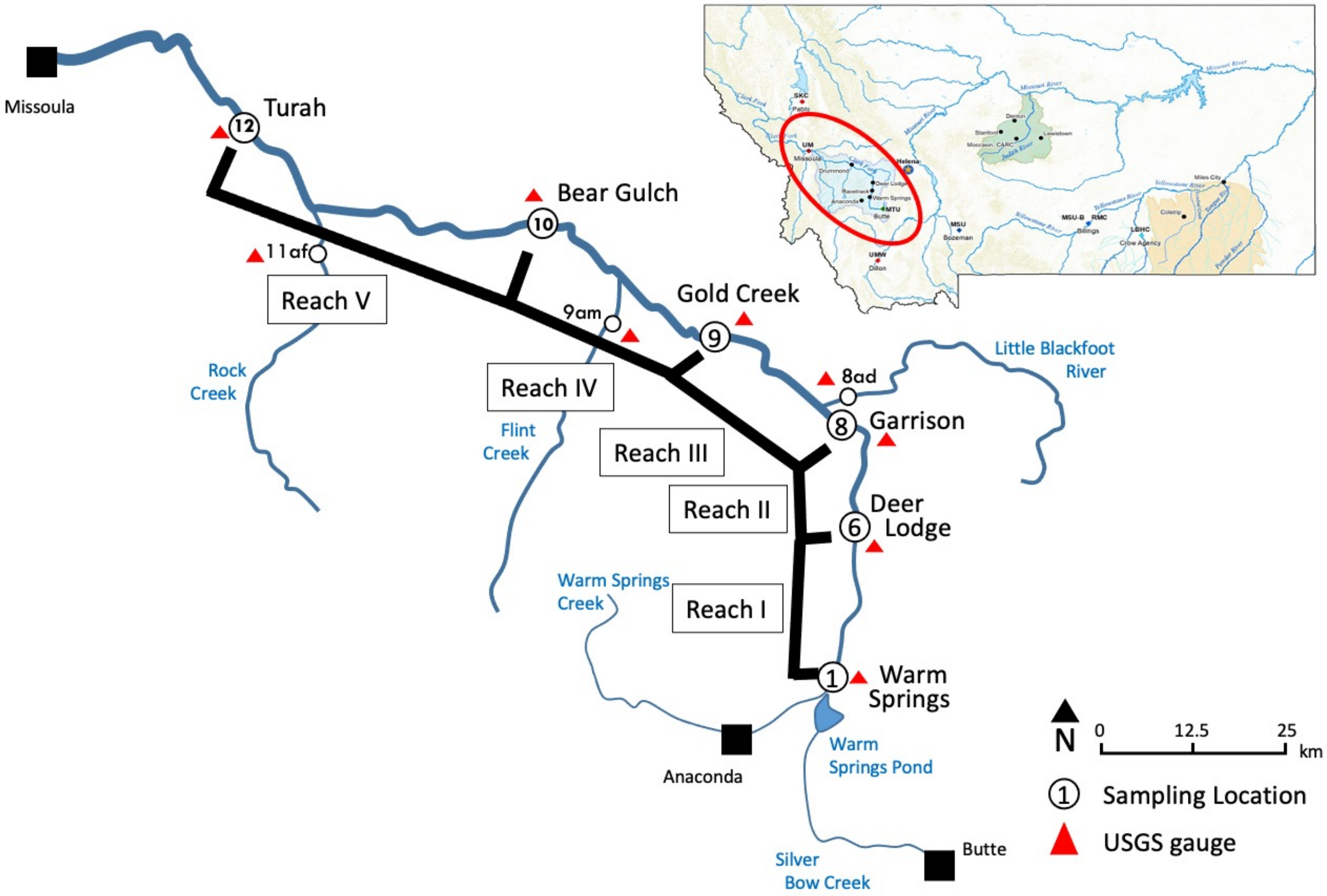

Figure 8. A map of the UCFR. Sampling sites are indicated by circles with numbers. The USGS gaging stations are depicted by red triangles and define the boundaries for Reaches I-V.

The UCFR drains a 57,000 km^2 catchment located in western Montana (USA) and is a productive mid-order river with average discharge of 23 ± 33 m^3 s^{-1}. It is also one of the largest superfund sites in the United States, with legacy of mining pollution (Moore and Luoma, 1990; Moore and Langner 2012). The UCFR was sampled at 6 main stem and 3 tributary sampling locations spanning ~200 km of the UCFR over four water years (Figure 8). Sampling was done monthly during the fall, winter, and spring months and bimonthly during the summer months. Samples were analyzed for total alkalinity (A_T) and spectrophotometric pH. Water temperature and specific conductivity were also measured in the field at the same time samples were collected. Discharge was obtained from six USGS gaging stations (Figure 8, Table 4) and the three tributary sampling sites include the Little Blackfoot (LBF), Flint Creek (FC), and Rock Creek (RC) (Table 4).

Table 4. Sample site names with corresponding sample site number, distance downstream from Warm Springs (Figure 8), elevation, and the location. Reaches are designated by roman numerals to the left of the sampling location names. A sampling site with two reach designations indicates that it is the end member for the previous reach and start member for the following reach.

Reach	Site Name	Site Number	Downstream Distance (km)	Elevation (m)	Latitude	Longitude
I	Warm Springs*	001	0.0	1459	46.1874	-112.7707
I, II	Deer Lodge*	006	44.9	1378	46.3831	-112.7380
II, III	Garrison*	008	64.8	1340	46.4984	-112.7388
III	Little Blackfoot*, ^{t}	008ad	73.6	1333	46.5187	-112.7923
III, IV	Gold Creek*	009	89.2	1276	46.5900	-112.9282
IV	Flint Creek*, ^{t}	009am	124.4	1227	46.6289	-113.1514
IV, V	Bear Gulch*	010	144.3	1155	46.7037	-113.3455
V	Rock Creek*, ^{t}	011af	182.1	1096	46.6977	-113.6692
V	Turah*	012	197.0	1013	46.8264	-113.8142

*Indicates sampling sites with USGS gage stations

^{t} Indicates tributary

Five river segments (Reaches I-V, Figure 8) were identified and averaged 39 ± 16 km in length. The shortest reach (Reach II) was 19.9 km in length. Reaches were generally longer downstream as river discharge increased where the longest reach (Reach IV) was 55.1 km long. Reaches I and II have no major tributaries while Reaches III, IV, and V include confluences with LBF, FC, RC, respectively (Figure 8, Table 4). This study focuses on a dataset comprised of 291 measurements of spectrophotometric pH and A_T used to calculate DIC, pCO$_2$, and air-water flux of CO$_2$ covering 48 months (51 sampling events) beginning in August 2017 and ending in September 2021.

Analytical methods

Spectrophotometric pH

Spectrophotometric pH measurements were made as outlined in Young et al. (2022), Lai et al. (2016), and Yao and Byrne (2001). Briefly, a double beam spectrophotometer (Agilent, Cary 300) was used with 10 cm cuvettes and temperature regulated cuvette holders. Because spectrophotometric pH and total alkalinity are analyzed from the same sample, spectrophotometric pH is analyzed first to minimize headspace that could allow gas exchange and alter the pH and pCO$_2$. Two to three pseudoreplicates (i.e., replicate measurements made from the same bottle sample) were analyzed and averaged for further use. Purified meta-cresol purple (pmCP) was used because the negative logarithm of its acid dissociation constant (pK_a) is equal to 8.6607 at 25 ºC at infinite dilution (μ = 0 mM) which overlaps with the pH range observed in the UCFR (Parker et al. 2007) and is optimal for many other alkaline freshwater systems (Peter et al. 2014).

Spectrophotometric pH measurements were calculated on the free hydrogen ion scale ($pH_{free} = -\log[H^+]$, where $[H^+]$ is the hydrogen ion concentration) using the equations from Young et al. (2022). Due to small changes in pH of the sample caused by the addition of indicator (Seidel et al. 2008; Yuan and DeGrandpre 2008; Li et al. 2020), pH was calculated using a linear regression of the pH values recorded with addition of three 80 µL indicator aliquots. The magnitude of this perturbation correction was found to be similar to that described in Young et al. (2022) and Yuan and DeGrandpre (2008) with an average correction of 0.005 ±

0.006 pH units (n = 1244). All sample measurements were temperature corrected to in situ temperature using the equilibrium model CO2SYS (Lewis and Wallace, 1998) at infinite dilution. This program uses an input (lab measurement) and output (in situ) temperature, alkalinity, and input pH. Temperature corrections averaged 0.14 ± 0.07 pH units due to large differences between ex situ (~20°C) and in situ (0 to 20°C) riverine temperature, especially during winter months. The resulting temperature corrected pH was used for subsequent pCO_2 calculations. Additionally, NIST traceable pH 8.00 ± 0.02 at 25.1 ± 0.3 °C (μ = ~0.2 M) phosphate buffers (Micro Essential Laboratory, Inc., Hydrion) were periodically measured monthly. The spectrophotometric pH measurements were converted to the National Bureau of Standards (NBS) scale (pH_{NBS}) (i.e., to allow direct comparisons) as described in Young et al. (2022), and temperature corrected to 25.0°C. Measurements showed good agreement with the pH buffer (average error of 0.00 ± 0.03 pH units, n = 45).

Total alkalinity

Unfiltered samples were analyzed for A_T using an open cell titration system consisting of a syringe pump (Kloehn Co LTD), pH electrode (Metrohm AG, Ecotrode Plus), and pH meter (Fisher Scientific, AR 25) (Young et al. 2022). The electrode was conditioned for low ionic strength solutions by immersion in tap water for one hour prior to use. Titration data were processed using the Gran Plot titration method (Gran 1952). The HCl acid titrant ranged from 0.0997- 0.1002 N (Fisher Scientific) and the factory certified value was used in the analysis.

The automated titration system was tested monthly prior to sample analysis using an alkalinity standard made from dried sodium carbonate (Na_2CO_3) following Young et al. (2022). The average difference between the standard and measured values was -0.3 ± 1.4 μmol L^{-1} (n = 34) and thus, very good calibration-free accuracy was achieved.

Estimating riverine ionic strength

In situ ionic strength (μ) was estimated for each sampling event using a relationship between A_T and μ at Bear Gulch (Figure 8, Table 4) established using data collected by Nagorski (2001):

$$\mu = (2.63 \times 10^{-6} * A_T) + 7.01 \times 10^{-4} \tag{7}$$

Estimates of μ were calculated from measured total ion concentrations (HCO_3^-, Ca^{2+}, K^+, Mg^{2+}, Na^+, SO_4^{2-}, SiO_3^{2-}) in surface water samples collected by Nagorski (2001) and linearly correlated with measured A_T (Eq. 7). Equation 7 was then used to estimate μ at each sampling location based on measured A_T. This calculated μ was then used for in situ pH for calculating DIC and $p\text{CO}_2$ (Young et al. 2022).

DIC and pCO₂

DIC and $p\text{CO}_2$ were calculated from spectrophotometric pH and A_T measurements using the equilibrium calculation described in Young et al. (2022). This calculation was used because it incorporates a range of μ values commonly found in freshwater environments and it has been shown that ignoring μ affects can affect the accuracy of calculated $p\text{CO}_2$ values and other inorganic carbon parameters (Liu et al. 2021; Young et al. 2022). Carbonic acid equilibrium constants (K_1 and K_2) from Millero et al. (1979) and Henry's law constant (K_H) from Weiss (1974) are used in this calculation and are modified to account for changes in dissociation constants due to μ using the Davies activity coefficient equation (i.e., apparent dissociation constants K_1', K_2', and K_H'). Based on the results in Young et al. (2022) we estimate the uncertainty of calculated $p\text{CO}_2$ and DIC to be about ±40 µatm and ±14 µmol L^{-1}.

Air-water CO₂ flux

The air-water CO_2 flux along the UCFR was determined from the calculated pCO_2 along with atmospheric pCO_2, K_H`, and k_{CO2} (Eq. 6). Air-water CO_2 flux was calculated at six sites along the UCFR and correspond to the sampling sites with USGS gage stations (Figure 8, Table 4). Atmospheric CO_2 was obtained from a meteorological tall tower in Wisconsin, USA (Andrews et al. 2017) of similar latitude to the UCFR (Appendix B, Figure S1). The tall tower has time series atmospheric CO_2 (among other measurements) from 1992 to present. It is important to note that these measurements are reported as the dry mole fraction of CO_2 in parts per million (xCO_2; ppm) and so these values were converted to wet pCO_2 (pCO_2; μatm) using barometric pressure, water vapor pressure, and temperature to convert xCO_2 to pCO_2 (Dickson et al. 2007). The resulting atmospheric pCO_2 was then used in the CO_2 flux calculations (Eq. 6).

The solubility of CO_2 in equation 6 (K_H`) was estimated using an empirical equation established by Weiss (1974). k_{CO2} (Eq. 6) was estimated using temperature dependent Schmidt numbers (Sc) calculated from an empirical relationship from Wanninkhof (2014) and estimated k_{600} values derived from sM (Appling et al. 2018b) using high resolution dissolved oxygen time series. The dissolved oxygen data used to generate k_{600} values were collected at the six sampling sites (Figure 8, Table 4) during baseflow conditions. *streamMetabolizer* was employed to segregate the dissolved oxygen timeseries based on discharge to pool k_{600} (Appling et al. 2018a,b). Estimating k_{600} based on similar discharge values (i.e., binning) was done because discharge varied considerably along the UCFR during baseflow oxygen sensor deployments with an average discharge across the six sites of 11 ± 7 m^3 s^{-1}. Depth was estimated for each sampling event using an empirical relationship between depth and discharge established by Raymond et al. (2012) (Appendix B, Figure S2). Monthly k_{600} values outside of baseflow conditions were estimated using relationships between discharge, depth, and baseflow k_{600} estimates (Appendix B, Figures S2, S3).

Temporal designation for seasonal analysis

For this study, seasons are defined by the months that best represent the seasonal progression in western Montana, USA. Western Montana is semi-arid with short autumnal duration, long winters, and a growing season that extends into late September. Therefore, seasons were defined accordingly: fall (October and November), winter (December through March), spring (April through June), and summer (July through September).

Data analysis

The molar deviation of DIC from atmospheric saturation (ΔDIC) was calculated for each location from temperature, atmospheric $p\mathrm{CO_2}$, and measured $\mathrm{A_T}$ using CO2SYS (Lewis and Wallace, 1998). The difference between the measured aqueous concentration of DIC and its calculated concentration in equilibrium with the atmosphere is expressed in equation 8 following Stets et al. (2017):

$$\Delta\mathrm{DIC} = \mathrm{DIC_W} - \mathrm{DIC_A} \tag{8}$$

where $\mathrm{DIC_W}$ is the calculated DIC in the water column from $\mathrm{A_T}$ and spectrophotometric pH and $\mathrm{DIC_A}$ is the estimated DIC concentration at atmospheric equilibrium at a given temperature, $\mathrm{A_T}$, and atmospheric $p\mathrm{CO_2}$ (Stets et al. 2017). ΔDIC was then used to assess DIC saturation (i.e., -ΔDIC = undersaturated, +ΔDIC = oversaturated) along the UCFR and how that relates to air-water $\mathrm{CO_2}$ flux variability. At the reach scale, differences in ΔDIC from downstream to upstream (ΔΔDIC) were also estimated to assess changes in DIC saturation along the UCFR (Eq. 9).

$$\Delta\Delta\mathrm{DIC} = \Delta\mathrm{DIC_{dwn}} - \Delta\mathrm{DIC_{up}} \tag{9}$$

ΔDIC_{dwn} and ΔDIC_{up} represent the calculated ΔDIC values (Eq. 8) at the downstream and upstream location, respectively. The primary statistical analyses used for this study were linear regression analysis with Pearson correlations (r) and coefficients of determination (R^2) and Student's t-test ($\alpha = 0.05$). These analyses allowed us to examine insights into the connections among many variables of interest.

Sampling bias

Due to the dynamic nature of pCO_2 in freshwater it is important to discuss the potential for sampling bias whenever discrete samples are concerned. Samples from each sampling event were collected from all sampling sites along the UCFR (Figure 8) in one day (Dent and Grimm, 1999; Ensign et al. 2017). Each sampling event took ~6-hr to complete. Sample collection began

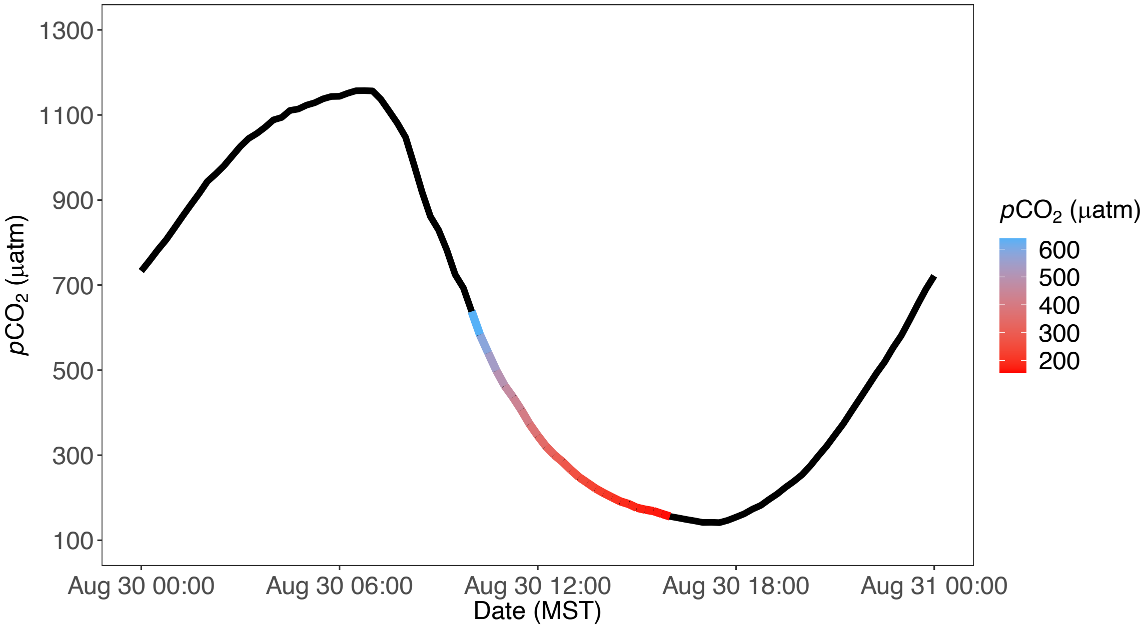

Figure 9. A 24-hr pCO_2 timeseries at the Gold Creek (Figure 8) sampling location in the UCFR collected using an in situ pCO_2 sensor (Young et al. 2022). The solid black line denotes the measured diel pCO_2 in the river and the colored segment denotes how pCO_2 levels change over the course of each sampling event from 10:00 am (blue) to 4:00 pm (MST) (red).

at ~10:00 am Mountain Standard Time (MST) at Warm Springs and ended at ~4:00 pm MST at Turah (Figure 8). Past studies have shown that pCO_2 exhibits large diel variability along the UCFR (Parker et al. 2007; Parker et al. 2010; Lynch et al. 2010; Young et al. 2022). A bias up to ~400 µatm exists in the UCFR depending on when sampling takes place with values biased high upstream and low downstream (Figure 9). For example, the mean diel pCO_2 of an upstream site near Warm Springs is ~400 µatm (DeGrandpre et al. unpubl.). When sampling at around 11:00 am MST, Figure 9 shows that the pCO_2 level could be ~500 µatm indicating a +100 µatm sampling bias. In contrast, the mean diel pCO_2 of a downstream site near Turah is also ~400 µatm (Lynch et al. 2010). However, when this site is sampled around 4:00 pm MST, Figure 9 shows that the pCO_2 level could be ~200 µatm indicating a -200 µatm sampling bias. The examples provided here are extreme cases where sampling bias is greatest. It is important to note, however, that most sampling during the day (11:00 am to 2:00 pm MST) takes place near the mean diel pCO_2 which, depending on location, can be relatively close to atmospheric levels. Moreover, sampling near the mean diel pCO_2 value can be beneficial for long-term monitoring as the mean diel pCO_2 will regulate air-water CO_2 flux more than the diel range (i.e., minimum, and maximum) due to slower CO_2 exchange.

Results

Spatiotemporal variability of inorganic carbon

Temperature, discharge, and inorganic carbon parameters followed consistent annual and seasonal trends along the UCFR (Figure 10). In situ temperature averaged 9.0 ± 6.4 °C ($n = 347$) and ranged from 0.0 to 21.0°C with minimum and maximum temperatures reported during the winter and summer, respectively. Generally, riverine temperature was coldest upstream near Warm Springs (Figure 10d). Discharge among the sites followed annual oscillations of peak flow

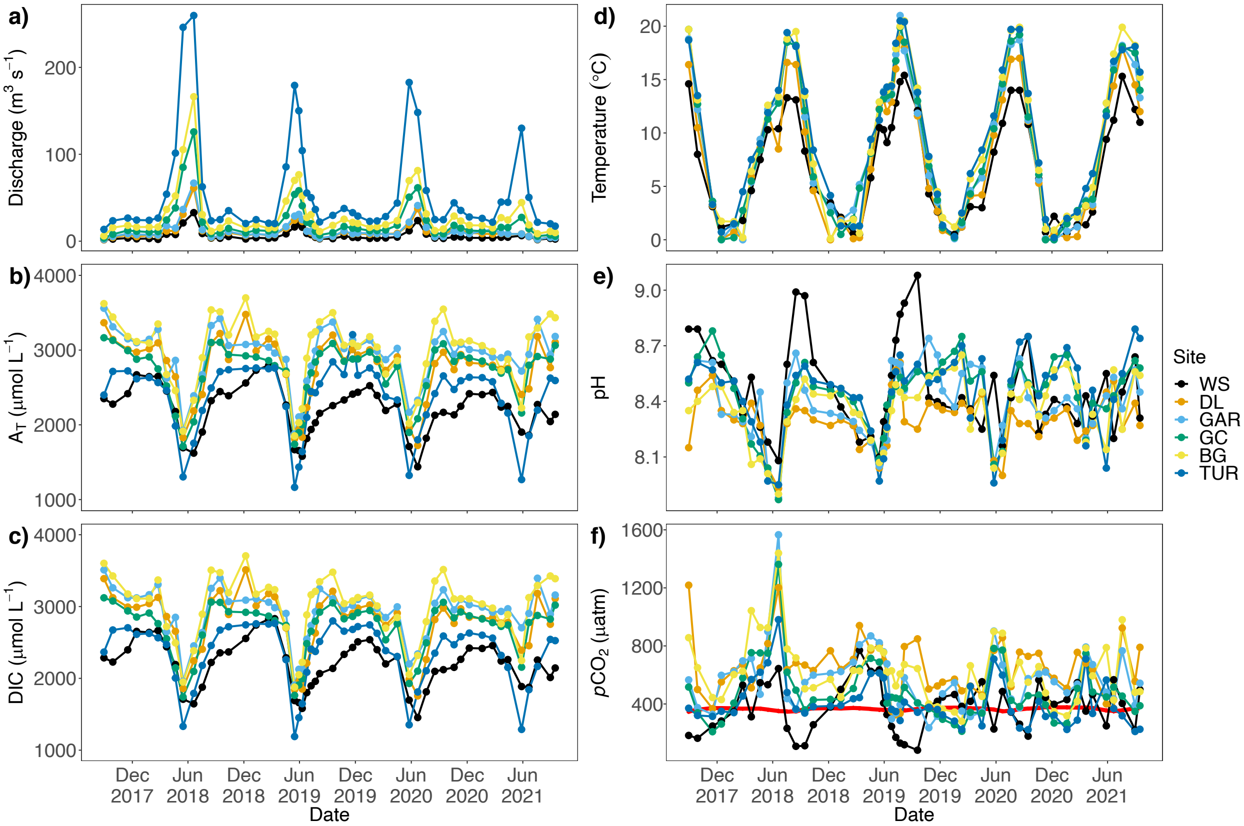

Figure 10. The spatiotemporal timeseries for **a)** discharge **b)** AT, **c)** calculated DIC, **d)** temperature, **e)** in situ spectrophotometric pH, and **f)** calculated pCO$_2$. Sites are individually colored. The solid red line found in subplot **f)** represents the atmospheric pCO$_2$ during the study period.

during spring snowmelt with reduced flows during late summer and winter (i.e., baseflow conditions), a common characteristic of snowmelt dominated catchments (Mast et al. 2006; Raymond et al. 2016). Discharge averaged 23 ± 33 m^3 s^{-1} across the UCFR and ranged from 1.7 to 260 m^3 s^{-1}. Warm Springs recorded the smallest discharge during winter and Turah recorded the largest discharge during spring (Figure 10a). A_T and DIC concentrations decreased by as much as ~3-fold from baseflow to spring snowmelt conditions (Figure 10b,c) and were strongly connected (R^2 values ranged from 0.52 to 0.82, $p<0.05$) with measured discharge (Figure 10a and Appendix B, Figures S4, S5) as is common in snowmelt-dominated systems (Mast et al. 2006; Lynch et al. 2010).

The non-conservative parameters, pH and $p\mathrm{CO}_2$, also correlated with discharge (R^2 ranged from 0.00 ($p>0.05$) to 0.75 ($p<0.05$)) but correlations were dependent on location and season. Riverine pH values along the UCFR also exhibit annual and seasonal oscillations with decreases >1 pH unit from baseflow conditions to spring snowmelt (Figure 10e). pH values were found to converge within ±0.10 pH units across the UCFR during the pH minima of each year (Figure 10e). Riverine $p\mathrm{CO}_2$ values showed increases as large as 4x that of atmospheric levels during spring snowmelt (Figure 10f), whereas other seasons along the UCFR showed $p\mathrm{CO}_2$ values approached atmospheric levels depending on location with a river-wide median of 500 µatm (Figure 10f). This is true for water years 2018 and 2019, however, water years 2020 and 2021 did not illicit the same distinct snowmelt-driven peaks (Figure 10f). Deer Lodge (Figure 8, Table 4) had the highest average $p\mathrm{CO}_2$ (655 ± 193 µatm, $n = 49$) and Warm Springs (Figure 8, Table 4) had the lowest average $p\mathrm{CO}_2$ (375 ± 172 µatm, $n = 48$). Annual ranges (river-wide maximum – river-wide minimum) in $p\mathrm{CO}_2$ were similar ($p>0.05$) for water years 2019, 2020, and 2021 (859 µatm, 724 µatm, and 770 µatm, respectively). The annual range in $p\mathrm{CO}_2$ for water year 2018, however, was twice as large at 1458 µatm. Further, spring and summer had the largest seasonal range in $p\mathrm{CO}_2$ of 1339 µatm and 1137 µatm, respectively, compared to fall and winter with seasonal ranges of 541 µatm and 831 µatm, respectively.

Spatial variability of inorganic carbon along the UCFR is highly dynamic with site-wide averages in A_T and DIC ranging as much as ~1000 µmol L^{-1} among sites (Figure 11a,b). Both A_T and DIC increase steadily from Warm Springs to Garrison by ~1000 µmol L^{-1}. These concentrations stay around 3000 µmol L^{-1} until Bear Gulch and then decrease by ~800 µmol L^{-1} at Turah (due to RC influence; Figure 11, Appendix B, Figure S6). The inflow of tributaries along the UCFR (i.e., LBF, FC, RC; Figure 8, Table 4) were found to impact the concentrations

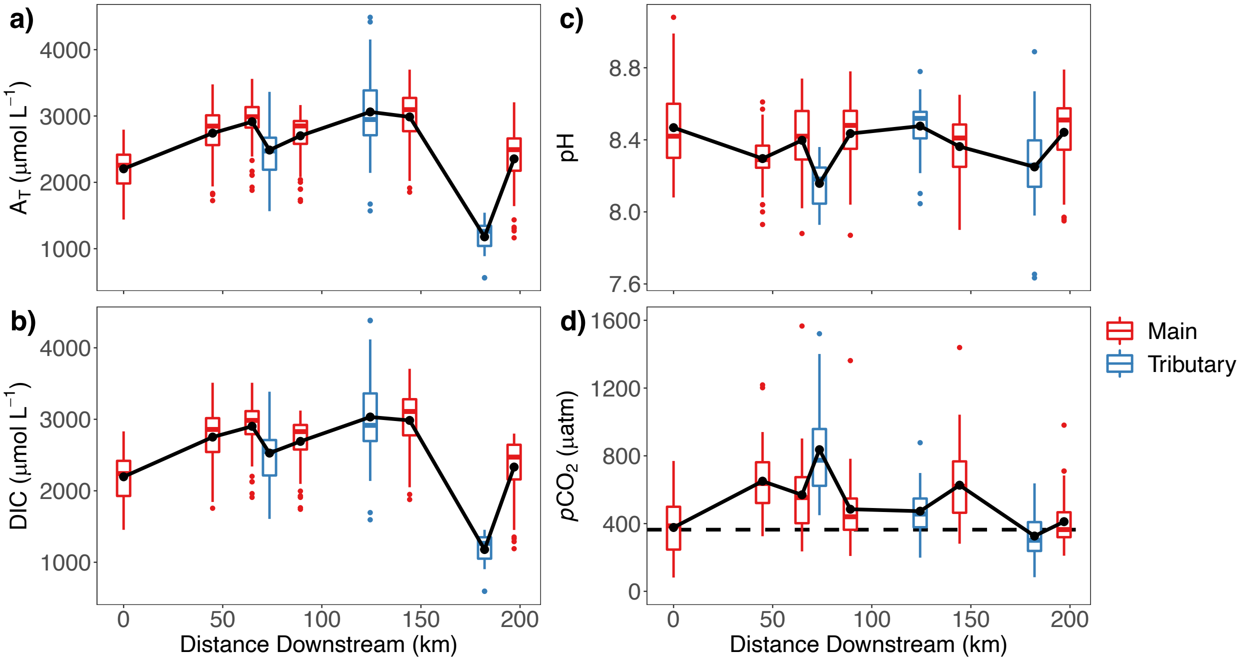

Figure 11. The spatial variability in **a)** A_T, **b)** DIC, **c)** spectrophotometric pH, and **d)** pCO$_2$ at the six sampling locations along the UCFR. The solid black line found in each subplot represents site-wide averages. The dashed black line in subplot **d)** represents the atmospheric pCO$_2$ (~370 µatm) along the UCFR.

of inorganic carbon along the UCFR, especially for A_T and DIC (Figure 11). Tributaries exhibited a wide range of conditions where tributary A_T could reach >4000 µmol L^{-1} (i.e., FC) or as low as <500 µmol L^{-1} (i.e., RC) (Figure 11a and Appendix B, Figure S6). The pH was also found to be highly variable with changes along the UCFR up to 1.2 pH units but without a clear trend up or down in contrast to DIC and A_T (Figure 11c). Tributary pH was highly dynamic (e.g., RC range ~7.6 to ~9.0) but did not influence downstream pH found in the mainstem (Figure 11c and Appendix B, Figure S6). Site-wide averages in pCO$_2$ along the UCFR were found to nearly double from Warm Springs to Deer Lodge and remained elevated until quickly dropping at Turah (Figure 11). Like the other parameters considered above, tributary pCO$_2$ was highly dynamic; LBF and RC had the greatest (860 ± 328 µatm) and least (329 ± 142 µatm) site-wide averages, respectively, compared to the mainstem locations (Appendix B, Figure S6). However, like tributary pH, it did not influence downstream $p\mathrm{CO_2}$ found in the mainstem (Figure 11).

Figures 10 and 11 show $p\mathrm{CO_2}$ along the UCFR near (i.e., Warm Springs and Turah) or above atmospheric $p\mathrm{CO_2}$ levels with a few values found below atmospheric levels. Overall, these findings are comparable with previous studies where streams and rivers are found to be primarily sources of CO_2 to the atmosphere (Richey et al. 2002; Raymond et al. 2013; Rocher-Ros et al. 2019) however, our reported $p\mathrm{CO_2}$ levels are much lower than previously reported values for similar systems. Additionally, studies have also found instances where streams and river exhibit periods sink behavior (i.e., $p\mathrm{CO_2}$ levels below atmospheric levels) even when systems are overall sources of CO_2 to the atmosphere (Minshall, 1978; Dodds, 2006).

Air-water flux of CO_2

Air-water CO_2 fluxes also had large temporal and spatial variability (Figure 12) that appear to follow the hydrograph (Figure 10a) with peaks in efflux during spring snowmelt. Air-water CO_2 flux weakly to moderately correlated with discharge (R^2 ranged from 0.12 to 0.69) dependent on location ($p<0.05$). Air-water CO_2 flux was the largest during water year 2018 with a maximum of 1.2 mol m^{-2} d^{-1} (Figure 12a). This corresponds to the large discharge peak observed in water year 2018 where maximum discharge along the UCFR was twice as high (~300 m^3 s^{-1}) as the following years' peaks. Water years 2019, 2020, and 2021 had considerably smaller peak air-water CO_2 fluxes (0.3, 0.4, and 0.3 mol m^{-2} d^{-1}, respectively). Further, the UCFR had similar minimum air-water CO_2 flux values across water years of -0.1 mol m^{-2} d^{-1}, -0.09 mol m^{-2} d^{-1}, -0.1 mol m^{-2} d^{-1}, and -0.07 mol m^{-2} d^{-1} for the four respective water years and suggest periods of sink behavior along the UCFR. Air-water CO_2 flux along the UCFR averaged

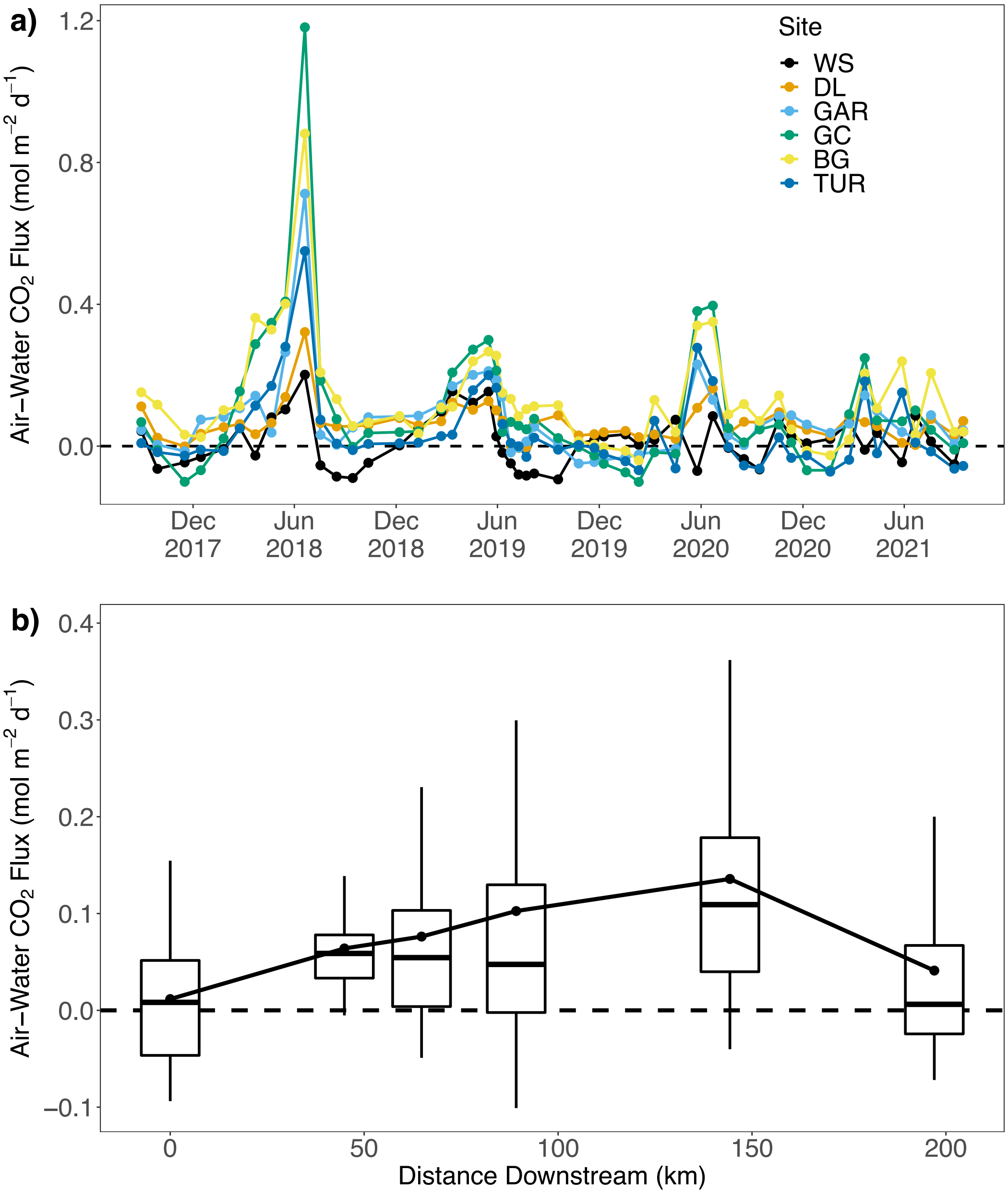

Figure 12. a) The time series air-water CO_2 flux data for each sampling site during the duration of study. **b)** The spatial variability of air-water CO_2 flux along the UCFR. Outliers were removed to better see the downstream variability of air-water CO_2 flux. Outliers ranged from 0.2 to 1.2 mol m^{-2} d^{-1} along the UCFR. The solid black circles with connecting line represent site-wide averages and the black dashed lines in **a)** and **b)** indicate no net exchange with the atmosphere.

0.08 ± 0.14 mol m^{-2} d^{-1} ($n = 275$). Spatial dynamics of air-water CO_2 flux along the UCFR indicate an average increase from Warm Springs to Bear Gulch and then decrease to near atmospheric equilibrium at Turah (Figure 12b), following a similar trend to pCO_2 (Figure 11d). Over the four water years the estimated air-water CO_2 flux values for the UCFR were above zero 76% of the time with periods of negative air-water CO_2 flux representing 24%. Thus, over this time, the UCFR was found to primarily be a source of CO_2 to the atmosphere with periods of sink behavior during the summer and winter (Figure 12a).

Biogeochemical regulation of inorganic carbon and air-water CO_2 flux

The DIC saturation (Eq. 8) relative to the atmosphere (Figure 13) and property-property correlations (Figure 14) showed that DIC along the UCFR was typically in excess relative to the atmosphere (Figure 13) and is influenced by seasonal fluctuations in discharge and temperature (Figure 14). Individual sites (Figure 13a) and reaches (Figure 13b) were found to exhibit periods of both undersaturation and oversaturation of DIC. Most sites were supersaturated with DIC during spring, summer, and winter except for Warm Springs and Turah which were consistently undersaturated during summer (Figure 13a). Warm Springs was found to be the most undersaturated with respect to DIC during the summer by -111 $\mu mol\ L^{-1}$, while Garrison was found to be the most supersaturated during spring by 79 $\mu mol\ L^{-1}$ (Figure 13a). Note that Gold Creek and Bear Gulch are also largely supersaturated by 63 and 71 $\mu mol\ L^{-1}$, respectively (Figure 13a). This appears to correspond with Figures 10 and 12 where Warm Springs has the lowest DIC concentration and air-water CO_2 flux, while Garrison, Gold Creek, and Bear Gulch have the highest DIC concentrations and air-water CO_2 flux.

At the reach scale ($\Delta\Delta$DIC, Figure 13b), a transition along the UCFR (i.e., Reach I to Reach V) occurs from a supersaturated system ($\Delta\Delta DIC>0$) to an undersaturated system ($\Delta\Delta DIC<0$) from upstream to downstream. Recall that Warm Springs (start member to Reach I) is largely undersaturated in DIC. Thus, for Reach I to become largely supersaturated downstream indicates the potential for allochthonous sources of DIC to heavily influence this reach. This reach in the past has been suspected to have significant groundwater influences (Kyro, 2021) and is a potential explanation for the observed variability in DIC saturation for Reach I (Figure 13).

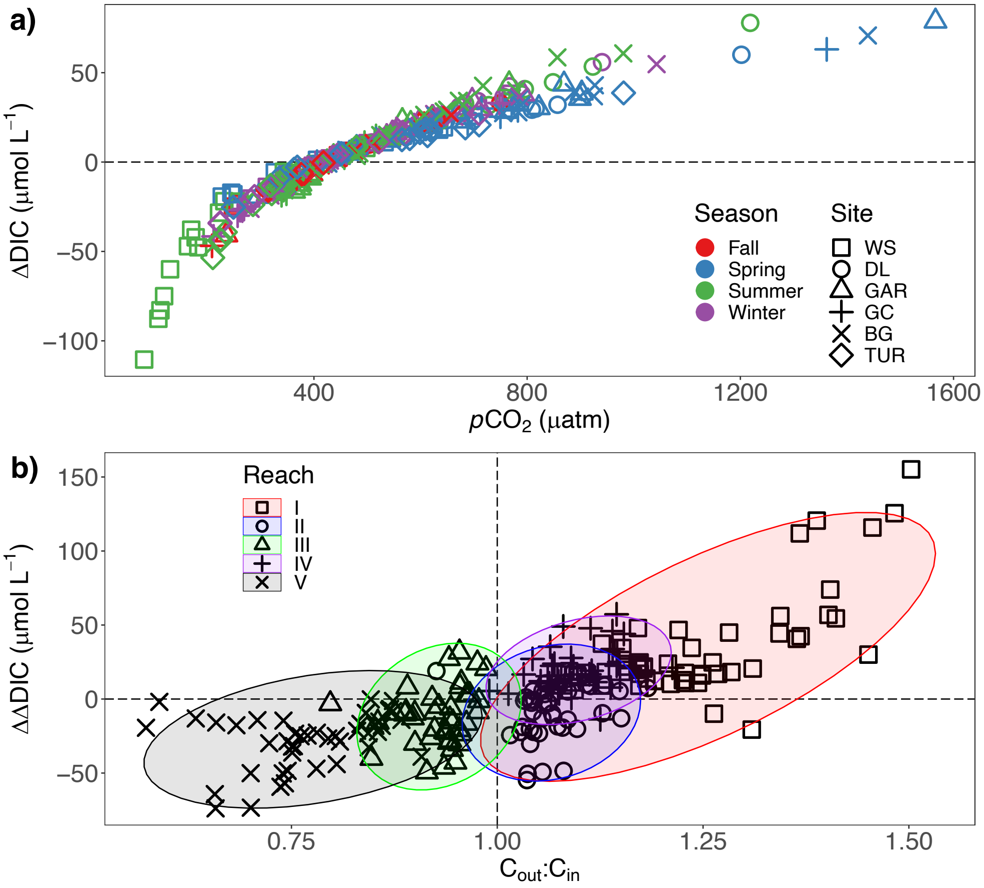

Figure 13. a) The difference in DIC at atmospheric saturation (ΔDIC) to DIC at calculated pCO$_2$ levels using the same A_T and temperature. Unique points represent individual sites (shape) and season (color). **b)** The relationship between the relative concentration of DIC in each reach (C_{out}:C_{in}) and the change in ΔDIC ($\Delta\Delta$DIC) between sites (i.e., Reach I-V). Unique points represent individual reaches and are grouped by ellipses also denoted by reach. Horizontal and vertical lines represent zero change in ΔDIC (i.e., at equilibrium with the atmosphere) and no change in riverine DIC between downstream and upstream sites, respectively.

Property to property Pearson correlations (r) of inorganic carbon parameters, temperature, discharge, and atmospheric pCO$_2$ show striking seasonal river-wide trends over four water years in the UCFR (Figure 14). Site-specific correlations were found to be moderately-strong over the four water years for select inorganic carbon parameters (Appendix B, Figure S7). Overall, the

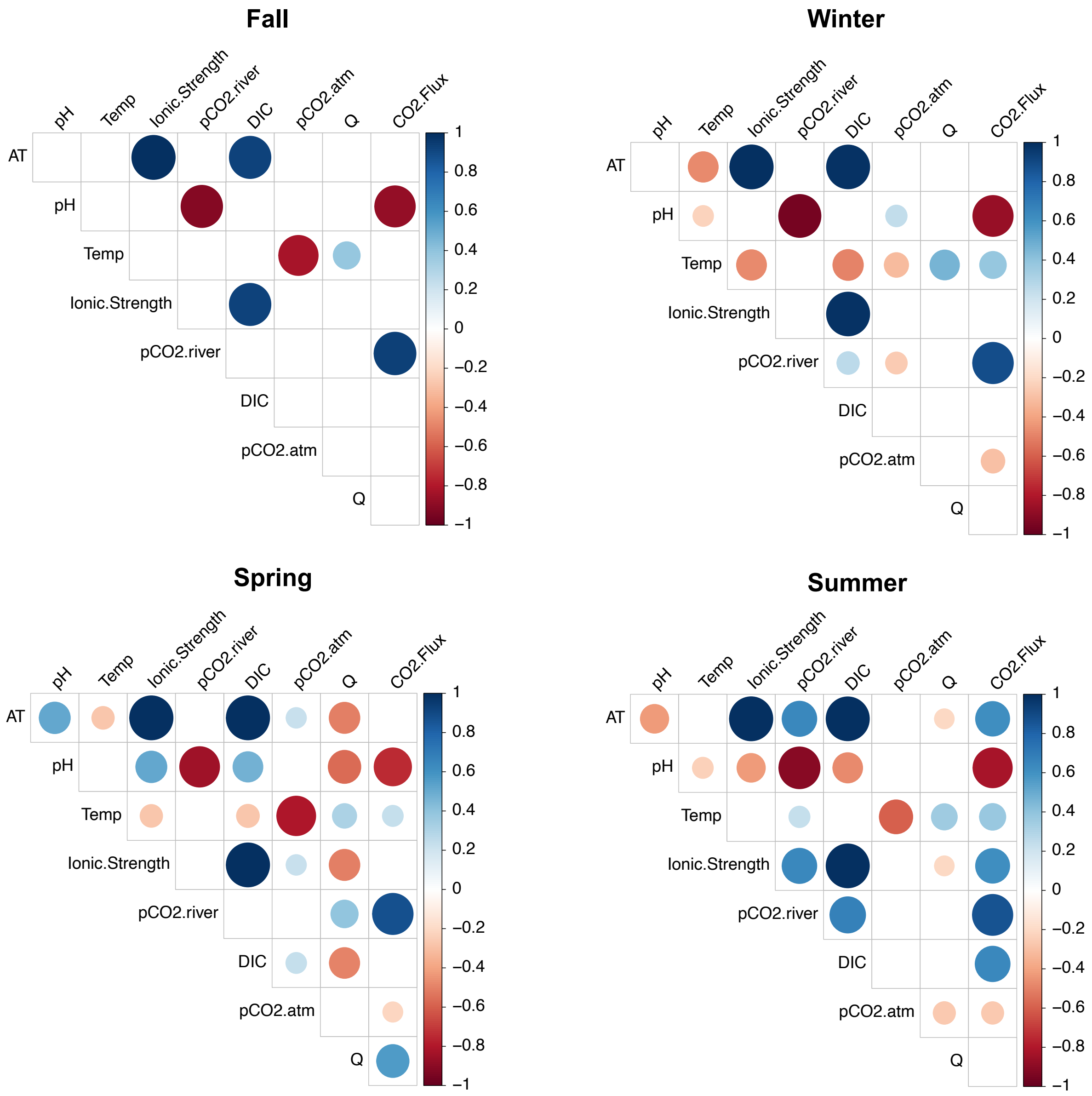

Figure 14. A series of seasonal correlograms (Fall, Spring, Summer, Winter) used to depict the relationships among different inorganic carbon parameters, temperature, and discharge for four water years of data in the UCFR. Average values across the six sampling locations were used for this analysis. "pCO2.atm" represents the atmospheric $p\text{CO}_2$ level (Figure 10f), "pCO2.river" represents the riverine $p\text{CO}_2$ level (Figure 10f), "Flux" refers specifically to the air-water CO_2 flux (mol m^{-2} d^{-1}) (Figure 11), and "Q" refers to discharge (m^3 s^{-1}) (Figure 10a). Circles within boxes are both colored and sized to illustrate the Pearson correlation (r) of each relationship. Boxes void of circles indicate a non-significant relationship based on an alpha level of 0.05.

UCFR appears to become more “homogenous” as the seasons progress from fall to spring, meaning that fall has the least significant correlations among all parameters (8), and spring has the most (25) (Figure 14). Additionally, fall shows that most of the significant correlations are only between inorganic carbon parameters (Figure 14). This highlights that not many other variables (i.e., temperature, discharge) impact inorganic carbon during this time (Figure 14).

As the season progresses to winter, more significant correlations take shape (Figure 14). Included in this is the increase in temperature related correlations where the colder winter conditions (see Figure 10d) appear to be negatively correlated with ionic strength (r = -0.48), DIC (r = -0.50), and atmospheric $p\mathrm{CO_2}$ (r = -0.32); yet positively correlated with discharge (r = 0.46) and air-water $\mathrm{CO_2}$ flux (r = 0.38) (Figure 14). As the seasonal progression continues, spring shows similar temperature correlations but now with an increase in discharge, $\mathrm{A_T}$, DIC, pH, and air-water $\mathrm{CO_2}$ flux related correlations (Figure 14). The increase in discharge related correlations support the observed trends in $\mathrm{A_T}$, DIC, pH and $p\mathrm{CO_2}$ (Figure 10 and Appendix B, Figures S4, S5) for when spring snowmelt effectively influences each variable. Additionally, discharge becomes positively correlated with air-water $\mathrm{CO_2}$ flux (r = 0.56). Note that discharge is negatively correlated with DIC (r = -0.49) and so the correlation between discharge and air-water $\mathrm{CO_2}$ flux is likely driven by increased gas transfer velocities and declining pH values during spring (Figure 10 and Appendix B, Figure S2) and not from increased DIC loads.

As the UCFR transitions into the growing season (i.e., summer), more significant correlations appear between air-water $\mathrm{CO_2}$ flux and other variables (Figure 14). Importantly, DIC is only correlated with air-water $\mathrm{CO_2}$ flux (r = 0.65) and riverine $p\mathrm{CO_2}$ (r = 0.68) during the summer suggesting a biological influence on $p\mathrm{CO_2}$ and air-water $\mathrm{CO_2}$ flux not apparent in the other seasons (Figure 14). Further, during summer the air-water $\mathrm{CO_2}$ flux becomes significantly correlated ($p<0.05$) with all parameters except for discharge (Figure 14). Additionally, the warmer summer conditions (see Figure 10d) appear to influence air-water CO_2 flux ($r = 0.37$) similar to winter ($r = 0.38$) (Figure 14). This highlights the role that maximum (~20°C) and minimum (~0°C) riverine temperatures have on air-water CO_2 flux estimates due to the solubility of CO_2 (i.e., K_H`; equation 10).

Discussion

The high precision and accuracy of measured freshwater spectrophotometric pH and A_T provided this study with high quality calculated freshwater inorganic carbon parameters. The increased accuracy in $p\mathrm{CO_2}$ allowed us to quantify air-water CO_2 fluxes better than before over four water years along ~200 km of the UCFR. Additionally, the high precision of measured pH, A_T, and calculated $p\mathrm{CO_2}$ made it possible to resolve spatial and temporal inorganic carbon gradients in freshwater better than before. This is especially true for freshwater pH where pH is typically measured electrochemically; a method that is known to provide erroneously low pH values (Hunt et al. 2011; Abril et al. 2015; Liu et al. 2020; Young et al. 2022). However, due to the accuracy of spectrophotometric pH (<0.008 pH units; Yuan and DeGrandpre, 2008; Lai et al. 2016; Young et al. 2022) this study was able to resolve small spatial changes in pH (Figure 10) not captured before from discrete measurements.

Past studies have shown overwhelming evidence for inland waters, especially rivers, acting as sources of CO_2 to the atmosphere (Aufdenkampe et al. 2011; Butman and Raymond, 2011; Raymond et al. 2013; Rocher-Ros et al. 2019; Liu and Han, 2021). Raymond et al. (2013) found that 95% of the global streams and rivers had a median calculated $p\mathrm{CO_2}$ greater than atmospheric values where the median value was found to be ~3100 μatm. Moreover, other studies have reported $p\mathrm{CO_2}$ values ranging from ~90 μatm in the Maotiao River (Wang et al.

2011) to as high as 44000 μatm in the Amazon River (Richey et al. 2002; Liu and Han, 2021). This places the pCO_2 values reported here for the UCFR at the lower end of this range and nearly a sixth of the global median (UCFR median of 500 μatm). In general, the UCFR was also found to act as a significant source of CO_2 to the atmosphere (Figure 12). However, despite the UCFR maintaining high concentrations of A_T and DIC (Figure 10), periods of sink behavior (i.e., air-water CO_2 flux<0) were observed during summer and winter months (Figure 12). From the literature, we know that most rivers tend to be net heterotrophic (i.e., greater respiration than production) (Minshall, 1978; Thorp and Delong, 2002; Dodds, 2006). However, in the UCFR we find that during the growing season (i.e., summer) primary production can drive pCO_2 below atmospheric levels creating a CO_2 sink dependent on location and season (Figure 10-12). In fact, all locations studied along the UCFR recorded several instances of negative air-water CO_2 fluxes (Figure 12) during all seasons. Of the 67 negative air-water CO_2 flux values, 73% occurred during summer and winter primarily at Warm Springs and Turah.

Inorganic carbon (i.e., A_T, DIC, pH, pCO_2) and air-water CO_2 flux were found to be highly dynamic with annual peaks and valleys following increased snowmelt due to increases in discharge. This is a common characteristic of conservative solutes in snowmelt dominated catchments (sulfate, chloride, calcium, alkalinity; Mast et al. 2016) and has been shown for non-conservative parameters as well (i.e., pH, pCO_2, air-water CO_2 flux; Hélie et al. 2002). A_T, for example, is highly conservative along the UCFR with a single source (i.e., groundwater) that is diluted or concentrated proportionally from precipitation and evaporation, respectively (Shangguan et al. 2021). Thus, when snowmelt enters the UCFR during spring, this brings in ~0 A_T water and effectively dilutes the river. Therefore, sharp valleys appear in the timeseries for A_T during spring each year (Figure 10). Conversely, once snowmelt is over, A_T quickly recovers to pre-dilution values due to the constant supply of highly concentrated groundwater. Additionally, pH was also found to decrease during annual snowmelt along with A_T and DIC (Figure 10). Modeled dilution of A_T and DIC from 3000 μmol L^{-1} to 1000 μmol L^{-1} (approximate range taken from Figure 10) was estimated to decrease pH by only ~0.03 pH units (modeled in CO2SYS; Lewis and Wallace, 1998). However, pH along the UCFR could decrease by ~0.8 pH units during spring snowmelt (e.g., water year 2018; Figure 10) and so other biogeochemical processes likely contributed to the observed decrease in pH. For instance, the lower buffer capacity (i.e., diluted A_T) and the addition of organic acids from increased dissolved organic carbon loads (commonly found during spring snowmelt, e.g., Hood et al. 2006; Mast et al. 2016) to the river during this time could also contribute to lower observed pH values (Figure 10). Consequently, $p\mathrm{CO}_2$ values were found to increase during snowmelt periods (Figure 10; ~June of each year) due to the inverse relationship between calculated $p\mathrm{CO}_2$ and pH where low pH generates high $p\mathrm{CO}_2$ values (Stumm and Morgan, 2008; Liu et al. 2020; Young et al. 2022). Riverine $p\mathrm{CO}_2$, however, is controlled by additional biogeochemical processes (e.g., gas exchange, respiration, primary production) and so the observed variability outside of seasonal snowmelt (Figure 10) is likely due to photosynthesis and respiration during the growing season. Accordingly, GPP and ER estimates along the UCFR during the summer of 2020 were found to be representative of a productive mid-order river with values of 0.25 ± 0.10 mol C m^{-2} d^{-1} and -0.26 ± 0.08 m C m^{-2} d^{-1}, respectively (DeGrandpre and Valett, unpubl.) and are comparable to other productive temperate rivers (Uehlinger, 2006; Appling et al. 2018a; Koenig et al. 2019). Additionally, estimated net ecosystem production (NEP = -0.013 mol C m^{-2} d^{-1}) indicates a net heterotrophic system (Lynch et al. 2010) and signifies the substantial influence of respiration on inorganic carbon dynamics, especially $p\mathrm{CO}_2$ and DIC along the UCFR as discussed above.

Inorganic carbon along the UCFR is also highly spatially variable with large gradients that are both locally and tributary driven (Figure 11). The strong influence of tributaries to these parameters is, again, due to the conservative behavior of A_T and DIC from dilution/enrichment. For example, RC has a much lower average A_T and DIC (~1000 µmol L^{-1}) compared to Bear Gulch (~3000 µmol L^{-1}; upstream of RC) (Figure 11). Therefore, the low concentration tributary water dilutes the mainstem and causes the concentration of A_T and DIC at Turah to be much lower (~2200 µmol L^{-1}; downstream of RC) (Figure 11). In contrast, other parameters such as pH and $p\mathrm{CO}_2$ are not as influenced by tributary inputs and appear to be spatially independent (Figure 11). Thus, localized processes such as GPP and ER along with temperature and gas exchange, discussed above, are likely contributing more to the spatial variability of pH and $p\mathrm{CO}_2$ along the UCFR. Air-water CO_2 fluxes along the UCFR gradually increased from Warm Springs to Bear Gulch until returning near zero at Turah (Figure 12). Midstream sites (i.e., Deer Lodge, Garrison, Gold Creek, and Bear Gulch) had larger absolute air-water CO_2 flux values compared to Warm Springs and Turah and were found to be driven by riverine $p\mathrm{CO}_2$ levels (Figures 10-13).

Most sites along the UCFR were found to be oversaturated in DIC during all seasons (Figure 13). Warm Springs and Turah, again, were found to be mostly undersaturated in DIC during the summer which corresponds with increased autochthonous production and near zero to negative air-water CO_2 flux values observed for these sites (Figure 12). In contrast, sites such as Garrison, Gold Creek, and Bear Gulch were supersaturated in DIC during spring (Figure 13) due to the relatively high concentrations of DIC at these locations even after dilution (Figure 12). Reach scale dynamics of ΔDIC illustrate a transition from supersaturated (Reach I) to near equilibrium (Reaches II-IV) to undersaturated (Reach V) along the UCFR (Figure 13). Recall that ΔΔDIC indicates changes in ΔDIC as you move downstream (Figure 13). Interestingly, Reach I is the only reach with such a large positive change in ΔDIC. This transition from undersaturation to oversaturation in DIC is likely due to allochthonous inputs of DIC-rich groundwater influencing Reach I (Warm Springs to Deer Lodge) year-round.

Seasonal correlograms provided additional insight into the temporal controls on inorganic carbon and air-water CO_2 fluxes along the UCFR (Figure 14). Springtime induced the most significant correlations where discharge was found to significantly correlate ($p<0.05$) with all inorganic carbon parameters including air-water CO_2 flux (Figure 14). Interestingly, summer was the only time when DIC significantly correlated ($p<0.05$) with air-water CO_2 flux and is likely due to increased respiration contributing substantially to the DIC pool and riverine pCO_2. Additionally, an increase in significant correlations between temperature and inorganic carbon parameters during baseflow conditions demonstrates the cooling (winter) and heating (summer) effect on the solubility of CO_2 (i.e., K_H`) (Figure 14). This has been shown to significantly affect pCO_2 in the UCFR in the past (Lynch et al. 2010). Appendix B (Figure S8) shows the average temperature-driven pCO_2 of the UCFR for this study following methods outlined in Takahasi et al. (2002) and Lynch et al. (2010). In general, there appears to be a phase shift between calculated pCO_2 and temperature-driven pCO_2 (Appendix B, Figure S8). During the peak of summer when temperature is at its greatest, we generally see low pCO_2 values compared to high temperature driven pCO_2. Note that pCO_2 increases with increasing temperature because of the decreased solubility of CO_2 and the increase in aqueous CO_2 from the bicarbonate equilibrium (Lynch et al. 2010; Middleburg, 2019). Low pCO_2 values during the height of summer suggest that high rates of photosynthesis are depleting aqueous CO_2 (Figures 10, 13, 14 and Appendix B,

Figure S8) as discussed above. During the winter months, however, riverine pCO_2 matches well with the temperature-driven pCO_2 indicating significant cooling effects on pCO_2 dynamics and consequently, air-water CO_2 fluxes in the UCFR (Figure 14 and Appendix B, Figure S8).

Conclusion

This study characterized the temporal and spatial drivers that regulate inorganic carbon and air-water CO_2 fluxes along the UCFR using accurate measures of spectrophotometric pH, A_T, and accurate computations of pCO_2 and air-water CO_2 fluxes. We found that these drivers primarily included discharge, tributary influence, temperature, and metabolic processes (i.e., GPP and ER) and were spatially and seasonally dependent. The UCFR was mainly a source of CO_2 to the atmosphere with an average of 0.08 ± 0.14 mol m^{-2} d^{-1} and reported increases during spring snowmelt as large as 1.2 mol m^{-2} d^{-1}. The average air-water CO_2 flux is comparable to the minimum stream values reported around the world (Telmer and Veizer, 1999; Abril et al. 2005; Zou, 2017; Li et al. 2012; Liu and Han, 2021) whereas the reported 1.2 mol m^{-2} d^{-1} value is more comparable to maximum values reported for much larger rivers including the Amazon River, Mekong River, and Xijiang River (Alin et al. 2011; Liu and Han, 2021). The UCFR also acted as a CO_2 sink during the summer and winter months when 24% of the data reported negative air-water CO_2 flux values.

The utility of spectrophotometric pH for freshwater application is starting to become clear over the past decade (Lynch et al. 2010; Lai et al. 2016; Young et al. 2022). As more studies begin to utilize the increased accuracy provided by spectrophotometric pH for calculating pCO_2, monitoring freshwater pH, etc. clearer insights into biogeochemical processes that regulate inorganic carbon in freshwater systems can be obtained. Here, spectrophotometric pH was ultimately used to estimate air-water CO_2 fluxes in a productive, mid-order montane river with moderate levels of pCO_2 (Raymond et al. 2013). Additional studies are needed, however, in larger systems with higher levels of pCO_2 to further evaluate the utility of spectrophotometric pH in calculating freshwater pCO_2 used to estimate air-water CO_2 fluxes.

CHAPTER 4

Carbon Processing Domains: Seasonal and spatial controls on organic carbon in a montane river

Introduction

Riverine organic carbon (C) has been extensively studied for several decades (Montoura and Woodward, 1983; Mann and Wetzel, 1995; Raymond and Bauer, 2001; Baum et al. 2007; Hilton et al. 2008; D'Andrilli et al. 2015; Shogren et al. 2021) and studies have focused on organic C quality, quantity, and transport. Dissolved organic C (DOC) acts as a basal resource for aquatic food webs and contributes to the chemistry of aquatic systems through the acidity of organic acids, metal chelation, and other processes. As an energy source, the bioavailability of DOC has been shown to limit microbial community production and impact aquatic food webs from the bottom-up (Jansson et al. 2000; Finlay, 2001; Thorp and Delong, 2002; Westhorpe et al. 2010; Baldwin et al. 2016). DOC is also a major source of C to the coastal oceans (Holmes et al. 2008; Dai et al. 2012), can control light availability in the water column (i.e., blackwaters; Aldridge et al. 1998; Phlips et al. 2007), and can influence inorganic C parameters (e.g., total alkalinity, partial pressure of CO_2) (Hunt et al. 2011; Liu et al. 2020; Young et al. 2022).

Many studies have focused on understanding the spatial and temporal variability of DOC in freshwater systems (Raymond and Bauer, 2001; Bianchi et al. 2004; Jaffé et al. 2008). The major sources and sinks of DOC include instream biological production and respiration (Drakare et al. 2002; Amon and Benner, 1996; Berggren et al. 2010; Jones et al. 2016), floodplain connectivity (Tockner et al. 1999; Atkinson et al. 2019; Lynch et al. 2019), allochthonous inputs (Pagano et al. 2014; Lynch et al. 2019), precipitation (Dawson et al. 2011; Mast et al. 2016), and photo-degradation (Cory et al. 2014; Jones et al. 2016). These studies exemplify the complex cycling of DOC in freshwater systems. Nevertheless, several conceptual models including the Flood Pulse Concept (Junk et al. 1989), the Riverine Productivity Model (Thorp and Delong 1994), and the Pulse Shunt Concept (Raymond et al. 2016) have been pursued towards understanding the hydrologic, chemical, and biological processes that significantly alter organic C in lotic systems.

The Flood Pulse and Pulse Shunt conceptual frameworks describe the effectiveness of interaction with the landscape in regards to transporting solutes into the river following inundation or precipitation, respectively (Junk et al. 1989; Raymond et al. 2016). The Flood Pulse Concept was derived with large, tropical rivers in mind but has been broadly applied to emphasize that long, predictable periods of high discharge provide organic matter (including DOC) from adjacent floodplains that is more labile than that derived from upstream import. Spring snowmelt and localized precipitation can trigger pulses of terrestrially derived DOC into drainage networks (Hornberger et al. 1994; Boyer et al. 1997; Raymond et al. 2016). Imported DOC can then be shunted (i.e., transported with minimal degradation) downstream to higher-order rivers far removed from the point of origin where it promotes biological activity and influences biogeochemical processes. These frameworks have provided the basis for enhanced DOC watershed biogeochemical modeling and have led to a deeper understanding of linkages to processes like ecosystem metabolism (e.g., Ulseth et al. 2018) and C fluxes (Raymond et al. 2016).

Others have emphasized the progression of ecosystem function following high flows (Fisher et al. 1982; Kaushal and Belt, 2012) and spring snowmelt in particular (Baker et al. 2000; Lowery et al. 2010; Yarnell et al. 2010). While evidence suggests that biological activity is relevant to C form and abundance during other times (Hood et al. 2006; Lynch et al. 2010; Mast et al. 2016), instream processes can significantly alter these features during baseflow growing seasons (Thorp and Delong; Westerhoff and Anning 2000; Stanley et al. 2012; Jones et al. 2016). Thorp and Delong's (1994) riverine productivity models emphasize the influence of autochthonous processes on carbon production and its importance for riverine food webs including DOC supplied during periods not limited to flood pulses. It is pertinent to understand how rivers respond both to pulse events and how DOC is processed and transported during periods of low flow.

Nutrient processing domains—application for DOC dynamics

Recently, Valett et al. (2022) presented Nutrient Processing Domains (NPD) as a budgetary approach for assessing riverine nutrient cycling where changes in nutrient concentration and mass are quantified at the section (i.e., km of river distance) scale. This classification system utilizes changes in discharge normalized to streambed area, material loads, and concentration to assess nutrient dynamics longitudinally among lengths of river reflecting landscape dynamics. This approach provides a novel way to assess biogeochemical solute variability over large scales with the capacity to simultaneously address hydrologic and biological influences, adding to the suite of conceptual frameworks discussed above.

Processing domains are defined in the hydrologic literature as the regions within which one or more geologic processes prevail in the processing and transport of mass (Montgomery, 1999; Brardinoni and Hassan, 2006). These domains have been delineated by fundamental characteristics like the local slope gradient and drainage area. In applying this approach to river systems, Valett et al. (2022) argued that each reach or section can be organized in functional space by the processes controlling whether that reach functions as a net source or sink for any given material, changes in its relative availability, and the propensity for hydrological exchange

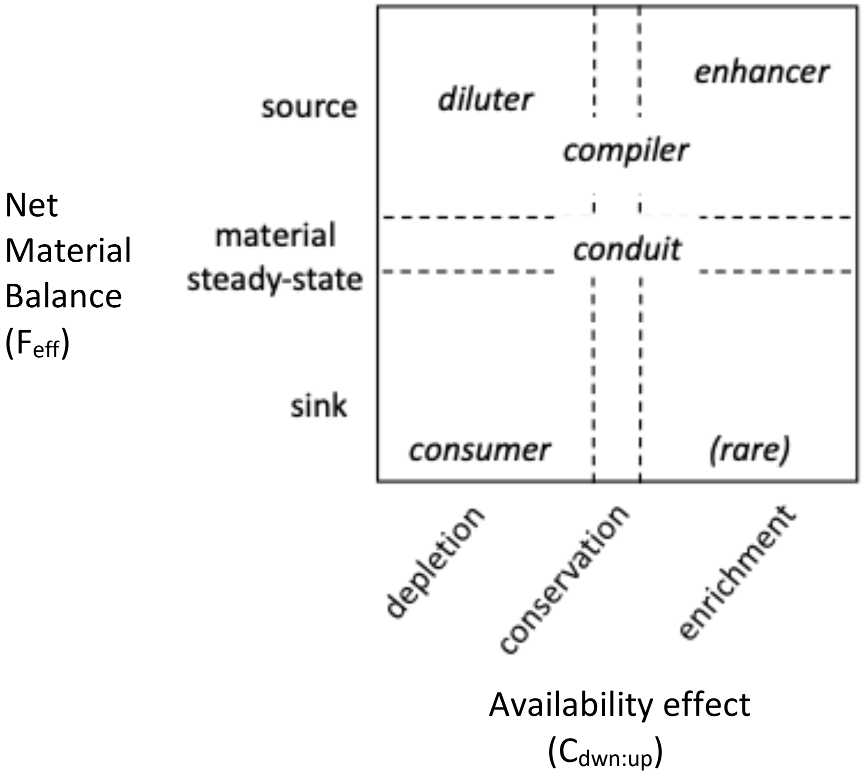

Figure 15. The processing domain conceptual framework defined by measures of net material balance (F_{eff}) and the availability effect ($C_{dwn:up}$) from Valett et al. (2022). Dashed lines denote boundaries of functional space and do not differ from the null values for $C_{dwn:up}$ (conserved concentration = 1) and F_{eff} (material steady state = 0).

to influence material budgets (Figure 15). Based on these characteristics, Valett et al. (2022) described five distinct processing domains including diluter, enhancer, consumer, conduit, and compiler. Three of these domains (i.e., diluter, enhancer, and consumer) describe conditions under which material budgets are not at steady state and solute concentrations are not being conserved. Reaches are diluters when downstream load increases, but solute concentrations decrease. Additionally, reaches are either enhancers or consumers when both downstream load and solute concentrations either increase or decrease, respectively. Under conditions of material steady-state and conserved concentrations, reaches reside in the conduit domain. Compilers, like conduits, conserve concentration but loads increase congruent with hydrologic gain.

While the NPD approach was initially created with nutrients in mind, it may prove useful for describing the spatiotemporal variability of a variety of solutes that may be more conservative (i.e., DOC, dissolved inorganic C, metals) or equally dynamic (i.e., hydrogen ion, partial pressure of carbon dioxide) in character. In the current study, we apply the NPD approach to DOC, to describe and interpret functional carbon processing domains (CPDs) along the upper Clark Fork River, MT, USA. Here, we extend beyond simple classification of reaches as emphasized by Valett et al. (2022) and leverage the quantitative relationship between key measures of biogeochemical character to gain insight into the relative roles of transport and reaction in governing DOC dynamics across river sections in a productive, mid-order montane river.

Quantifying C biogeochemical character

In this study, measures of C transport and processing are derived from DOC concentrations, discharge, and reach area. Parameters involved include changes in concentration ($C_{\mathrm{dwn:up}}$; unitless), discharge (ΔQ; m^3 s^{-1}), hydraulic load (ΔHL; m d^{-1}), and material load (ΔLoad; mol s^{-1}), along with derived measures of the effective solute flux (F_{eff}; mol m^{-2} d^{-1}). Changes in the concentration of DOC along each section ($C_{\mathrm{dwn:up}}$) is calculated as the ratio of downstream to upstream DOC concentration (C_{dwn} and C_{up}, respectively, Eq. 10).

$$C_{\mathrm{dwn:up}} = \frac{C_{\mathrm{dwn}}}{C_{\mathrm{up}}} \tag{10}$$

Reaches with $C_{\mathrm{dwn:up}}$ values >1, =1, and <1 represents those that are enriched, conserved, or depleted of DOC, respectively. This relative concentration describes an 'availability effect' (Figure 15; Valett et al. 2022) as it represents the relative change in DOC abundance in the water column and its availability to riverine biota using a measure that can be directly compared across reaches.

Changes in discharge (ΔQ) is calculated by the difference in flow between a downstream and upstream site (Eq. 11):

$$\Delta Q = Q_{dwn} - Q_{up} \tag{11}$$

where Q_{dwn} and Q_{up} represent the downstream and upstream discharge, respectively. Values for $\Delta Q>0$ indicate a gaining reach, i.e., net addition to flow, whereas $\Delta Q<0$ indicates a losing reach, i.e., net loss to the underlying aquifer. To track the loading of water through each reach, the change in hydraulic load (ΔHL) is determined by differences in discharge normalized by wetted reach area (A_w) (Eq. 12).

$$\Delta HL = \frac{\Delta Q}{A_w} \tag{12}$$

Hydraulic load is a term frequently employed in wetland studies (Kadlec and Wallace, 2009) that effectively normalizes flow change by the area of a reactive surface reflecting accumulation (or loss) of depth along the reach. It additionally, allows for the comparison among reaches as lengths and absolute discharge values vary.

The change in load (ΔLoad) is calculated by the difference between the products of discharge and concentration at downstream and upstream sites (Eq. 13)

$$\Delta Load = (C_{dwn} \times Q_{dwn}) - (C_{up} \times Q_{up}) \tag{13}$$

where C_{dwn} and C_{up} represent the downstream and upstream DOC concentration (μmol L^{-1}), respectively. ΔLoad can then be normalized to the wetted area (A_w) to describe the areal rate of net DOC accumulation or loss from the water column along the reach as the effective flux of DOC (F_{eff}; Eq. 14). F_{eff}, therefore, represents the net rate of DOC gain or loss per unit wetted area resulting from both advective and biotic processes in each reach (Valett et al. 2022).

$$\mathrm{F_{eff}} = \frac{\Delta \mathrm{Load}}{\mathrm{A_w}} \tag{14}$$

Equations 13 and 14 indicate that F_{eff} is controlled by changes in discharge and concentration along the reach. Changes in discharge are captured as ΔQ and may reflect the influences of tributaries or exchange with groundwater. Changes in DOC concentration can be due to allochthonous inputs (e.g., via tributaries, groundwater) or autochthonous biological processes that consume or produce DOC. Accordingly, deconstructing F_{eff} to reflect advective and biological influences yields equation 15:

$$\mathrm{F_{eff}} = \frac{\Delta \mathrm{L_{tg}} + \Delta \mathrm{L_{bio}}}{\mathrm{A_w}} = \frac{\Delta \mathrm{Q} \times \mathrm{C_{tg}}}{\mathrm{A_w}} + \frac{\Delta \mathrm{L_{bio}}}{\mathrm{A_w}} \tag{15}$$

where ΔL_{tg} is the change in DOC load due to allochthonous inputs, C_{tg} is the mean DOC concentration of tributaries and groundwater, and ΔL_{bio} is the net change in load due to instream biological processing. Equation 15 can be simplified by substituting in equations 12 and 14 to reveal how the effective solute flux of DOC (F_{eff}) is related to change in the hydraulic load (ΔHL), allochthonous inputs (C_{tg}), and instream biological processing (F_{bio}) (Eq. 16):

$$\mathrm{F_{eff}} = \Delta \mathrm{HL} \times \mathrm{C_{tg}} + \mathrm{F_{bio}} \tag{16}$$

It is important to note that F_{bio} is equivalent in magnitude (but opposite in sign) to measures of biological DOC uptake (i.e., respiration) provided in the literature (Bernhardt and Likens, 2002; Ensign and Doyle, 2006; Garnier and Billen, 2007; Valett et al. 2022). Thus, a $-F_{bio}$ value indicates a loss of DOC from the water column due to biotic respiration and a $+F_{bio}$ value indicates DOC added to the water column via biotic pathways such as photosynthetic exudates (Soares et al. 2017). Additionally, a positive or negative sign associated with F_{eff} characterizes a reach as either a material source or sink, respectively.

Equation (16), thus, represents a linear quantitative relationship between the propensity for a reach to act as a source or sink (F_{eff}) and the change in flow normalized to reach area (ΔHL). The slope of the line from this quantitative relationship represents the concentration of DOC in waters exchanging with the reach (C_{tg}) and the intercept provides the magnitude of the net biological flux influencing DOC concentrations (F_{bio}). Our current analysis of CPDs in the upper Clark Fork River, MT, USA exploits this quantitative relationship to assess the relative roles of transport and reaction in dictating DOC dynamics. Here, we focus on contrasting behaviors associated with periods of elevated flow and baseflow conditions characteristic of the annual cycle of ecosystem dynamics in a snowmelt-driven river.

Material and methods

Study sites

This study took place along ~215 km of the upper Clark Fork River (UCFR), MT, USA starting at Warm Springs, MT and ending in Missoula, MT (Figure 16, Table 5). The UCFR drains a 57,000 km^2 catchment and is a productive mid-order river but also one of the largest superfund sites in the United States, with a legacy of heavy metal pollution (Moore and Luoma, 1990; Parker et al. 2007; Moore and Langner 2012). The UCFR was sampled at 13 main stem locations and three tributary locations (Figure 16, Table 5). This was further divided into reach segments I-V based on the location of U.S. Geological Survey (USGS) stream gaging stations (Figure 16, Table 5). This study focuses on a dataset comprised of 656 DOC measurements spanning 36 months (52 sampling events) starting in October 2018 and ending in September 2021. Discharge measurements were taken from six USGS gaging stations (Figure 16, Table 5).

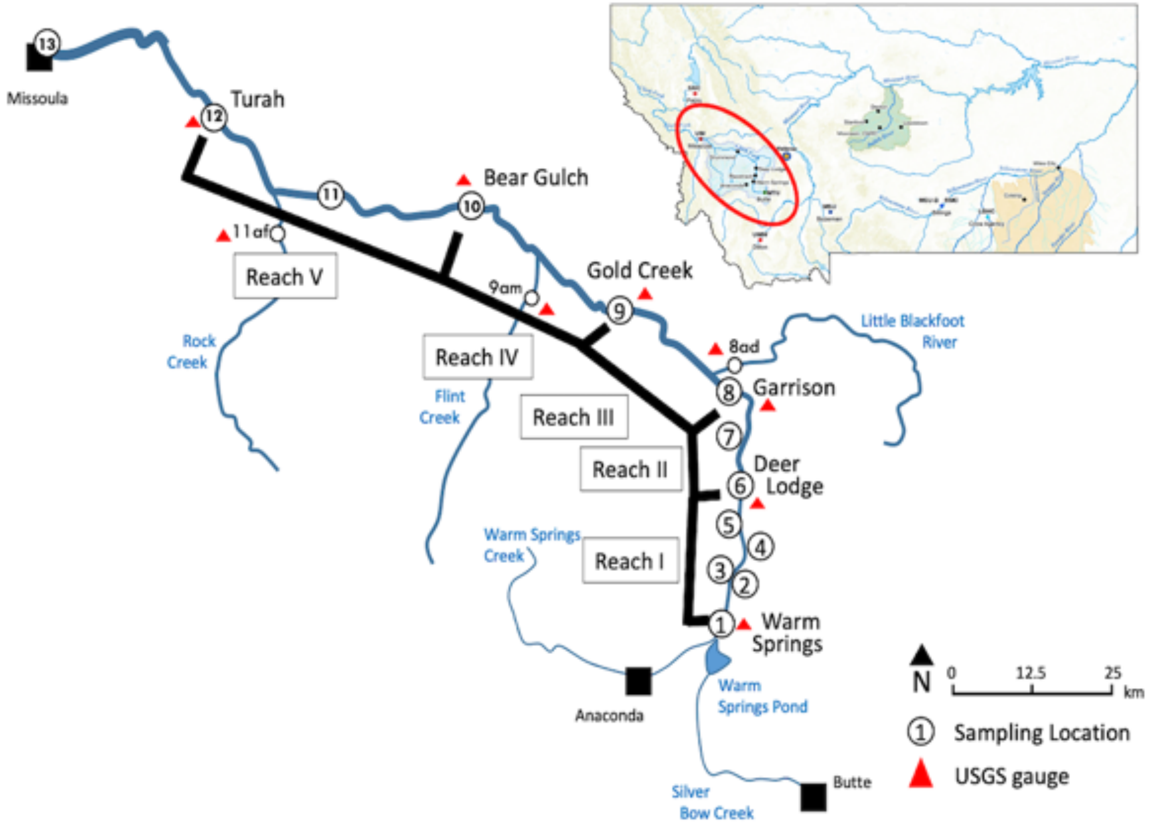

Figure 16. Descriptive map of the UCFR. Sampling sites are indicated by numbers and USGS gaging stations are depicted by red triangles. Smaller circles with alphanumeric designations indicate tributaries. Reaches I-V are defined by USGS gage station locations.

Table 5. Sample site locations with corresponding sample site number, distance downstream from Warm Springs, altitude, and the latitude and longitude where samples are taken. Reaches are designated by roman numerals to the left of the sampling location names. A sampling site with two reach designations indicates that it is the end member for the previous reach and start member for the following reach

Reach	Site Name	Site Number	Downstream Distance (km)	Elevation (m)	Latitude	Longitude
I	Warm Springs*	001	0.0	1459	46.1874	-112.7707
I	Perkins	002	5.1	1449	46.2083	-112.7674
I	Galen	003	12.2	1436	46.2372	-112.7532
I	Racetrack	004	19.3	1426	46.2651	-112.7446
I	Sager	005	30.9	1401	46.3172	-112.7362
I, II	Deer Lodge*	006	44.9	1378	46.3831	-112.7380
II	Cattle Rd	007	60.5	1350	46.4729	-112.7279
II, III	Garrison*	008	64.8	1340	46.4984	-112.7388
III	Little Blackfoot*, t	008ad	73.6	1333	46.5187	-112.7923
III, IV	Gold Creek*	009	89.2	1276	46.5900	-112.9282
IV	Flint Creek*, t	009am	124.4	1227	46.6289	-113.1514
IV, V	Bear Gulch*	010	144.3	1155	46.7037	-113.3455
V	Bonita	011	167.8	1102	46.7220	-113.5723
V	Rock Creek*, t	011af	182.1	1096	46.6977	-113.6692
V	Turah*	012	197.0	1013	46.8264	-113.8142
--	Missoula	013	215.8	968	46.8671	-113.9834

*Indicates sampling sites with USGS gage stations.

t Indicates tributary

Reaches and reach area

Five river segments (Reaches I-V, Figure 16) were identified and evaluated using the NPD approach. Reach length averaged 39 ± 16 km. The shortest reach (Reach II) was 19.9 km in length. Reaches were generally longer downstream as river discharge increased where the longest reach (Reach IV) was 55.1 km long. Reaches I and II have no major tributaries while Reaches III, IV, and V include confluences with the Little Blackfoot River (LBF), Flint Creek (FC), and Rock Creek (RC), respectively.

Reach wetted area (Aw, m^2) was calculated by averaging the upstream width and downstream width for each reach and multiplying by reach length. Stream width was estimated using nonlinear regression analyses derived from USGS gage specifications associated with historic discharge records across six locations (Figure 16) and from discrete width measurements (Valett et al. 2022). Lines of best fit were then established for each USGS gaged site and used to calculate upstream and downstream widths based on discharge during our sampling timeframes associated with each sampling event. The average percent error associated with this calculation across the six USGS gage stations was 1 ± 14%.

Dissolved organic carbon samples

DOC samples were collected in triplicate at each sampling location, filtered through a 0.7 µm Whatman glass fiber filter, and put into amber borosilicate 40-mL vials. Samples were collected between the hours of 0800 and 1700 starting at Warm Springs and working downstream to Missoula (Figure 16). Additionally, ashed Teflon disks were added to vial caps to minimize DOC contamination. Whatman glass fiber filters were combusted at 500°C for one hour and glassware were combusted for 4-hrs at 425°C prior to sample collection. Samples were refrigerated at 4°C until analyzed using an Aurora 1030W Total Organic Carbon Analyzer (Xylem Inc., Rye Brook, NY). The instrument employs heated persulfate wet chemical oxidation coupled to a non-dispersive infrared (NDIR) detector (U.S. EPA, 2005). Each day the instrument is used, it is calibrated using a six-point calibration ranging from 42 µmol Carbon L^{-1} (hereafter referred to as µmol L^{-1}) to 1665 µmol L^{-1}. Potassium hydrogen phthalate (KHP) standards (Fisher Scientific, Catalog #P243-100) were used for calibration and to test the accuracy and precision of the instrument after calibration. Based on several measurements of 416, 583, and 1249 µmol L^{-1} KHP standards, the instrument showed good agreement with an average error of 7 ± 31 µmol L^{-1} ($n = 32$). The precision of the triplicate field samples averaged 8.5 ± 14.8 µmol L^{-}

^{1}. Field blanks of DOC (i.e., deionized water filtered in the field) were also collected and analyzed to assess sample contamination and averaged 9.8 ± 11.9 µmol L^{-1} ($n = 24$).

Several studies have provided evidence of diel patterns of DOC in freshwater systems that can range from <80 to ~300 µmol L^{-1} depending on the system (Kaplan and Bott, 1982; Spencer et al. 2008; Parker et al. 2010; Johnson, 2021; Oviedo-Vargas et al. 2022). Therefore, sampling bias may exist for samples collected earlier in the day compared to samples collected in the evening. The low-resolution synoptic sampling approach (Dent and Grimm, 1999) used here indicates that a consistent DOC bias may exist due to diel variability in DOC. Importantly, DOC diel dynamics typically show increases in DOC during the day (e.g., Spencer et al. 2010; Johnson, 2021, Oviedo-Vargas et al. 2022) and would suggest that from Warm Springs to Missoula (Figure 16, Table 5), DOC would increase. Similarly, we know from preliminary findings that there is a distinct diel pattern in 350 nm absorbance (a commonly used proxy for DOC; Spencer et al. 2008) at Garrison (Figure 17, Table 5) (DeGrandpre et al. unpubl.) with increases in absorbance during the day. This supports the presence of DOC diel variability in the UCFR. However, below (see *Results*) we see a decrease of ~50 µmol L^{-1} between Warm Springs and Missoula. Note that this difference has the potential to be larger in the absence of DOC diel bias. Thus, diel DOC along the UCFR has the potential to be significant and could have biased our discrete sampling. However, the contrast between reported DOC diel behavior and our findings reported below indicates that spatial (and temporal) controls on DOC along the UCFR may overshadow diel variability, especially at coarse resolution (i.e., monthly, annually).

Temporal designation for seasonal analysis

For this study, seasons are defined by the months that best represent the seasonal progression in western Montana, USA. Western Montana is semi-arid with short autumnal duration, long winters, and a growing season that extends into late September. Therefore, seasons were defined accordingly: fall (October and November), winter (December through March), spring (April through June), and summer (July through September).

Statistical analyses

The primary statistical analyses used for this study were linear regression analysis, breakpoint regression analysis, Student's T-test ($\alpha = 0.05$), and analysis of variance (ANOVA). This suite of analyses allowed us to examine differences from zero and one as well as look at statistical variation among seasons for various measures. Additionally, the breakpoint regression analysis (e.g., Schmidt et al. 2010, Ulseth et al. 2019) provided this study with explanatory insight into distinct hydrologic regimes along the UCFR.

Results

Spatiotemporal variability

Periods of elevated DOC concentration (i.e., peaks of interest) along the UCFR were observed before, during, and after periods of increased discharge (Figure 17a; peaks 1-7). DOC concentrations ranged from 75 to 597 µmol L^{-1} ($n = 656$) along the main stem of the UCFR (Figure 17a) and exhibited annual oscillations with large peaks found in May-June (i.e., spring) of each year (peaks 1, 4, 7; Figure 17a). Compared to DOC concentrations at baseflow, spring peak concentrations were up to ~5 times greater depending on location. DOC was found to be strongly linked to discharge with greater DOC concentrations corresponding to increased discharge (Figure 17; R^2 from 0.32 to 0.74 for log-log regressions at gaged sites; Appendix C, Figure S1). In the UCFR, river-wide DOC averages (±SD) during the spring, summer, fall, and winter were 284 ± 95 µmol L^{-1} ($n = 195$), 193 ± 70 µmol L^{-1} ($n = 227$), 188 ± 55 µmol L^{-1} ($n = 91$), and 138 ± 58 µmol L^{-1} ($n = 143$), respectively. River-wide DOC concentrations among all

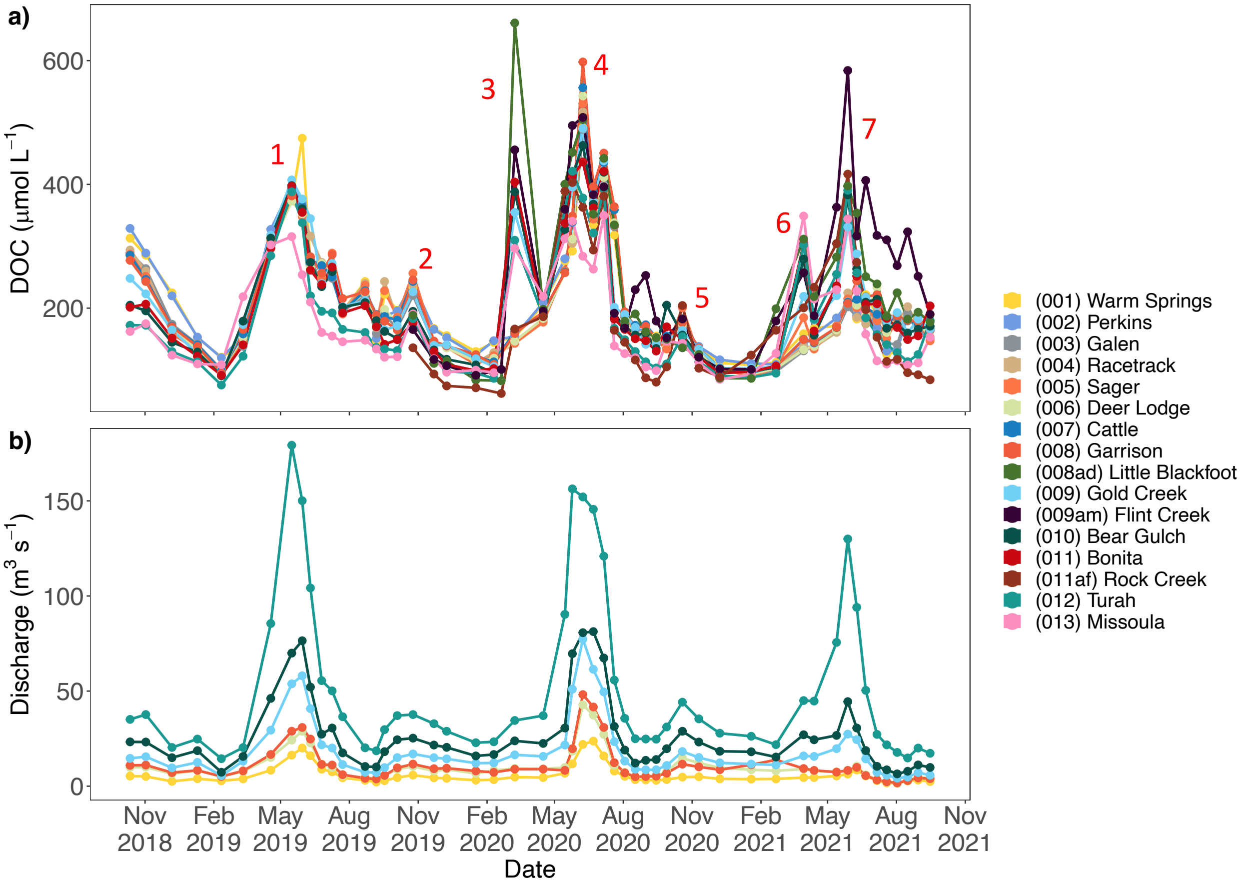

Figure 17. a) DOC time series (*n* = 656) at all sampling locations and times along the UCFR. Red numbers (1-7) denote DOC peaks of interest. **b)** Discharge time series at all six USGS gage stations along the main stem of the UCFR.

seasons were found to be statistically different ($p<0.001$). Only DOC values from fall and summer were not statistically different ($p>0.05$) due to small hydrologic influence during these times (i.e., baseflow; Figure 17). Additionally, grand means of DOC concentrations were found to be similar among water years (2019: 232 ± 82 µmol L^{-1}, n = 191; 2020: 223 ± 112 µmol L^{-1}, n = 247; 2021: 169 ± 55 µmol L^{-1}, n = 218).

Four of seven peaks (2, 3, 5, 6; Figure 17a) of increased DOC concentration occurred outside of annual snowmelt (i.e., peaks 1, 4, 7; Figure 17a). Two (2 and 5) occurred during fall whereas two others (3 and 6) took place during late winter just prior to snowmelt. The pre-snowmelt peaks in late winter (peaks 3, 6; Figure 17a) do not evidently correspond to distinct increases in discharge compared to peaks associated with maximum runoff (1, 4, 7) or periods of increased flow during fall following the cessation of summer baseflow (2, 5; Figure 17).

DOC concentrations differed less across space than over time (Figures 17 and 18). Site-wide average DOC concentrations for each water year differed by <50 µmol L^{-1} among sampling locations (Figure 18). The average percent change in DOC concentration from upstream (Warm

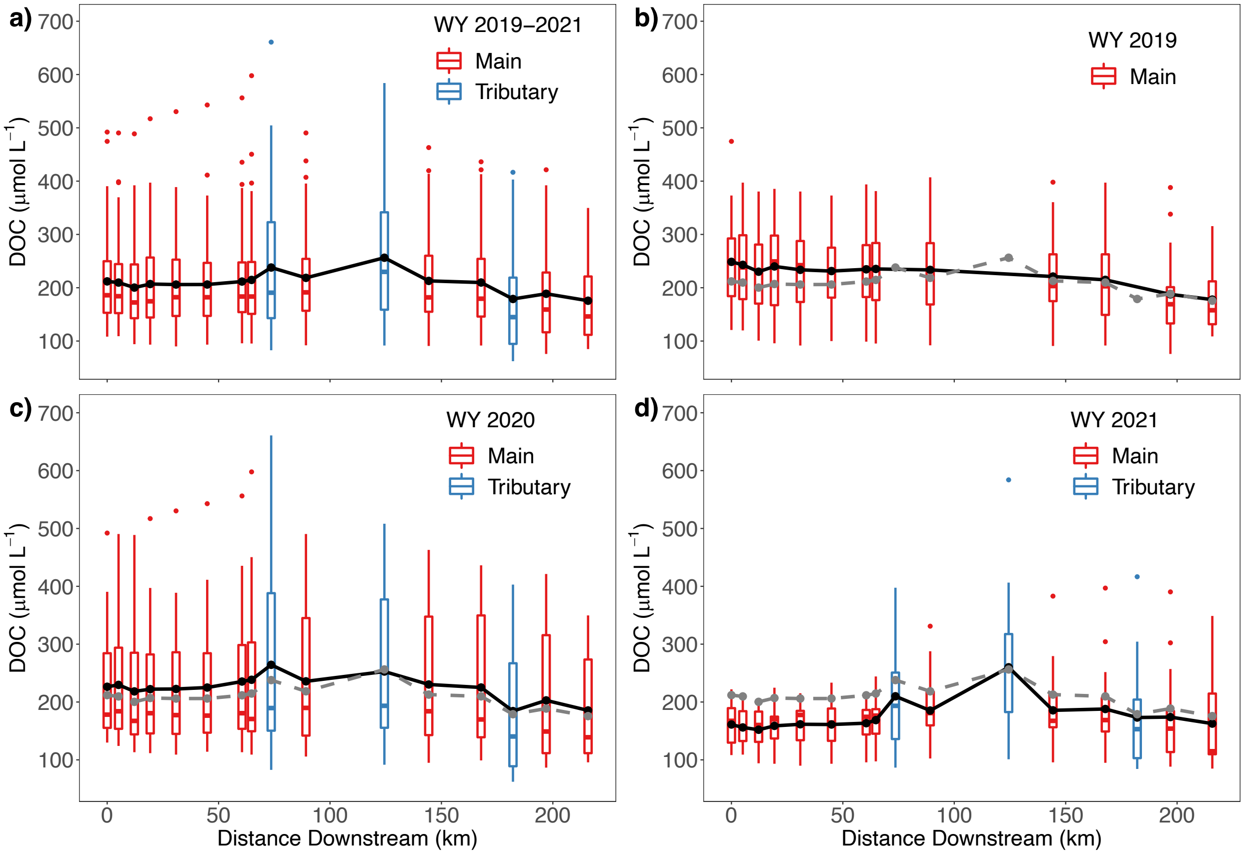

Figure 18. Spatial variability in DOC from upstream (Warm Springs = 0 km) to downstream (Missoula = 215.8 km) from **a)** WY 2019-2021, **b)** WY 2019, **c)** WY 2020, and **d)** WY 2021. Red boxplots indicate sampling sites on the main channel of the UCFR and blue boxplots denote tributaries. The black line in each subplot connects site-wide averages from upstream to downstream. The grey dashed line in subplots **b-c)** represents the spatial averages across all water years (black solid line in subplot **a)**.

Springs; Figure 16) to downstream (Missoula; Figure 16) was -15 ± 35% (*n* = 48) indicating lower DOC concentrations downstream. Additionally, spatial patterns in DOC concentration were consistent across water years 2019 and 2020 with grand means at each site differing by an average of only 4% (Figure 18). Water year 2021 had a grand mean much lower than the other water years ($p<0.001$) and differed from water years 2019 and 2020 by 21%.

Tributaries either enriched the main stem with DOC (i.e., higher DOC concentrations in LBF and FC; Figure 18) or diluted the main stem (i.e., lower DOC concentrations in RC; Figure 18). Average DOC concentrations during the study period for LBF, FC, and RC was 242 ± 137 µmol L^{-1} (*n* = 34), 260 ± 132 µmol L^{-1} (*n* = 33), and 185 ± 109 µmol L^{-1} (*n* = 33), respectively (Figures 17a and 18). Further, ranges of DOC were found to be 83 to 661 µmol L^{-1} (*n* = 34), 92 to 584 µmol L^{-1} (*n* = 34), and 62 to 417 µmol L^{-1} (*n* = 33) for the LBF, FC, and RC, respectively (Figure 18). Note that, like mainstem behavior, temporal variability in tributaries is driven with large DOC peaks associated with annual snowmelt (peaks 1, 4, 7; Figure 17a).

Reach characteristics and DOC processing domains

Relative concentration ($C_{dwn:up}$)

$C_{dwn:up}$ along the UCFR ranged from 0.5 to 2.2 due to the large seasonal fluctuations in DOC along the UCFR (Figure 17). This range indicates that the UCFR exhibits periods of depletion ($C_{dwn:up}<1$), chemostasis ($C_{dwn:up} = 1$), and enrichment ($C_{dwn:up}>1$) depending on season and reach (Figure 19). Most reaches show elevated $C_{dwn:up}$ values during late winter and spring when concentration (Figure 17a) and discharge (Figure 17b) also increase. Additionally, this shift in relative reach concentration from depleted to enriched back to depleted follows the nature of the hydrograph with $C_{dwn:up}>1$ during rising limbs and $C_{dwn:up}<1$ during the falling limb (Figures 17, 19 and Appendix C, Figure S2). On an annual basis only Reaches II and V display

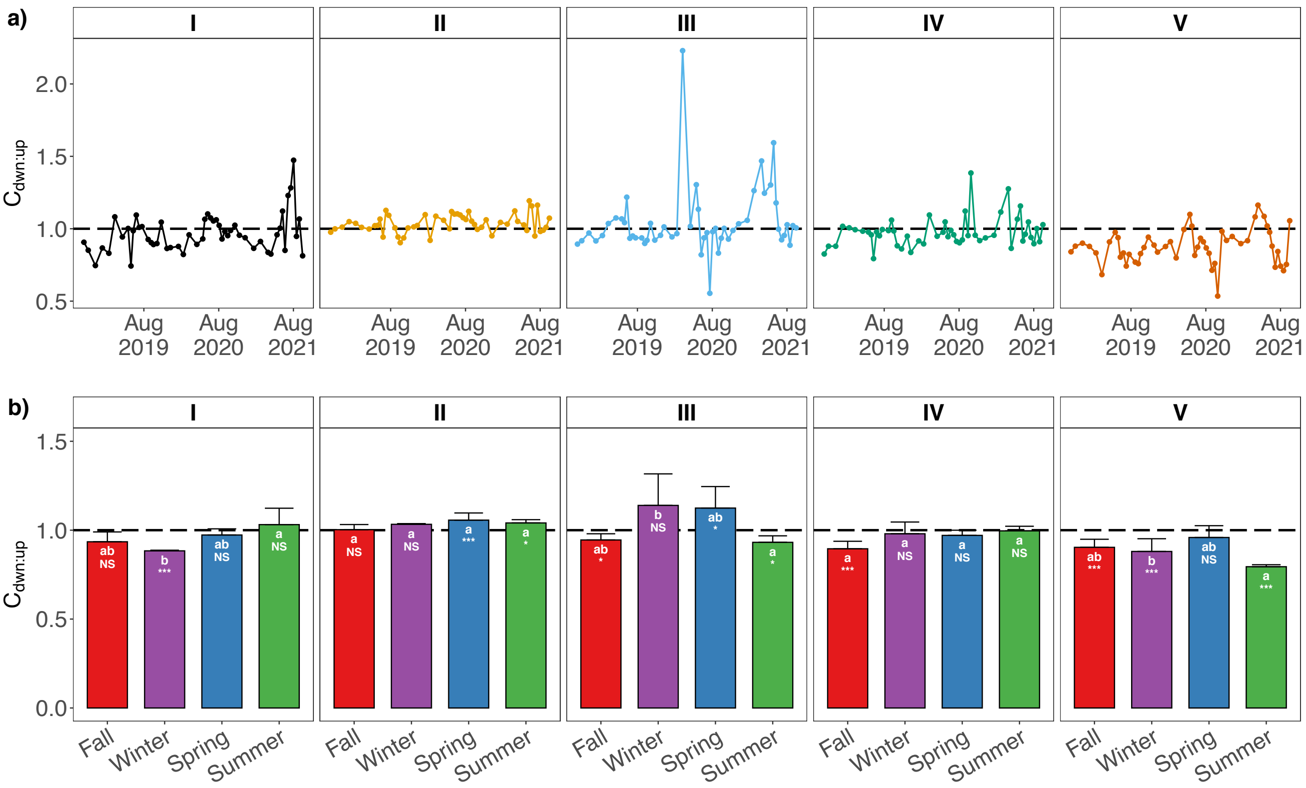

Figure 19. a) Spatiotemporal time series of $C_{dwn:up}$ for Reaches I-V. Individual lines and points are colored by Reach (data from Figure 17). **b)** Seasonal averages from 2018-2021 of $C_{dwn:up}$ for Reaches I-V. Error bars denote the standard deviation of averages from three water years. Unique letters designate statistical significance between bars within a reach (Tukey HSD following significant 1-way ANOVA). Asterisks denote individual bars are significantly different from 1 (NS, $p>0.5$; * $p<0.05$; ** $p<0.01$; *** $p<0.001$). Black dashed lines at 1 represent no change in the ratio of DOC from downstream to upstream.

availability effects statistically different from 1 ($p < 0.05$); Reach II was enriched in DOC ($C_{dwn:up} = 1.04$) and Reach V was depleted of DOC ($C_{dwn:up} = 0.87$) (Figure 19). In contrast, Reaches I, III, and IV display chemostatic behavior, with conserved DOC concentrations and $C_{dwn:up}$ not different from 1 ($p>0.05$). Reach III showed dramatic peaks in $C_{dwn:up}$ during each spring and winter (Figure 19) likely reflecting tributary influences. Support for this is provided by the elevated DOC concentrations evident in the LBF (tributary to Reach III) occurring during pre-snowmelt runoff (Figure 17). Seasonal dynamics in $C_{dwn:up}$ along the UCFR show that given reaches experienced periods of enrichment, chemostasis, and depletion statistically different from 1 (Figure 19b). Reaches I, III, and IV, where grand means indicated chemostatic behavior, exhibit significant periods of depletion or enrichment dependent on season (Figure 19b).

Hydrologic measures, exchange potential, and effective solute flux

ΔQ ranged from -3 to 109 $m^3 s^{-1}$ (*n* = 258) with an average of 9 ± 15 $m^3 s^{-1}$ (*n* = 258) (Figure 20a) and ΔHL ranged from -0.5 to 3.4 m d^{-1} (*n* = 258) with an average of 0.5 ± 0.6 m d^{-1} (*n* = 258) along the UCFR (Figure 20b). Only 25 out of 258 data points showed reaches with hydraulic loss (-ΔQ). Of the 25 data points, 23 points came from Reach II and 1 point came from Reach I and III. -ΔQ values occurred during all seasons but were more frequent during summer (48%). Spring snowmelt promotes hydraulic gain among reaches (Figure 20b) but that gain differs with the reaches position on the landscape and the influence of tributaries. Reach V experiences the greatest positive values for ΔQ while the range among the four other reaches are more similar. Normalizing to reach area illustrates that Reaches III and V behave similarly as do Reaches I and IV and that those two pairs differ in the magnitude of ΔHL but their patterns of change over the seasons are similar (Figure 20). In contrast, Reach II responds minimally to snowmelt and has several negative values distributed around the seasons (Figure 20).

The magnitude and direction of F_{eff} followed trends reported for ΔHL with greatest F_{eff} values during spring snowmelt (peaks 1, 4, 7; Figure 20c). Across all reaches and seasons, F_{eff} ranged from -0.2 to 1.4 mol $m^{-2} d^{-1}$ with an average of 0.13 ± 0.24 mol $m^{-2} d^{-1}$ (*n* = 251). Values for $F_{eff} < 0$ represents sinks for DOC and comprised only 8% (21 out of 251) of all measures (Figure 20). As expected from their similar and elevated values for ΔHL (Figure 19b), reaches III and V displayed comparable strong positive F_{eff} values in response to all periods of elevated flow (peaks 1-7; Figure 20c).

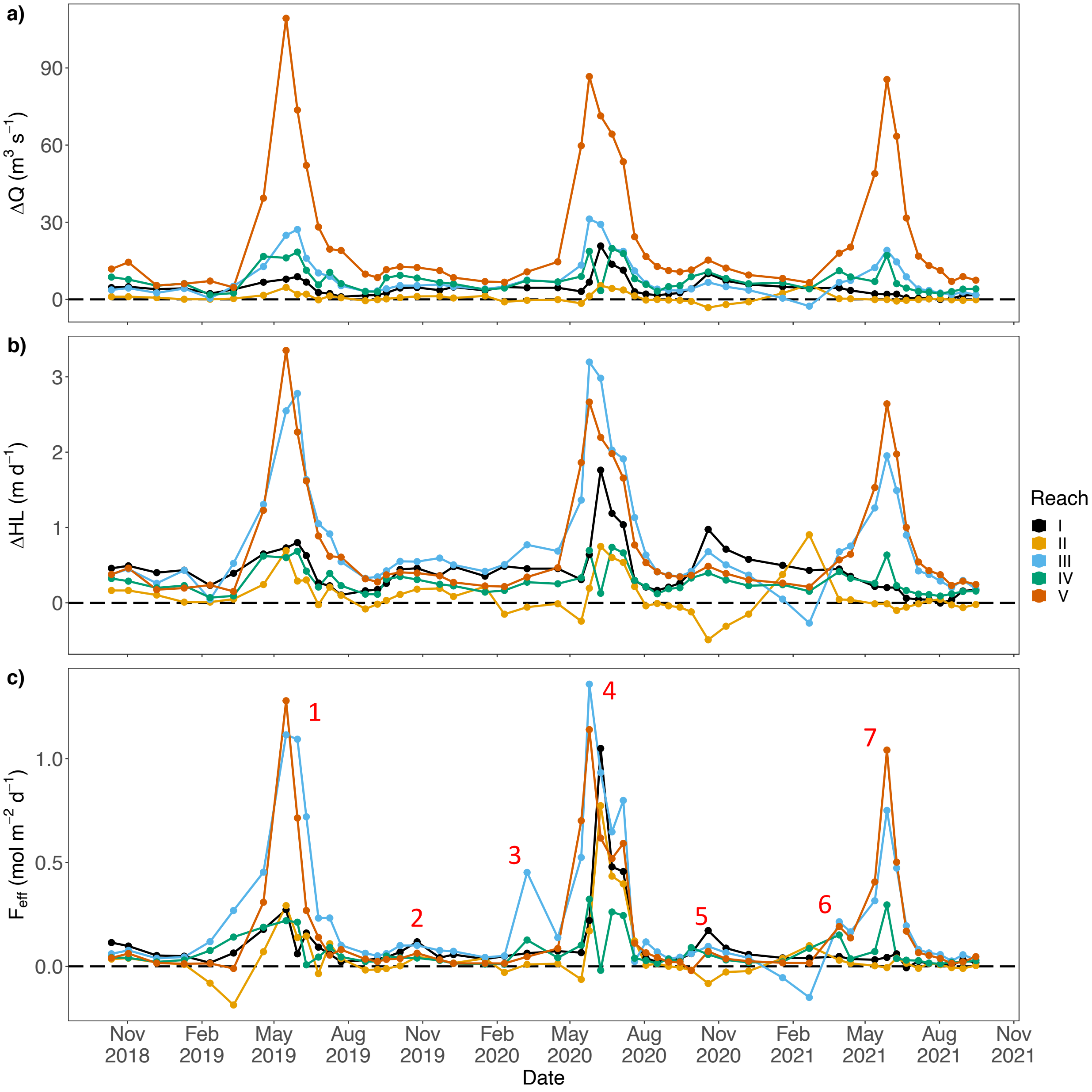

Figure 20. Spatiotemporal time series of **a)** ΔQ (*n* = 258), **b)** ΔHL (*n* = 258), and **c)** F_{eff} (*n* = 251). Individual lines and points are colored by reach (see Legend) as depicted in Figure 1 and Table 1. Black dashed lines at zero represent zero change **(a,b)** or flux **(c)**. Red numbers (1-7) on subplot **c)** represent the same peaks of interest described in Figure 18a to track spatiotemporal variability through the processing domain framework.

DOC processing domains

Reaches in the UCFR occupied CPDs reflecting the overwhelming influence of exchange potential and the generally non-reactive character of DOC. Increases in discharge generally resulted in increased loads and enhanced hydrologic exchange where more conservative behavior took place under baseflow conditions. Reaches along the UCFR were found to primarily occupy the diluter (40%), conduit (27%), or enhancer (24%) processing domains; enriched concentrations and increased loads associated with compilers were rarely observed (8%) as were conditions of declining load and decreased concentrations characteristic of consumer domains (1%) (Figure 21). All points within the consumer domain represented Reach II and correspond to negative changes in hydraulic loads (i.e., ΔHL<0; Figure 19b) indicating a losing reach (i.e., ΔQ<0; Figure 19a) and net export of DOC during spring 2019 and winter 2020.

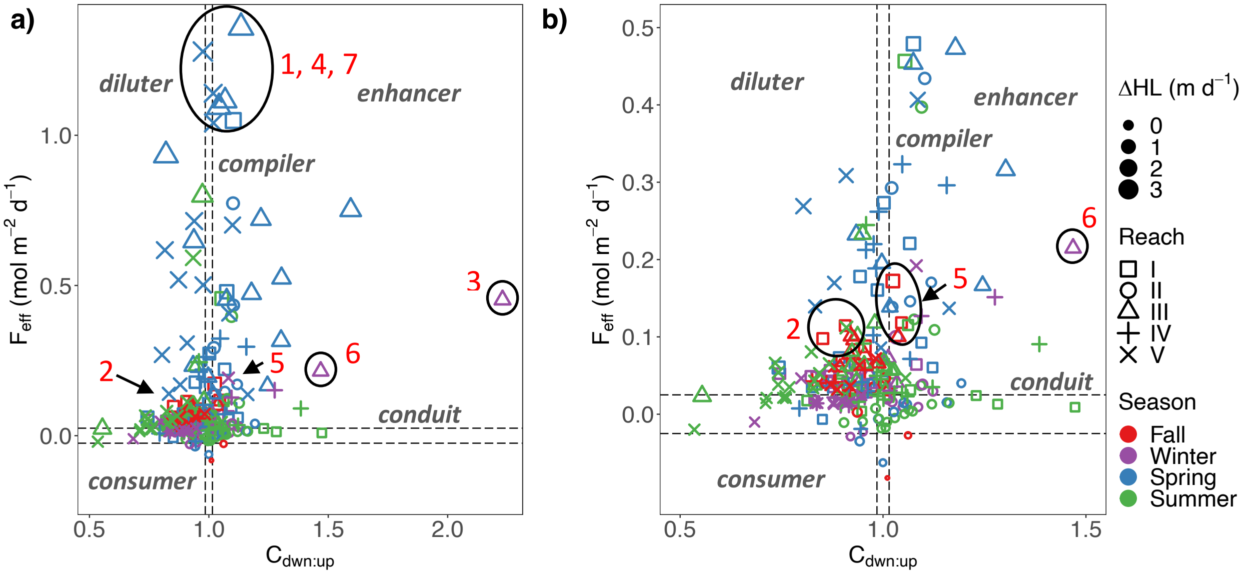

Figure 21. a) The carbon processing domains for five study reaches on UCFR. **b)** Detailed plot focusing on points with $F_{eff}<0.5$ mol m^{-2} d^{-1}. Note the change in scales of the x- and y-axes between **a)** and **b)**. Reaches are presented as unique symbols and each symbol is colored by season. Symbol sizes reflect the magnitude of the change in hydraulic load (ΔHL). Black dashed lines represent the 95% null boundaries for $F_{eff} = 0$ and $C_{dwn:up} = 1$. Points highlighted by black circles and red numbers (1-7) represent the peaks of interest presented in Figures 18a and 20c.

Snowmelt-driven increases in flow resulted in substantial hydrologic gains (i.e., strong positive ΔHL, Figure 20) and were accompanied by increases in DOC concentration (Figure 17) resulting in all but one peak of interest (i.e., peak 2) occupying the enhancer domain (Figure 21). Peak 2 occupied the diluter domain where increased flow increased material loads but decreased DOC concentration downstream (Figure 21). During the rising and falling limbs associated with peak flows, reaches transitioned across domains including diluter to enhancer during the rising limb and enhancer to diluter during the falling limb (Appendix C, Figure S2). This transition was reach dependent where, for example, Reaches I and II transitioned from the conduit to the enhancer domain during the rising limb.

Temporal patterns of CPD occupation for individual reaches were generally congruent (Appendix C, Figures S3-S5) as reflected in river-wide behavior. Greatest F_{eff} occurred during spring import (i.e., with +ΔHL). However, in response to spring runoff, reaches occupied diluter, conduit, compiler, and enhancer domains depending on reach location and water year (Appendix C, Figures S3, S4). In contrast, summer CPD assignment generally placed reaches in the conduit domain as reflected in low F_{eff} and little hydrologic exchange (i.e., small positive values for ΔHL) (Appendix C, Figure S4). Data points during the fall and winter primarily occupied the diluter domain with few points in the enhancer domain during pre-snowmelt runoff (i.e., +ΔHL) (Appendix C, Figure S4). The large F_{eff} values during the summer along the UCFR that occupy both the diluter and enhancer domains corresponds with the summer shoulder peak attached to peak 3 on Figure 17a.

Allochthonous inputs and biological processing

The important role for discharge in organizing the effective flux of DOC along the UCFR is illustrated by the robust linearity found between F_{eff} and ΔHL (Figure 22). Distribution of observations in the F_{eff}-ΔHL space, however, suggest two system states distinguished by the magnitude of flow accumulation. Within these states, points follow different linear trends; a steeper slope characterizes periods of greater flow accumulation which are themselves associated with greater river discharge (Figure 22). Breakpoint analysis indicates a point of inflection at ΔHL = 0.42 m d^{-1} ($p<0.05$), separating low-flow behavior (line 1; slope = 0.17 ± 0.02, $R^2 = 0.39$) from that of high-flow conditions (line 2; slope = 0.41 ± 0.02, $R^2 = 0.84$). Note that for line 2, spring (and a few summer) high flow events in reaches I, III, and V primarily contribute to the correlation. Low-flow phase space (line 1) includes a range of reaches and seasons that generally share relatively low absolute discharge (Q) and changes in hydraulic load (ΔHL). In contrast,

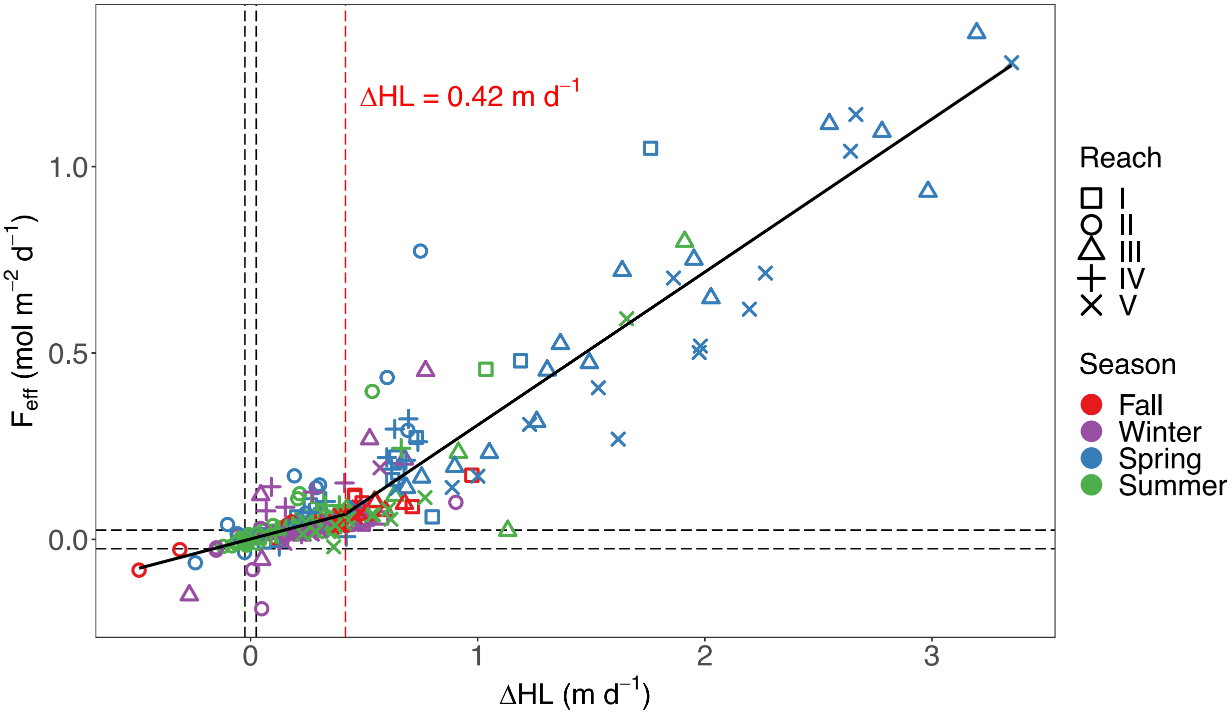

Figure 22. Effective solute flux for DOC (F_{eff}) versus change in hydraulic load (ΔHL) across seasons and reaches in the UCFR (*n* = 251). Reaches are represented by unique symbols colored by season. Black dashed lines represent limits for zero values. Solid black lines denote best fit regressions above and below the breakpoint value (ΔHL = 0.42 m d^{-1}, red dashed line) determined by breakpoint analysis.

high-flow phase space (line 2) reflects high flows during spring and summer that correspond with substantial flow accumulation along all reaches. These distinct phases of reach behavior reflect distinct combinations of import and processing that characterize contrasting realms of DOC dynamics.

Values derived from analysis of river-wide or individual reach responses across seasons and water years illustrate the contrasting measures of import concentration (C_{tg}) and biological processing (F_{bio}) during low-flow and high-flow phases (Figure 23). At the whole-river scale, C_{tg} and F_{bio} values during low flow (i.e., line 1) were 167 ± 16 μmol L^{-1} ($p < 0.001$) and -0.002 ± 0.004 mol m^{-2} d^{-1} ($p > 0.05$), respectively. During high flow (i.e., line 2), the values for C_{tg} were

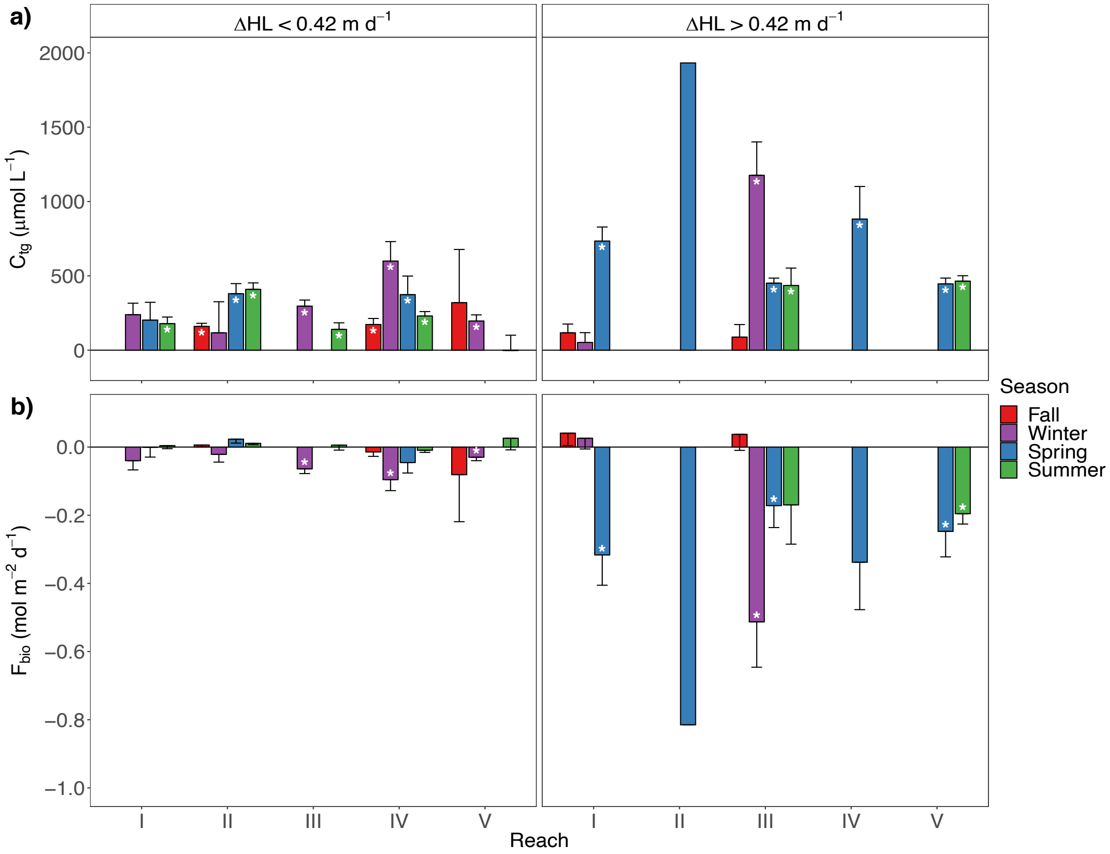

Figure 23. Estimates of **a)** allochthonous inputs (C_{tg}) and **b)** biological processing (F_{bio}) derived following equation 15 for individual reaches and seasons. Values are available in Table S1. Asterisks indicate values that are significantly different from zero ($p<0.05$).

greater (412 ± 19 µmol L^{-1}, $p < 0.001$) and the magnitude of F_{bio} more negative (-0.11 ± 0.02 mol m^{-2} d^{-1}) and significantly less than zero ($p < 0.001$). Results suggest lower import concentrations during periods of low flow accompanied by inconsequential rates of biological processing (i.e., F_{bio} not different from zero, $p>0.05$). In contrast, during high flow, C_{tg} was enriched more than 2-fold and accompanied by substantial biological processing (i.e., $F_{bio}<0$).

Analysis of individual reaches reveals the relative conservation of behavior during low-flow conditions compared to the highly dynamic changes in the character of import and processing during high flow (Figure 23). When $\Delta HL<0.42$ m d^{-1}, little variation was observed in C_{tg} across reaches and seasons; 69% of the reported values (140 to 600 µmol L^{-1}) were significantly different from zero ($p<0.05$). This suggests a consistent year-round source of allochthonous inputs along the UCFR and is supported by measured tributary DOC values in reaches III-V (Appendix C, Figure S6). Conversely, C_{tg} concentrations during high-flow phases across spring, summer, and winter ranged 3-fold from 435 to 1176 µmol L^{-1} with 64% of estimates significantly different from zero ($p<0.05$) (Figure 23 and Appendix C, Table S1).

Similar to C_{tg} concentrations, F_{bio} values show striking differences between low and high flow events. River-wide F_{bio} average was 50-fold greater during high flow compared to low flow, but an even more extreme contrast was observed among individual reaches and seasons (-0.0004 to -0.8 mol m^{-2} d^{-1}; Appendix C, Table S1). Only 25% of the reported values (-0.1 to 0.01 mol m^{-2} d^{-1}) were significantly different from zero ($p<0.05$) during low-flow conditions. In contrast, F_{bio} values during high-flow conditions ranged from -0.5 to -0.2 mol m^{-2} d^{-1} with 46% of the reported values significantly different from zero ($p<0.05$) nearly doubling the amount of significant F_{bio} values during low-flow conditions. Therefore, biological uptake of DOC along the UCFR is likely a relevant contributor to spatiotemporal variability of DOC during certain periods of peak discharge.

Discussion

Through the NPD approach, peaks of biogeochemical interest (i.e., peaks 1-7; Figures 17a, 19c, 21) were placed into functional processing domains along the UCFR to better interpret spatial and temporal trends in DOC. DOC concentrations along the UCFR were found to increase drastically during periods of increased discharge (i.e., spring snowmelt) compared to baseflow conditions. During spring, snowmelt saturates the floodplain and transports DOC-rich water to the river and effectively reconnects the floodplain to the river and increases discharge where small changes in ΔHL result in significant DOC loading to the river (Figure 22). This is a common characteristic of snowmelt dominated systems and has been shown extensively in the literature (Hood et al. 2006; Godsey et al. 2009; Dawson et al. 2011; Mast et al. 2016; Tunaley et al. 2016). The magnitude of DOC concentrations reported here also matches values found in other temperate rivers (Hood et al. 2006; Jeong et al. 2012; Cook et al. 2015).

The majority (~70%) of F_{eff} values were positive indicating a net loading of material (Figure 15) to the system. This suggests that the UCFR is transport limited where sufficient flow is needed (i.e., spring snowmelt) to transport DOC from the terrestrial landscape to the river (Tunaley et al. 2016; Valett et al. 2022). A source limited system, on the other hand, suggests a relatively small DOC source pool that flow events can deplete quickly (Tunaley et al. 2016; Shogren et al. 2021). The idea of transport limitation is further supported by elevated F_{eff} values arising during high flows in spring (Figure 21) where the floodplain is effectively reconnected to the river as discussed above. In previous studies, transport (or source) limitation is commonly assessed through log-transformed concentration-discharge plots (Godsey et al. 2009; Shogren et al. 2021). Using the NPD approach, similar conclusions can be made based on the sign of the effective solute flux (F_{eff}; Figure 15). There were, however, instances of $F_{eff} < 0$ (1% of data) in reach II that occupied the consumer domain (Figure 21) and suggests a sink of DOC indicative of source limitation during these times.

Increases in discharge along the UCFR correspond to elevated material loads ($+F_{eff}$) and changes in concentrations that placed reaches primarily into diluter and enhancer domains (Figure 21). Occupation of these domains indicates an overall source of DOC to the river ($+F_{eff}$), however, based on differences in reach scale hydrology the availability of DOC in the water column became depleted (i.e., diluter domain) or enriched (i.e., enhancer domain) (Figure 21; Appendix C, Figure S7). Additionally, reaches along the UCFR often occupied the conduit domain (27%) during low-flow conditions. This indicates that the UCFR shunts DOC loads downstream with minimal processing or changes during periods of low flow (i.e., summer and fall; Figure 21). In contrast, high-flow conditions illicit elevated F_{eff} values and a range of relative DOC concentrations ($C_{dwn:up}$) suggesting enhanced biogeochemical influences (i.e., allochthonous inputs, biological processing).

The quantitative relationship between F_{eff} and ΔHL (equation 16; Figure 22) assessed here provided critical insight into biogeochemical processes that influence DOC dynamics along the UCFR. Our results found statistically significant contributions from both allochthonous inputs (C_{tg}) and biological uptake of DOC (F_{bio}) (Figure 23) dependent on reach, season, and ΔHL (Figures 21, 22, 23). Additionally, F_{bio} values reported here (Appendix C, Table S1) are similar to respiration values reported in the literature (e.g., Bernhardt and Likens, 2002; Ensign and Doyle, 2006; Garnier and Billen, 2007; Dodds et al. 2017).

Based on breakpoint analysis (Figure 22) differences in ΔHL created two phase spaces: one at low-flow and the other at high-flow. This highlights a biogeochemical shift in how DOC is transported and processed along the UCFR and explains why reaches transitioned into diluter and enhancer domains during periods of high-flow (i.e., increased biogeochemical influence) but behaved conservatively during periods of low-flow (i.e., shunted downstream; Raymond et al. 2016) (Appendix C, Figure S2). Both C_{tg} and F_{bio} values significantly increased during high flows compared to low flows (Figure 23). Increases in both C_{tg} and F_{bio} suggests an inflow of exogenous source water with labile, terrestrially sourced DOC (Raymond et al. 2016; Tunaley et al. 2016; Bernal et al. 2019). Interestingly, the relationship between estimated C_{tg} and F_{bio} values were found to be negatively correlated where increases in estimated allochthonous inputs corresponded to larger rates of biological processing (Appendix C, Figure S8). Moreover, this correlation became stronger during periods of high flow (Appendix C, Figure S8) reiterating the idea that during high flow allochthonous inputs are supplying labile DOC to the UCFR which could be increasing instream biological production (i.e., more negative F_{bio}).

To assess estimates of C_{tg} a comparison was done between measured tributary DOC and C_{tg} estimates to better understand allochthonous inputs in reaches III-V, the reaches with major tributaries (Appendix C, Figure S6). Recall that C_{tg} is an estimate of all allochthonous inputs, not just tributary influence. Thus, any discrepancies between estimated C_{tg} and measured tributary surface water may be explained by other allochthonous inputs (i.e., groundwater, overland flow, etc.). Overall, we found that tributaries are likely the major source of allochthonous inputs (Appendix C, Figure S6). Estimated C_{tg} matched reasonably well with measured tributary DOC values during low flow but consistently overestimated measured tributary DOC values during high flows in winter, spring, and summer (Appendix C, Figure S6). The overestimation during high flows could largely stem from error associated with the C_{tg} estimate as well as other sources that are not accounted for including smaller tributaries, groundwater, etc. Thus, these other sources may help explain the observed deviation of up to ~800 μmol L^{-1} (Appendix C, Figure S6). Further, a recent study from Kyro (2021) indicates that measured groundwater DOC near the headwaters of the UCFR ranged from 25 to 3350 μmol L^{-1}. Note that reaches I and II do not have large tributaries and so groundwater may significantly contribute to C_{tg} values in these reaches (Figure 23 and Appendix C, Table S1). Thus, the reported values from Kyro (2021) provide a potential source for the relatively large, significant C_{tg} values estimated for these reaches (Appendix C, Table S1).

The CPD approach provided critical insight into the spatiotemporal dynamics of DOC along the UCFR for a variety of biogeochemical processes. Although ΔHL primarily controlled DOC dynamics (Figures 21 and 22), biogeochemical processes related to dilution, enhancement, and biological processing of DOC did not operate independently. This is apparent in Figures 21-23 where elevated values of F_{eff}, C_{tg}, and F_{bio} are reported during periods of high flow. Thus, even when F_{bio} is significant (Figure 23 and Appendix C, Table S1), F_{eff} will often be positive due to the magnitude of DOC loads in the UCFR. Only when concentration and/or discharge decreases enough will F_{bio} significantly impact F_{eff} and produce values in the consumer domain ($-F_{eff}$).

Conclusion

The processing domain provides a conceptual framework to systematically examine observed variability of aquatic solutes in time series plots that are by nature complex. The CPD uses a budgetary approach based on discharge, concentration, and reach wetted area to understand how river reaches process and transport solutes. This approach could be examined for metals, pollutants, and biogeochemically relevant solutes. The overall novelty of the processing domains conceptual framework is that it provides insights into the physical and chemical drivers (i.e., discharge, load, and concentration) as well as allochthonous inputs and biological activity of a system; all of which are important to fully understand the spatial and temporal variability of the processing of DOC in different river reaches. A caveat to using the CPD framework is that a lot of data and effort are needed to obtain the relevant measurements for this assessment. Additionally, the CPD framework should be integrated with independent measurements of F_{bio} (e.g., with in situ sensors or incubations) to validate the F_{bio} estimates shown in Figure 23.

A snowmelt dominated system such as the UCFR is a model system with repeatable annual and seasonal trends in precipitation and discharge. Because of this, monthly sampling was sufficient to capture DOC variability during the three water years of our study. In more hydrologically dynamic systems such as ones subject to intense short-term rain events (e.g., Spencer et al. 2008; Ågren et al. 2010; Abril et al. 2015; Mast et al. 2016), high resolution sampling may be needed to appropriately capture DOC variability as systems can vary widely in their response to precipitation events (Tunaley et al. 2016). This framework should prove robust enough to be applied to high frequency datasets to elucidate the variability of solutes on a diel, weekly, or monthly basis, providing added explanatory value to these highly dynamic systems.

This framework creates a path for a variety of future studies to assess its broad utility for any biogeochemically relevant solute or material (Appendix C, Figures S9, S10). For example, biomass standing stocks or chlorophyll *a* concentration could be tracked to understand how discharge may impact primary production signals. Additionally, this framework could be used at the regional level to functionally categorize different rivers, catchments, or regions as primarily diluters or enhancers, for example. Since the processing domain parameters are normalized by wetted area all streams and rivers would be able to be compared across landscapes and biomes, provided there are measurements of the processing domain parameters at this scale.

Chapter 5

Conclusions

The work presented in the preceding chapters outlined an effective method for calculating freshwater pCO_2 from pH and A_T (Chapter 2) and characterized the spatial and temporal variability of inorganic and organic carbon along the UCFR (Chapters 3, 4). The methodological advancement provided in Chapter 2 showed that spectrophotometric pH can significantly improve freshwater pH measurements compared to electrochemical pH. This improvement in pH resulted in a 4-fold reduction in calculated pCO_2 error compared to a reference measurement. To further show the utility of this approach, spectrophotometric pH and calculated pCO_2 were monitored for 4 water years along the UCFR described in Chapter 3 to estimate air-water CO_2 fluxes. Because this method was employed, and spectrophotometric pH provides more accurate calculated pCO_2 than electrochemical pH (Young et al. 2022), higher quality air-water CO_2 flux estimates were made. If the observed percent improvement in calculated pCO_2 from Chapter 2, corresponds to a similar improvement in estimated air-water CO_2 fluxes then the efflux of riverine systems could be reduced by ~40% (assuming calculated pCO_2 from electrochemical pH) from 1.8 Pg C yr^{-1} (Raymond et al. 2013) to 1.1 Pg C yr^{-1}, reducing its significance in the global carbon budget.

In addition to the novel methodological approach to calculating freshwater pCO_2, this research also displays the first ever account of using spectrophotometric pH for long-term (>1 yr) monitoring of freshwater pH. Lynch et al. (2010) also measured spectrophotometric pH, but this was at a single site in the UCFR and only lasted a year. In contrast, this study measured spectrophotometric pH along a ~200 km gradient of the UCFR for over 4 years. Additionally, the estimates of air-water CO_2 flux made along this ~200 km gradient of the UCFR (Chapter 3) are also a first where previous estimates were made at a single location in the UCFR (Lynch et al. 2010). We estimated riverine air-water CO_2 flux values as high as 1.2 mol m^{-2} d^{-1} (comparable to maximum reported values for larger rivers like the Amazon and Mekong Rivers; Liu and Han, 2021) and as low as -0.1 mol m^{-2} d^{-1} both at Gold Creek. As discussed above in Chapter 3, rivers are typically sources of CO_2 to the atmosphere. However, the productive nature of the UCFR, especially during summer, drove pCO_2 below atmospheric levels causing air-water CO_2 flux values to become negative and the UCFR to act as a sink for CO_2. The average estimates of air-water CO_2 flux were much less than those found in other temperate rivers (Chen et al. 2012; Hotchkiss et al. 2015; Duvert et al. 2018; Rocher-Ros et al. 2019). The river-wide average air-water CO_2 flux value of 0.08 mol m^{-2} d^{-1} presented in Chapter 3 is four times higher than the average air-water CO_2 flux presented in Lynch et al. (2010) of 0.02 mol m^{-2} d^{-1}. This difference in air-water CO_2 flux could be due to differences in the gas transfer velocities used in Lynch et al. (2010) since their reported pCO_2 values are similar to those we report along the UCFR. Note that averaging the air-water CO_2 flux of all sites along the UCFR minimizes the importance of episodic large flux estimates as shown in Chapter 3 (e.g., GC, Figure 12). Thus, monitoring riverine carbon dynamics along a longitudinal gradient (i.e., sampling several sites) is critical to better understand how the biogeochemical character may change along a river reaches to ultimately assess carbon processing, transport, and transformation.

As shown in Chapter 4, the CPD framework can be a valuable tool for quantitatively assessing DOC variability along river reaches. The utility of this approach stems from its ability to functional classify river reaches by hydraulic loading (ΔHL), solute fluxes (F_{eff}), and solute availability ($C_{dwn:up}$) (see Chapter 4, Figure 15). This functional classification can further decipher whether a reach acts a diluter, enhancer, consumer, compiler, and/or conduit based on reach values of F_{eff} and $C_{dwn:up}$ (see Chapter 4, Figure 21). These "domains" therefore describe the functionality of a reach. Importantly, reaches can occupy several domains and show a "domain progression" dependent on season, reach, and hydraulic load. We showcase reach III as an example of this domain progression in Appendix C (Figure S2) where reach III moves from the diluter domain to the enhancer domain at the onset of spring snowmelt (i.e., increased symbol size indicates increased hydraulic load). Once spring snowmelt ceases, reach III transitions back to the diluter domain by summer (Appendix C, Figure S2). Additionally, peaks of interest (see Chapter 4, Figure 17) were able to be tracked through the NPD framework to further explain observed spatiotemporal variability in DOC. Being able to track certain points of interest found in a timeseries to specific biogeochemical domains highlights the underlying utility of this approach. For example, a peak in DOC during the fall could be caused by several processes. These could include episodic rainfall (Mast et al. 2016), algal senescence (Jones et al. 2016), increased allochthonous DOC loading (Lynch et al. 2019), etc. From only looking at time-series and property-property correlations, it may be difficult to conclude which process has caused a peak in DOC during the fall. However, through the NPD approach, the calculated parameters (i.e., ΔHL, F_{bio}, C_{tg}) within, and the placement of those data in respective domains (i.e., consumer domain would suggest biological activity whereas diluter domain suggest hydraulic loading), you could conclude what process(es) likely controlled this peak.

The NPD approach could prove useful for both conservative (i.e., A_T, DIC) and nonconservative (i.e., pH, $p\mathrm{CO}_2$) inorganic carbon parameters in addition to other viable solutes (i.e., metals, pollutants, etc.). The only caveat being that a gas exchange term (i.e., F_{ex}) would need to be added to equations 15 and 16 (see Chapter 4). Right now, only biological processing (F_{bio}) and allochthonous inputs (C_{tg}) are accounted for in these equations as they were derived initially for nitrate and phosphate (Valett et al. 2022). A potential solution to this issue is to add the air-water CO_2 flux equation (Eq. 6) to equation 15. However, to get equation 6 to be relevant at the reach scale the difference between air-water CO_2 flux estimates at the downstream and upstream sites would need to be taken. Therefore, equation 15 would transform into equation 17 below.

$$\mathrm{F_{eff}} = \frac{\Delta \mathrm{Q} \times \mathrm{C_{tg}}}{\mathrm{A_w}} + \frac{\Delta \mathrm{L_{bio}}}{\mathrm{A_w}} + \Delta \mathrm{CO_{2Air-water}} \tag{17}$$

Where $\Delta CO_{2Air\text{-}water}$ is the change in air-water CO_2 flux (see equation 6; Chapter 3) from downstream to upstream. Once simplified, equation 16 would look like equation 18.

$$\mathrm{F_{eff}} = (\Delta \mathrm{HL} \times \mathrm{C_{tg}}) + (\mathrm{F_{bio}} + \mathrm{F_{ex}}) \tag{18}$$

Where F_{ex} is equivalent to $\Delta CO_{2Air\text{-}water}$ but formatted to match CPD notation. Note that F_{bio} and F_{ex} have the same units and so when solving for these variables through linear regression (see Chapter 4), the y-intercept value will be a combination of these two parameters (F_{bio} and F_{ex}). Thus, it is critical to have independent measurements of either F_{bio} or F_{ex} to be able to determine the relative contribution of each parameter to F_{eff}.

Summary

The aim of this research was to 1) be able to accurately characterize inorganic carbon and air-water CO_2 fluxes for freshwater systems and 2) be able to provide better interpretations of complex spatial and temporal patterns in DOC compared to previous approaches. In addition to each chapter satisfying these aims, this research also provides ideas regarding future research. This is important to note because more research is needed to further show the utility of the ideas discussed above. Our research only focuses on the UCFR, a productive, snowmelt dominated, mid-order river in a temperate biome. Thus, studies in other systems with different biogeochemical character will be needed to support and build off the methods, findings, and frameworks discussed here.

Future research needed to support and build from the information provided in Chapters 2-4 include laboratory experiments and field campaigns to test the approaches used here in diverse freshwater systems. The methodological approach for calculating freshwater $p\mathrm{CO_2}$ (Chapter 2) should be assessed at much higher levels of $p\mathrm{CO_2}$ (e.g., 2000-10000 µatm) as well as in systems with low A_T and high DOC to explore the utility of spectrophotometric pH in these systems. Additionally, using spectrophotometric pH to ultimately estimate air-water CO_2 fluxes (Chapter 3) should also be done in systems with higher levels of $p\mathrm{CO_2}$ to better understand the utility of spectrophotometric pH in a variety of freshwater systems. Lastly, the NPD approach created a path for a variety of studies to better interpret the spatiotemporal variability of biogeochemically relevant riverine solutes including conservative (e.g., A_T, DIC, metals, etc.) (Appendix C, Figures S9, S10) and nonconservative (e.g., pH, $p\mathrm{CO_2}$) (Appendix C, Figures S9, S10) parameters at local or regional scales.

Appendices

Appendix A

Supplemental Information for Chapter 2: Comparison of spectrophotometric and electrochemical pH measurements for calculating freshwater pCO_2

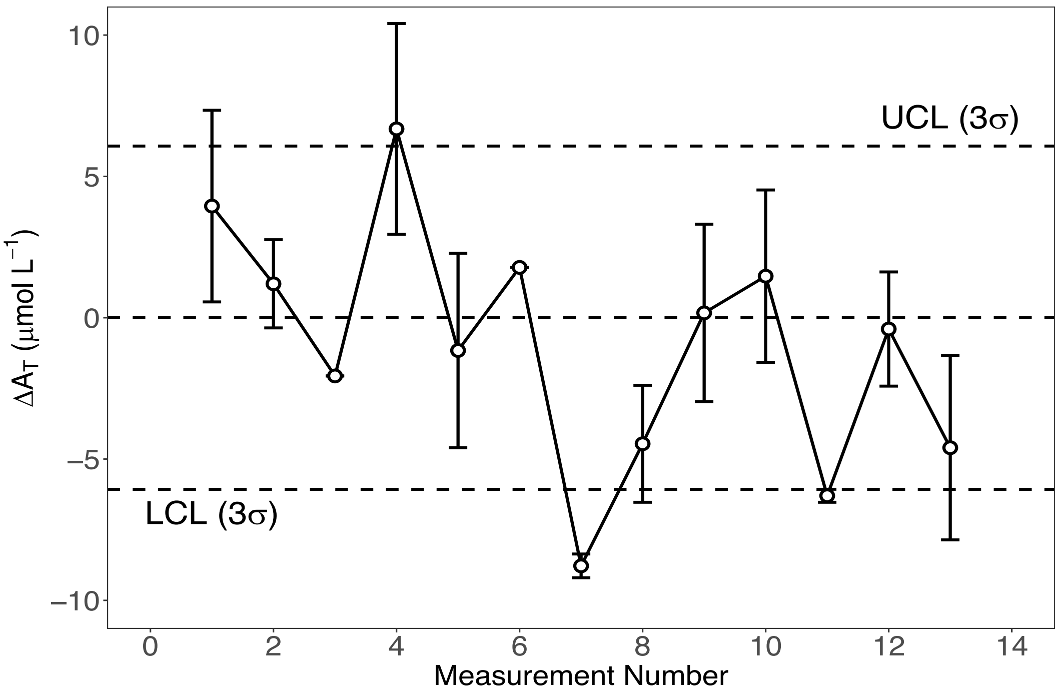

Figure S1. The A_T quality control chart representing the differences between known A_T standard values and measured A_T values. ΔA_T represents the average error between the known and measured A_T values (measured – known). The average ΔA_T is -1.0 ± 4.3 μmol L^{-1} ($n = 13$). The UCL and LCL represent the upper and lower 99% control limits, respectively, calculated from three times the average measurement standard deviation. Error bars represent the standard deviation of replicates. A total of 13 measurements were made covering the duration of the tank study experiment as outlined in the main text.

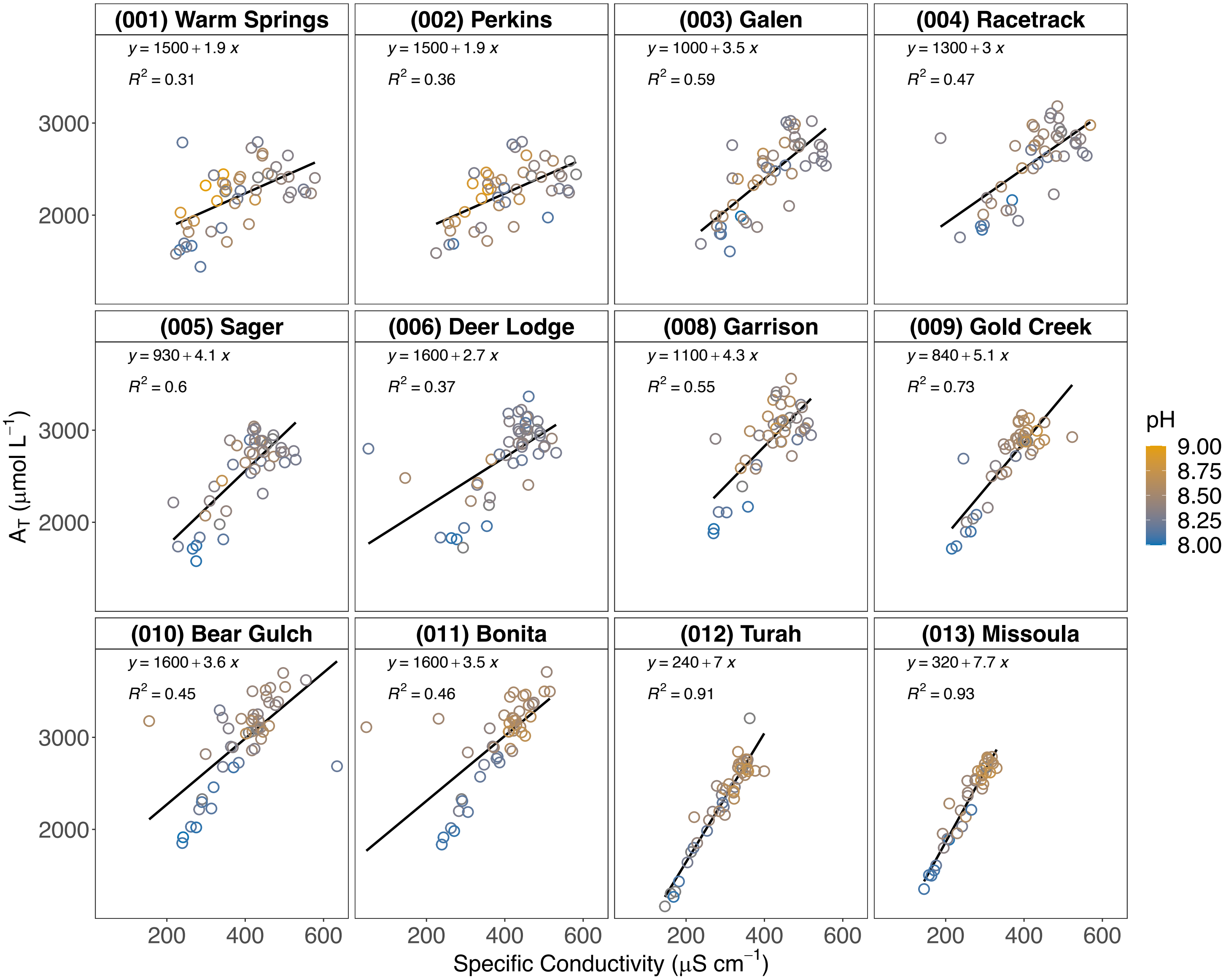

Figure S2. The relationship between total alkalinity (A_T) and specific conductivity at all main stem sampling locations along the upper Clark Fork River, MT, USA from September 2017 to September 2021. For a descriptive map of these locations refer to Chapter 4, Figure 16 of the main text. The line of best fit and the R^2 for each relationship is provided in the upper left of each subplot. Each data point is colored by pH collected at the same time and location as A_T and specific conductivity. For the entire time series record of A_T refer to Chapter 3, Figure 10.

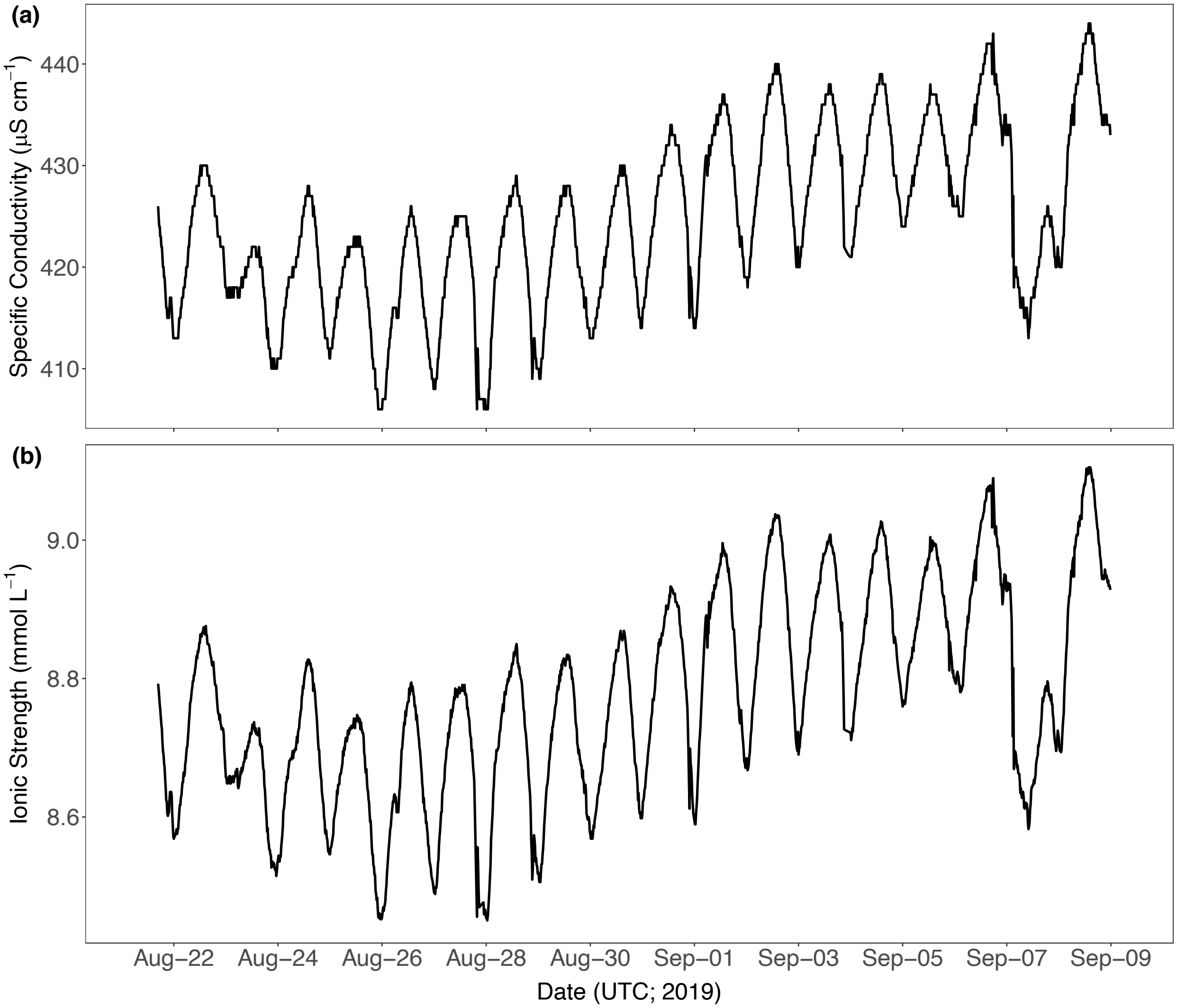

Figure S3. A 19-d time series from the CFR of **(a)** measured specific conductivity and **(b)** calculated ionic strength. Ionic strength was calculated using the conductivity-derived A_T obtained from Figure 1 in the main text along with eq. 5 (Nagorski 2020). The date and time are UTC during the year 2019.

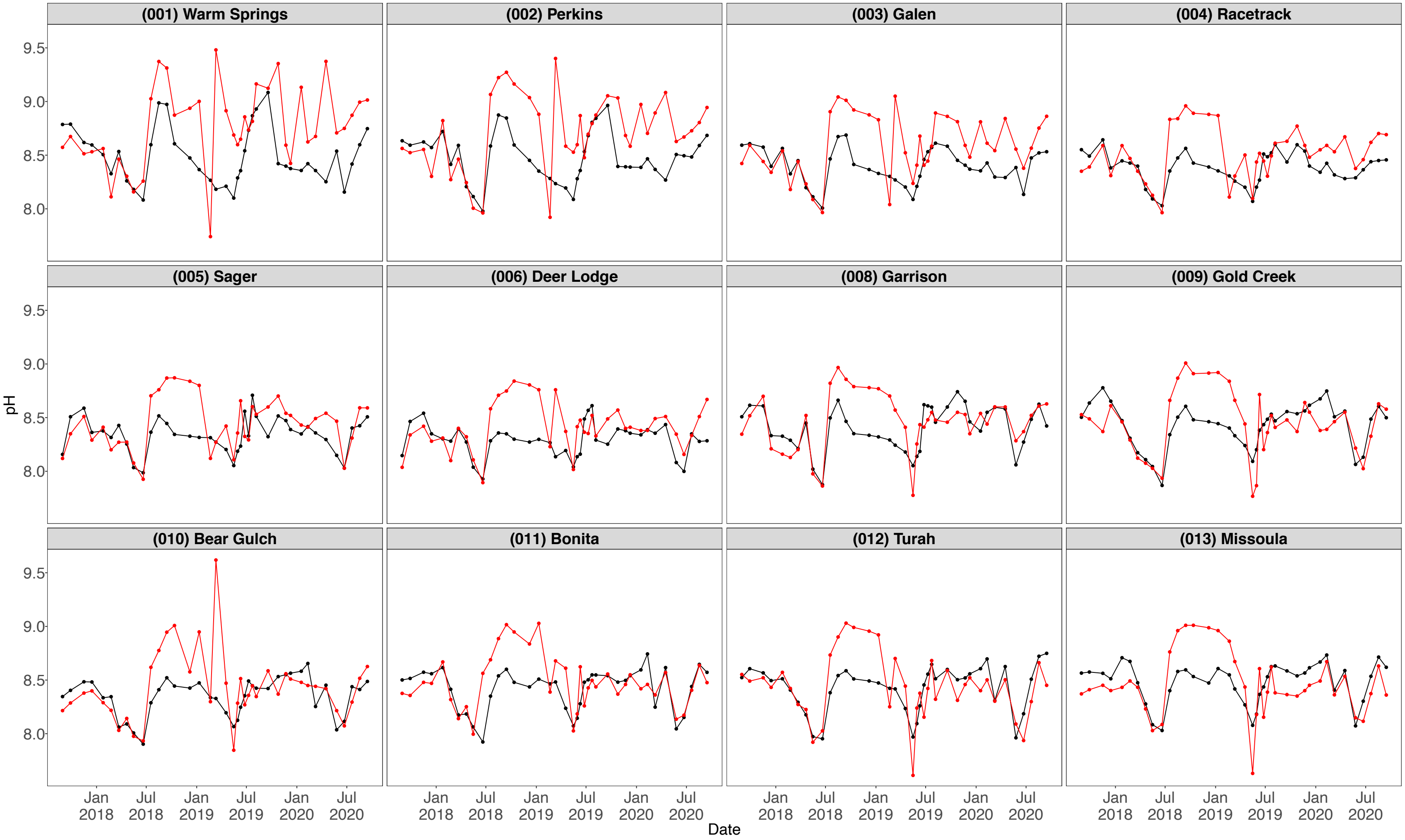

Figure S4. A time series record of discrete spectrophotometric pH (black line) and YSI electrochemical pH (red line) from September 2017 to September 2021 along the upper Clark Fork River, MT, USA. For a descriptive map of these locations refer to Chapter 4, Figure 16 of the main text.

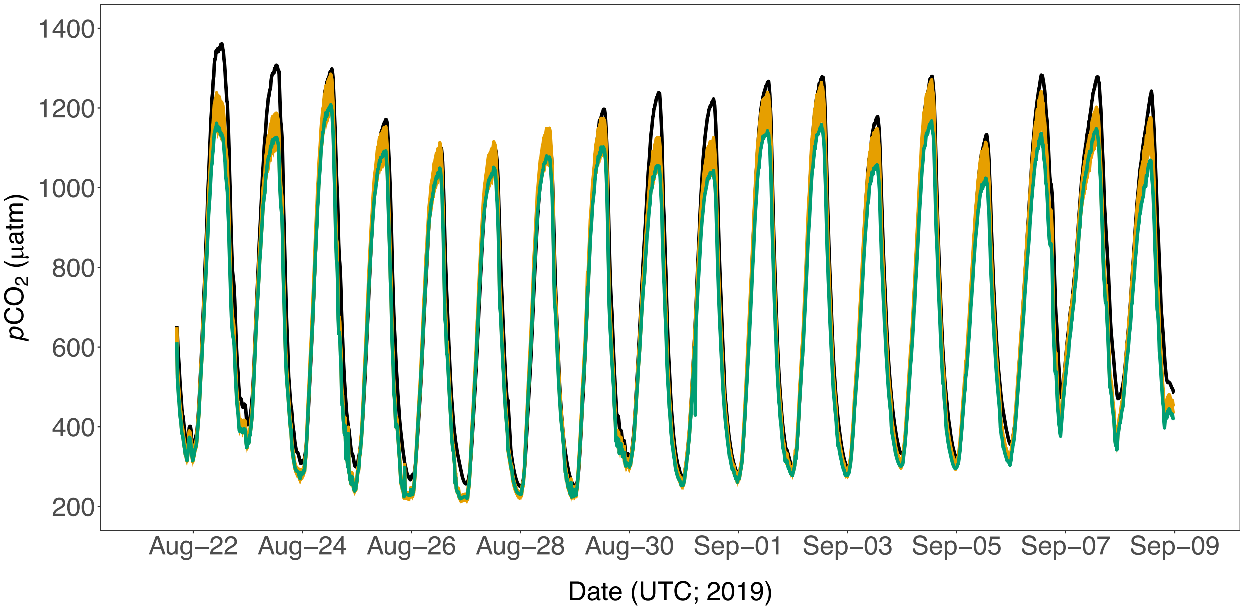

Figure S5. Measured (solid black line) pCO$_2$ time series compared to calculated pCO$_2$ using conductivity-derived A_T with ±130 µmol L^{-1} uncertainty limits (orange ribbon) and calculated pCO$_2$ using a constant A_T (3050 µmol L^{-1}) (green line). This plot examines the uncertainty in the conductivity derived A_T relationship and how it can help explain the observed difference between measured and calculated pCO$_2$ in Figure 6d of the main text.

Table S1. Example spectrophotometric $\mathrm{pH_{free}}$ measurements with molar absorptivity (ε), absorbances (A), and indicator concentrations used in the $\mathrm{pH_{free}}$ calculation (Eq. 1 of the main text). Samples 1 and 2 were measured at similar temperatures but different $p\mathrm{CO_2}$ levels (~100 and ~1600 μatm, respectively). Each molar absorptivity is distinguished by wavelength (434 or 578) and form of the indicator species (i.e., a = acidic form ($\mathrm{HI^-}$) and b = basic form ($\mathrm{I^{2-}}$)). The perturbation free pH was determined by the y-intercept of the regression between total indicator concentration and pH, as outlined in the main text.

Sample	Temp (ºC)	εa434 (L mol^{-1} cm^{-1})	εa578 (L mol^{-1} cm^{-1})	εb434 (L mol^{-1} cm^{-1})	εb578 (L mol^{-1} cm^{-1})	A434	A578	$\mathrm{HI^-}$ (M)	$\mathrm{I^{2-}}$ (M)	Total Indicator Concentration (M)	$p\mathrm{K_a}$	pH	Perturbation Free pH
1A	14.88	18000	103	2078	41845	0.0981	0.4917	4.06E-06	1.17E-05	1.58E-05	8.7612	9.0621	9.0641
1B	14.87	18000	103	2078	41846	0.1962	0.9857	8.19E-06	2.35E-05	3.17E-05	8.7613	9.0600	
1C	14.86	18001	103	2078	41847	0.2951	1.4740	1.23E-05	3.52E-05	4.75E-05	8.7614	9.0580	
2A	15.37	17984	103	2081	41790	0.2243	0.1417	1.21E-05	3.35E-06	1.54E-05	8.7561	8.0397	8.0413
2B	15.35	17984	103	2081	41792	0.4530	0.2847	2.44E-05	6.74E-06	3.11E-05	8.7563	8.0378	
2C	15.32	17985	103	2081	41796	0.6855	0.4293	3.69E-05	1.01E-05	4.70E-05	8.7566	8.0363	

Table S2. The average, standard deviation, and sample sizes for specific conductivity, total alkalinity (A_T), several ions used to calculate ionic strength (i.e., calcium, magnesium, chloride, and sulfate) (Eq. 4 of the main text), and the resulting estimated ionic strength during the duration of the tank study. Averages and standard deviations represent all treatments for the duration of the tank study experiment, as outlined in the main text. A counterion (Na^+) at a concentration of 0.07 mmol L^{-1} was used to achieve charge balance.

	Specific Conductivity (µS cm^{-1})	A_T (µmol L^{-1})	Calcium (mg L^{-1})	Magnesium (mg L^{-1})	Chloride (mg L^{-1})	Sulfate (mg L^{-1})	Ionic Strength (mmol L^{-1})
Average	334	2806	57	19	28	21	7.5
SD	54	395	8	3	4	3	1.1
n	35	34	35	35	35	35	35

Below is the code used in the main text for calculating freshwater *p*CO_2 from pH_{free}, A_T, temperature, and ionic strength. In the main text this program is referred to as “CalcCO2_frompH”. Commented throughout the code are references and descriptions for how to use the code.

```
% ****************pCO2_Equilibrium_Model_TA_pH_freshwater.M******************
% **********ORIGINALLY WRITTEN BY T.MARTZ FOR SEAWATER***************
% *******************MODIFIED FOR FRESHWATER BY C.LAI*******************
% ****************MODIFIED FOR READING DATASETS BY F. YOUNG************
% *******PROGRAM FOR CALCULATING pCO2 from pH and TA for freshwater********
% ******** Copyright 2022 - Martz, Lai, Young, and DeGrandpre.  MIT License ***********

%~~~~~~~~~~~~~~~~~~~~~~~~~~~~~~~~~~~~~~~~~~~~~~~~~~~~~~~~~~~~~~~~~~~~~~~~~~
%Brief Description of Program
%~~~~~~~~~~~~~~~~~~~~~~~~~~~~~~~~~~~~~~~~~~~~~~~~~~~~~~~~~~~~~~~~~~~~~~~~~~
% This program is used to calculate the partial pressure of carbon dioxide
% (pCO2) from pH and total alkalinity (TA). Ionic strength (I) is used for
% both the pH measurement and apparent equilibrium constants (K1a, K2a, KWa,
% and KHa). pH measurements are made on the Free Hydrogen Ion Scale and the
% hydrogen ion activity is determined using the Davies equation.

%~~~~~~~~~~~~~~~~~~~~~~~~~~~~~~~~~~~~~~~~~~~~~~~~~~~~~~~~~~~~~~~~~~~~~~~~~~
%Example of how to use Program
%~~~~~~~~~~~~~~~~~~~~~~~~~~~~~~~~~~~~~~~~~~~~~~~~~~~~~~~~~~~~~~~~~~~~~~~~~~
% Upload input parameters ('Temp','spCond' or 'IS, 'TA', and 'pH') as column
% vectors. Note: make sure that the units are correct as described below in
% 'INPUT VALUES'. Once input parameters are loaded and labeled properly, 'RUN'
% the script. The program will automatically generate the calculated pCO2
% under the column vector labeled 'pCO2_correction'. This will be the final
% pCO2 value. Note that this program also generates calculated values for
% dissolved inorganic carbon (DIC), bicarbonate ion (HCO3), carbonate ion (CO3),
% and dissolved CO2 (CO2).

%~~~~~~~~~~~~~~~~~~~~~~~~~~~~~~~~~~~~~~~~~~~~~~~~~~~~~~~~~~~~~~~~~~~~~~~~~~
% START SCRIPT
%~~~~~~~~~~~~~~~~~~~~~~~~~~~~~~~~~~~~~~~~~~~~~~~~~~~~~~~~~~~~~~~~~~~~~~~~~~

%~~~~~~~~~~~~~~~~~~~~~~~~~~~~~~~~~~~~~~~~~~~~~~~~~~~~~~~~~~~~~~~~~~~~~~~~~~
%Global Environment
%~~~~~~~~~~~~~~~~~~~~~~~~~~~~~~~~~~~~~~~~~~~~~~~~~~~~~~~~~~~~~~~~~~~~~~~~~~
global CT TA KWa K1a K2a KHa alpha1 alpha2

%~~~~~~~~~~~~~~~~~~~~~~~~~~~~~~~~~~~~~~~~~~~~~~~~~~~~~~~~~~~~~~~~~~~~~~~~~~
%Input Values
%~~~~~~~~~~~~~~~~~~~~~~~~~~~~~~~~~~~~~~~~~~~~~~~~~~~~~~~~~~~~~~~~~~~~~~~~~~
TC = Temp; %temperature in degrees celsius
```

```
TK = TC + 273.15; %temperature in Kelvin
EC = spCond ./ 1000; %electrical conductivity. EC must is in mS/cm so use uS/cm with the
%'./1000'
TA = TA ./ 1000000; %measured total alkalinity in mol/kg so make sure input TA is in umol/kg
pH = pH; %determined pH on the Free Hydrogen Ion Scale
I = 0.0127 .* EC; %ionic strength calculated from electrical conductivity in mol/L using Griffin
%and Jurinak 1973 relationship
%I = IS; %if ionic strength is known comment out 'EC' and 'I' calculation to use ionic strength
%estimates directly and uncomment this line.

%~~~~~~~~~~~~~~~~~~~~~~~~~~~~~~~~~~~~~~~~~~~~~~~~~~~~~~~~~~~~~~~~~~~~~~~~~~~~
%Calculating activity coefficients
%~~~~~~~~~~~~~~~~~~~~~~~~~~~~~~~~~~~~~~~~~~~~~~~~~~~~~~~~~~~~~~~~~~~~~~~~~~~~
%Calculations of concentrations for different ions are based on the equilibrium
%with the inclusion of activity coefficients and Davies equation
%~~~~~~~~~~~~~~~~~~~~~~~~~~~~~~~~~~~~~~~~~~~~~~~~~~~~~~~~~~~~~~~~~~~~~~~~~~~~
A = 0.5092 + (TC - 25) .* 0.00085; % temperature-related coefficient in Davies equation
gamma = -A.*(I .^ 0.5 ./ (1 + I .^ 0.5) - 0.3 .* I); % part of Davies equation
%~~~~~~~~~~~~~~~~~~~~~~~~~~~~~~~~~~~~~~~~~~~~~~~~~~~~~~~~~~~~~~~~~~~~~~~~~~~~
% Therefore, the activity coefficient to different ions are relevant to gamma*(charge of ion)^2
%~~~~~~~~~~~~~~~~~~~~~~~~~~~~~~~~~~~~~~~~~~~~~~~~~~~~~~~~~~~~~~~~~~~~~~~~~~~~
ACH = 10 .^ gamma; % activity coefficient for H+
ACOH = 10 .^ gamma; % activity coefficient for OH-
ACHCO3 = 10 .^ gamma; % activity coefficient for HCO3-
ACCO3 = 10 .^ (4 .* gamma); % activity coefficient for CO32-
%~~~~~~~~~~~~~~~~~~~~~~~~~~~~~~~~~~~~~~~~~~~~~~~~~~~~~~~~~~~~~~~~~~~~~~~~~~~~
%Calculating freshwater apparent equilibrium constants K1K2 (Source: Millero et al. 1979)
%~~~~~~~~~~~~~~~~~~~~~~~~~~~~~~~~~~~~~~~~~~~~~~~~~~~~~~~~~~~~~~~~~~~~~~~~~~~~
K1 = exp(290.9097 - 14554.21./TK - 45.0575.*log(TK));
K1a = K1 ./ (ACH .* ACHCO3); % apparent dissociation coefficient

K2 = exp(207.6548 - 11843.79./TK - 33.6485.*log(TK));
K2a = K2./(ACH .* ACCO3./ACHCO3); % apparent dissociation coefficient
%~~~~~~~~~~~~~~~~~~~~~~~~~~~~~~~~~~~~~~~~~~~~~~~~~~~~~~~~~~~~~~~~~~~~~~~~~~~~
%Calculating freshwater apparent equilibrium constants KW (Source: Millero 1995)
%~~~~~~~~~~~~~~~~~~~~~~~~~~~~~~~~~~~~~~~~~~~~~~~~~~~~~~~~~~~~~~~~~~~~~~~~~~~~
KW = exp(-13847.26 ./ TK + 148.9802 - 23.6521 .* log(TK));
KWa = KW./(ACH .* ACOH); % apparent dissociation coefficient
%~~~~~~~~~~~~~~~~~~~~~~~~~~~~~~~~~~~~~~~~~~~~~~~~~~~~~~~~~~~~~~~~~~~~~~~~~~~~
%Calculating freshwater apparent equilibrium constants KH (Source: Weiss 1974)
%~~~~~~~~~~~~~~~~~~~~~~~~~~~~~~~~~~~~~~~~~~~~~~~~~~~~~~~~~~~~~~~~~~~~~~~~~~~~
KH = exp(93.4517 .* 100 ./ TK - 60.2409 + 23.3585 .* log(TK ./ 100));

        % Convert ionic strength to salinity
                S = 53.974*I;
```

```
KHa = KH + (0.023517 - 0.023656 * TK./100 + 0.0047036 .* TK./100 .* TK./100).*S;
%~~~~~~~~~~~~~~~~~~~~~~~~~~~~~~~~~~~~~~~~~~~~~~~~~~~~~~~~~~~~~~~~~~~~~~~~~~~~~
%Calculation of each ion concentration
%~~~~~~~~~~~~~~~~~~~~~~~~~~~~~~~~~~~~~~~~~~~~~~~~~~~~~~~~~~~~~~~~~~~~~~~~~~~~~
   H = 10.^(-pH);
   OH = KWa ./ H;
   alpha1 = (H .* K1a)./(H.^2 + K1a .* H + K1a .* K2a);
   alpha2 = (K1a .* K2a) ./ (H.^2 + K1a .* H + K1a .* K2a);
   CT  = (TA- OH + H) ./ (alpha1 + 2.*alpha2);
   CO2 = CT .* (H .^ 2) ./ (H .^ 2 + K1a .* H + K1a .* K2a);
   HCO3 = CO2 .* K1a ./ H;
   CO3 = HCO3 .* K2a ./ H;
%~~~~~~~~~~~~~~~~~~~~~~~~~~~~~~~~~~~~~~~~~~~~~~~~~~~~~~~~~~~~~~~~~~~~~~~~~~~~~
%DIC calculation
%~~~~~~~~~~~~~~~~~~~~~~~~~~~~~~~~~~~~~~~~~~~~~~~~~~~~~~~~~~~~~~~~~~~~~~~~~~~~~
DIC = CT .* 1000000;
%~~~~~~~~~~~~~~~~~~~~~~~~~~~~~~~~~~~~~~~~~~~~~~~~~~~~~~~~~~~~~~~~~~~~~~~~~~~~~
%pCO2 calculation
%~~~~~~~~~~~~~~~~~~~~~~~~~~~~~~~~~~~~~~~~~~~~~~~~~~~~~~~~~~~~~~~~~~~~~~~~~~~~~
CO2 = (CT .* (H.^2) .* 10.^ (6.*gamma)) ./ ((H.^2 .* 10.^(6.*gamma))+ (K1 .* H .*
10.^(4.*gamma))+ (K1 .* K2));

  %Uses Henry's Law constant and converts from atm to uatm (KH in fugacity (mol-atm / kg-
  %soln))
   pCO2 = (CO2 ./ KH) .* 1000000;
  %Uses the apparent Henry's Law constant and converts from atm to uatm (KHa in fugacity
  %(mol-atm / kg-soln))
   pCO2_correction = (CO2 ./ KHa) .* 1000000;

%~~~~~~~~~~~~~~~~~~~~~~~~~~~~~~~~~~~~~~~~~~~~~~~~~~~~~~~~~~~~~~~~~~~~~~~~~~~~~
%END SCRIPT
%~~~~~~~~~~~~~~~~~~~~~~~~~~~~~~~~~~~~~~~~~~~~~~~~~~~~~~~~~~~~~~~~~~~~~~~~~~~~~
```

Appendix B

Supplemental Information for Chapter 3: The temporal and spatial regulation of air-water CO_2 fluxes along a montane river

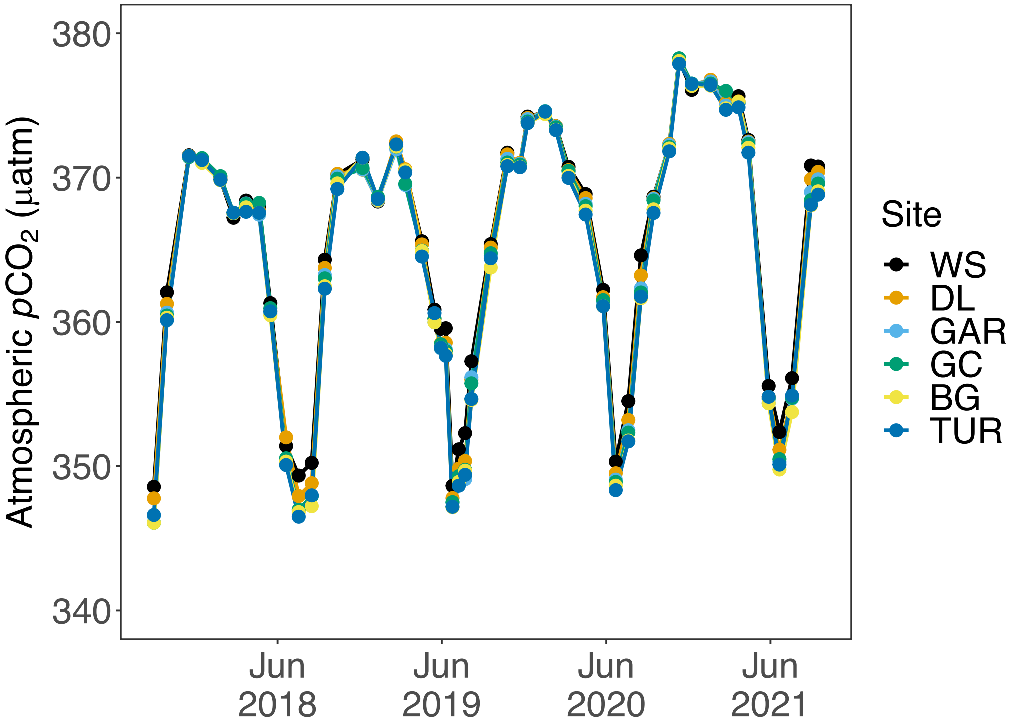

Figure S1. The timeseries of atmospheric pCO_2 obtained from a meteorological tall tower in Wisconsin, USA (Andrews et al. 2017). Points are colored by site and correspond to sites with USGS gaging stations (Figure 8, Table 4).

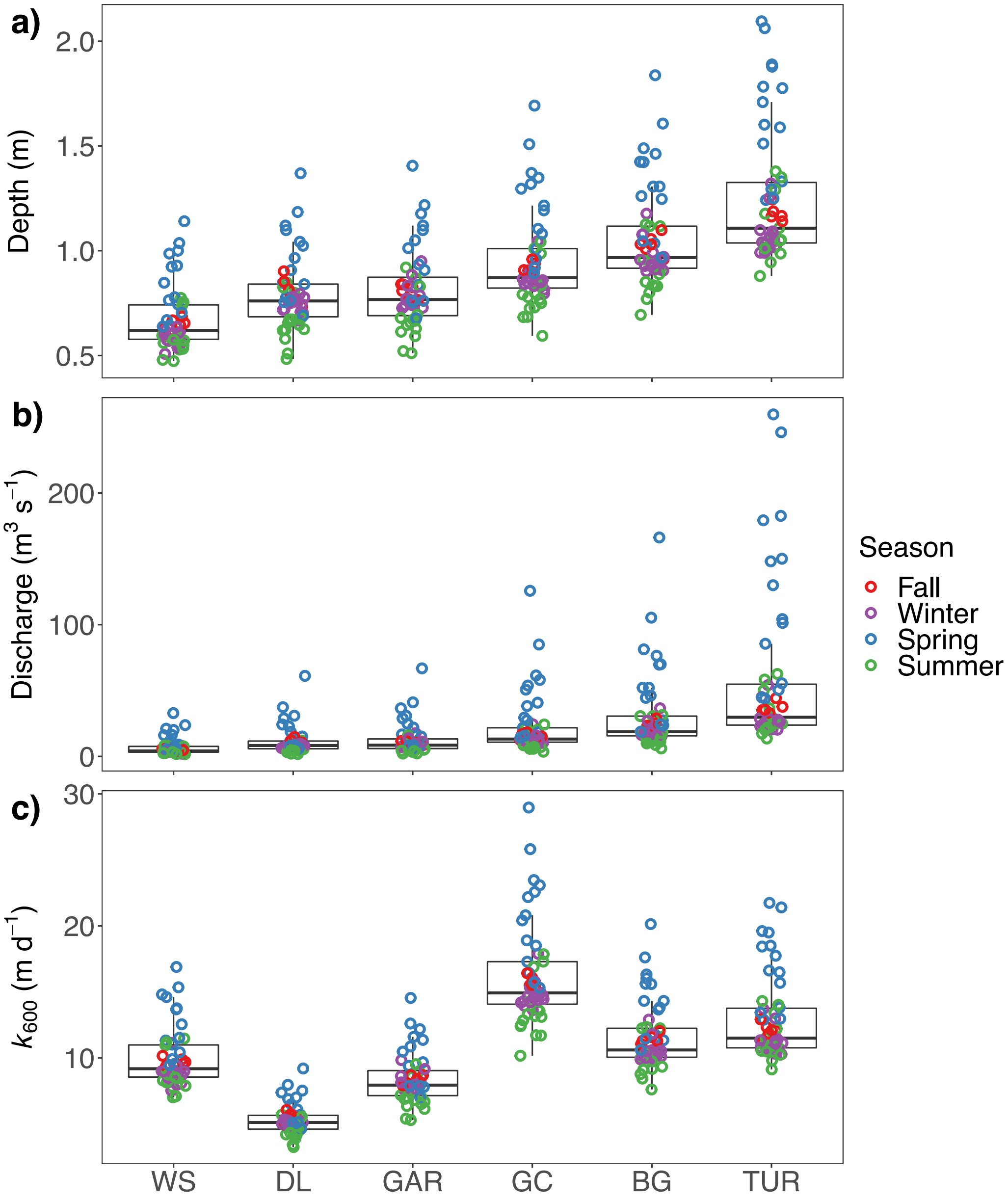

Figure S2. The **a)** depth, **b)** discharge, and **c)** k_{600} values for each sampling location used to calculate the CO_2 flux. k_{600} values were obtained through the Bayesian model, *StreamMetabolizer* in R. Individual data points are jittered on top of each boxplot and colored by season to display the variability of values.

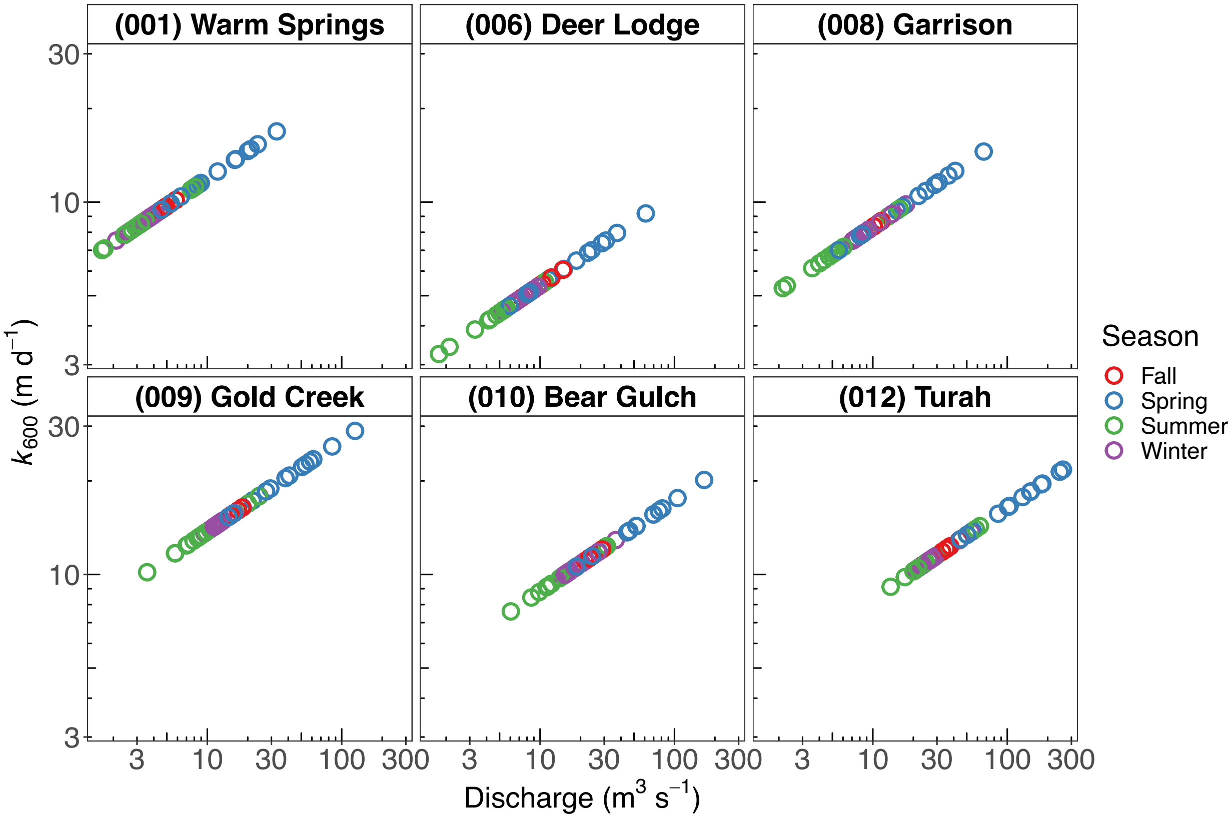

Figure S3. The relationship between estimates of k_{600} and discharge from the six USGS gage stations described in Figure 8 and Table 4. Both the x- and y-axis are log transformed and individual points are colored by season.

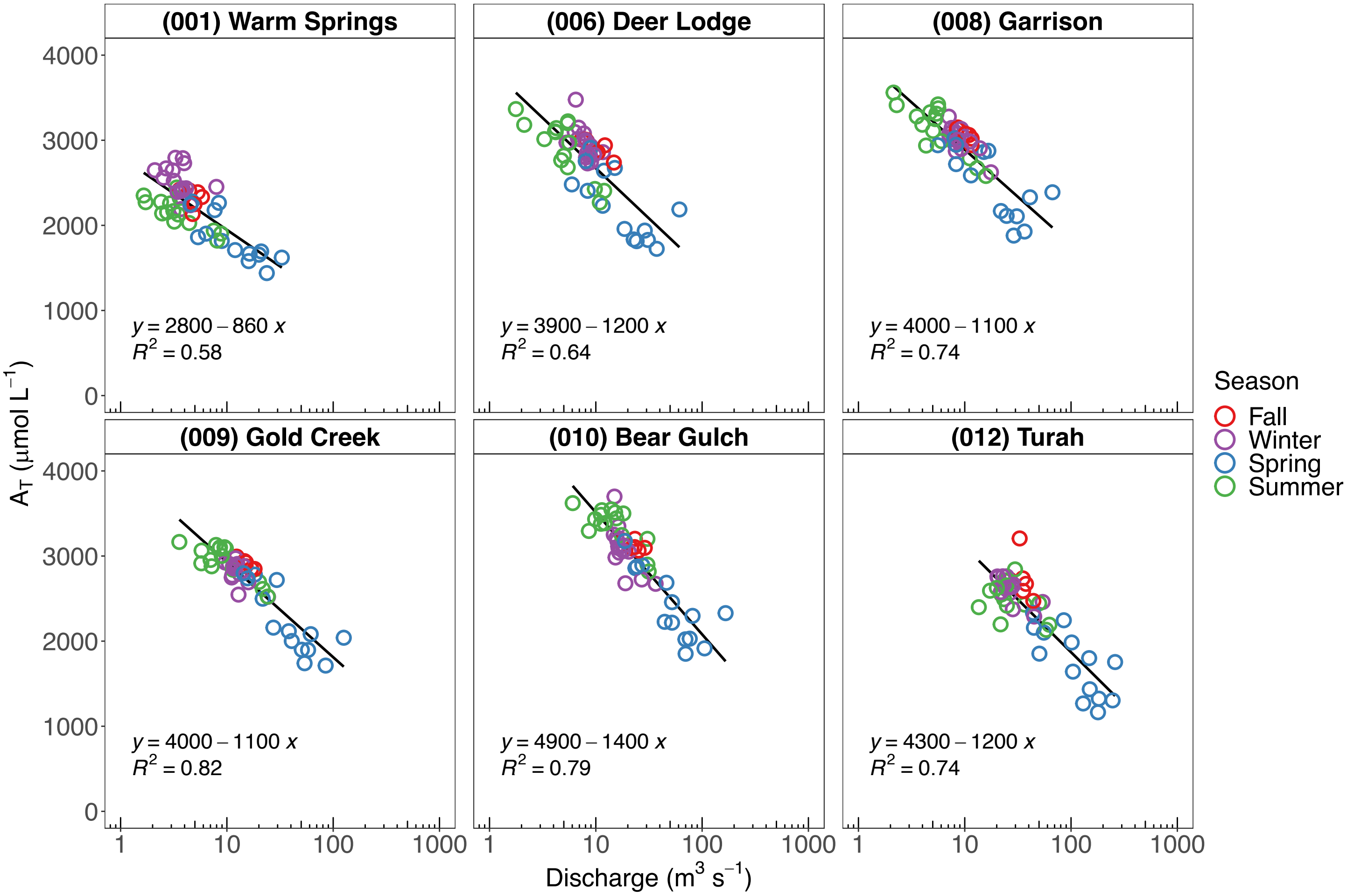

Figure S4. Log-concentration relationship of A_T as a function of discharge for each sampling site with a USGS gaging station. Individual points are colored by season and the coefficient of determination (R^2), and linear equation are presented in the bottom-left of each panel.

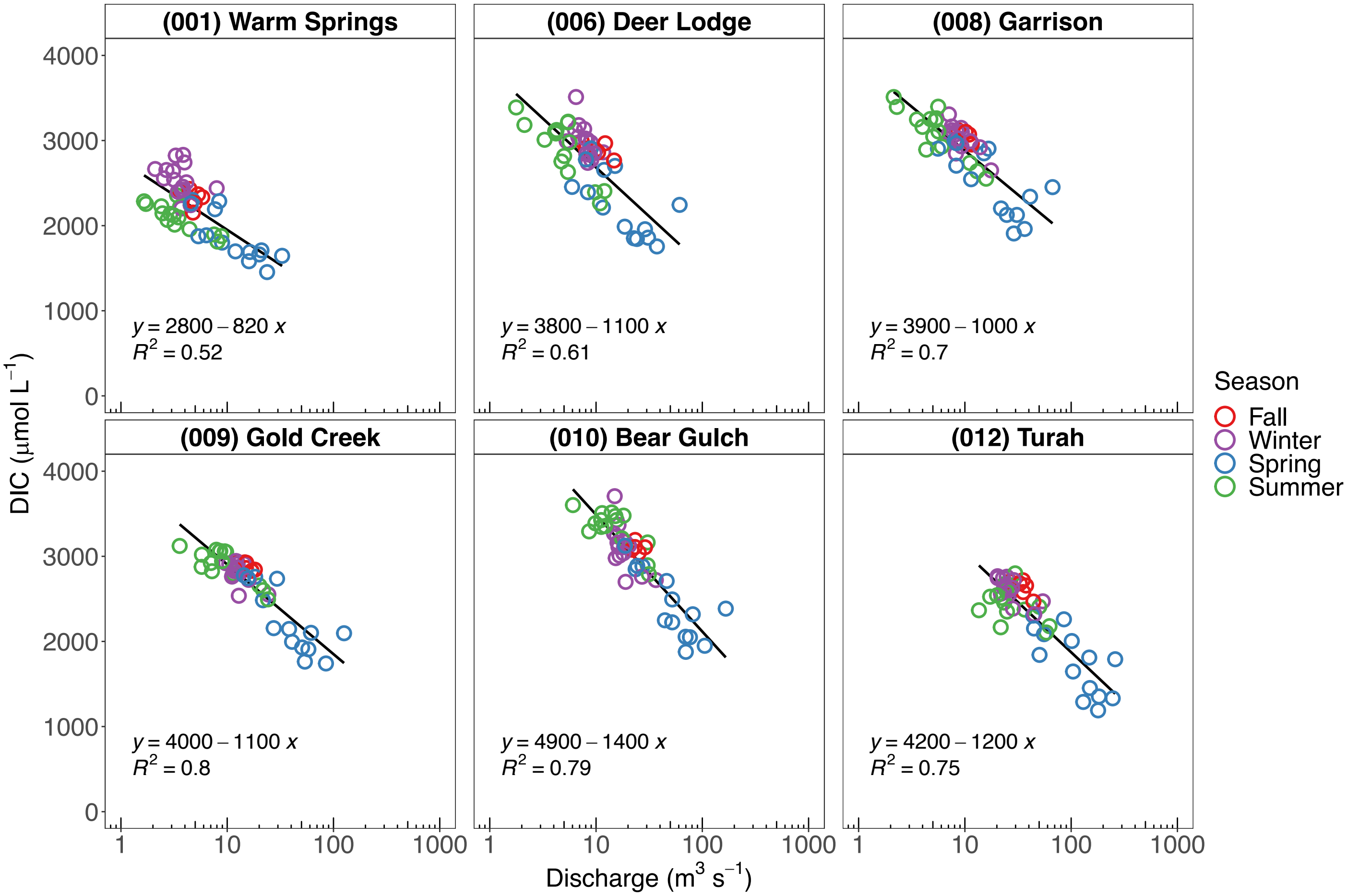

Figure S5. Log-log relationship of DIC as a function of discharge for each sampling site with a USGS gaging station. Individual points are colored by season and the coefficient of determination (R^2), and linear equation are presented in the bottom-left of each panel.

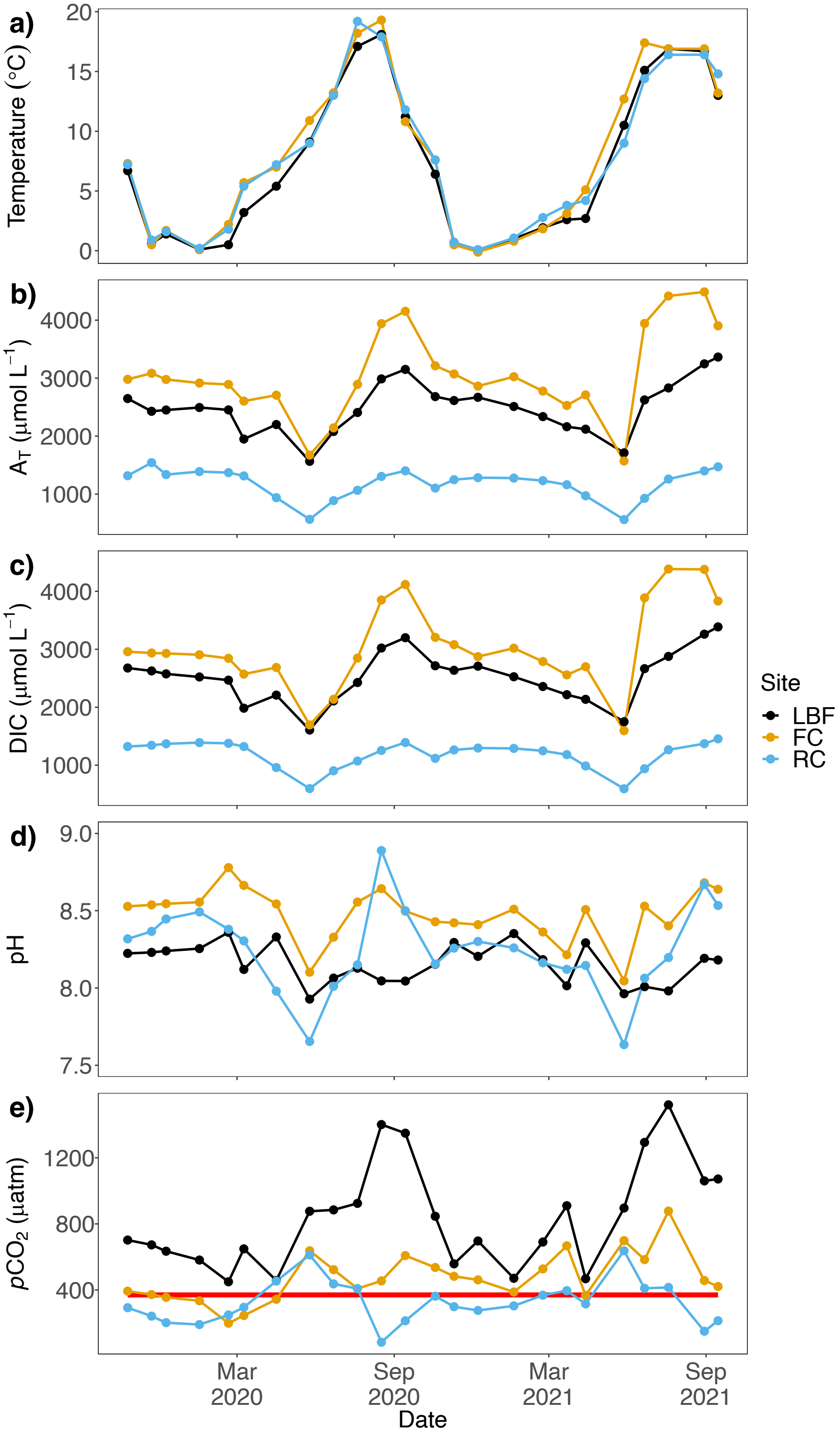

Figure S6. Spatiotemporal variability of **a)** temperature, **b)** A_T, **c)** DIC, **d)** spectrophotometric pH, and **e)** pCO$_2$ in the three tributary sites along the UCFR. The solid red line in subplot **e)** represents the average atmospheric pCO$_2$.

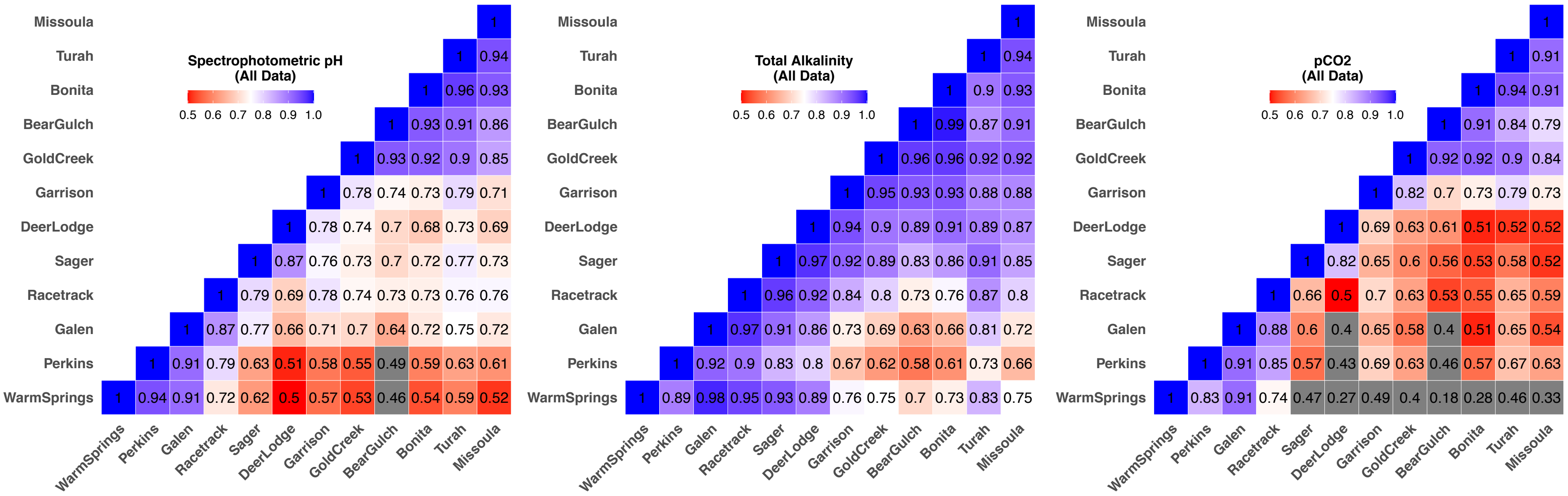

Spectrophotometric pH (All Data)

	WarmSprings	Perkins	Galen	Racetrack	Sager	DeerLodge	Garrison	GoldCreek	BearGulch	Bonita	Turah	Missoula
Missoula												1
Turah											1	0.94
Bonita										1	0.96	0.93
BearGulch									1	0.93	0.91	0.86
GoldCreek								1	0.93	0.92	0.9	0.85
Garrison							1	0.78	0.74	0.73	0.79	0.71
DeerLodge						1	0.78	0.74	0.7	0.68	0.73	0.69
Sager					1	0.87	0.76	0.73	0.7	0.72	0.77	0.73
Racetrack				1	0.79	0.69	0.78	0.74	0.73	0.73	0.76	0.76
Galen			1	0.87	0.77	0.66	0.71	0.7	0.64	0.72	0.75	0.72
Perkins		1	0.91	0.79	0.63	0.51	0.58	0.55	0.49	0.59	0.63	0.61
WarmSprings	1	0.94	0.91	0.72	0.62	0.5	0.57	0.53	0.46	0.54	0.59	0.52

Total Alkalinity (All Data)

	WarmSprings	Perkins	Galen	Racetrack	Sager	DeerLodge	Garrison	GoldCreek	BearGulch	Bonita	Turah	Missoula
Missoula												1
Turah											1	0.94
Bonita										1	0.9	0.93
BearGulch									1	0.99	0.87	0.91
GoldCreek								1	0.96	0.96	0.92	0.92
Garrison							1	0.95	0.93	0.93	0.88	0.88
DeerLodge						1	0.94	0.9	0.89	0.91	0.89	0.87
Sager					1	0.97	0.92	0.89	0.83	0.86	0.91	0.85
Racetrack				1	0.96	0.92	0.84	0.8	0.73	0.76	0.87	0.8
Galen			1	0.97	0.91	0.86	0.73	0.69	0.63	0.66	0.81	0.72
Perkins		1	0.92	0.9	0.83	0.8	0.67	0.62	0.58	0.61	0.73	0.66
WarmSprings	1	0.89	0.98	0.95	0.93	0.89	0.76	0.75	0.7	0.73	0.83	0.75

pCO2 (All Data)

	WarmSprings	Perkins	Galen	Racetrack	Sager	DeerLodge	Garrison	GoldCreek	BearGulch	Bonita	Turah	Missoula
Missoula												1
Turah											1	0.91
Bonita										1	0.94	0.91
BearGulch									1	0.91	0.84	0.79
GoldCreek								1	0.92	0.92	0.9	0.84
Garrison							1	0.82	0.7	0.73	0.79	0.73
DeerLodge						1	0.69	0.63	0.61	0.51	0.52	0.52
Sager					1	0.82	0.65	0.6	0.56	0.53	0.58	0.52
Racetrack				1	0.66	0.5	0.7	0.63	0.53	0.55	0.65	0.59
Galen			1	0.88	0.6	0.4	0.65	0.58	0.4	0.51	0.65	0.54
Perkins		1	0.91	0.85	0.57	0.43	0.69	0.63	0.46	0.57	0.67	0.63
WarmSprings	1	0.83	0.91	0.74	0.47	0.27	0.49	0.4	0.18	0.28	0.46	0.33

Figure S7. Pearson correlation (r) heatmaps of spectrophotometric pH, total alkalinity, and *p*CO_2 of all sites and water years along the UCFR. Blue represents strong positive r values and red represents moderately weak positive r values. Grey boxes indicate weak Pearson correlations with $r < 0.50$.

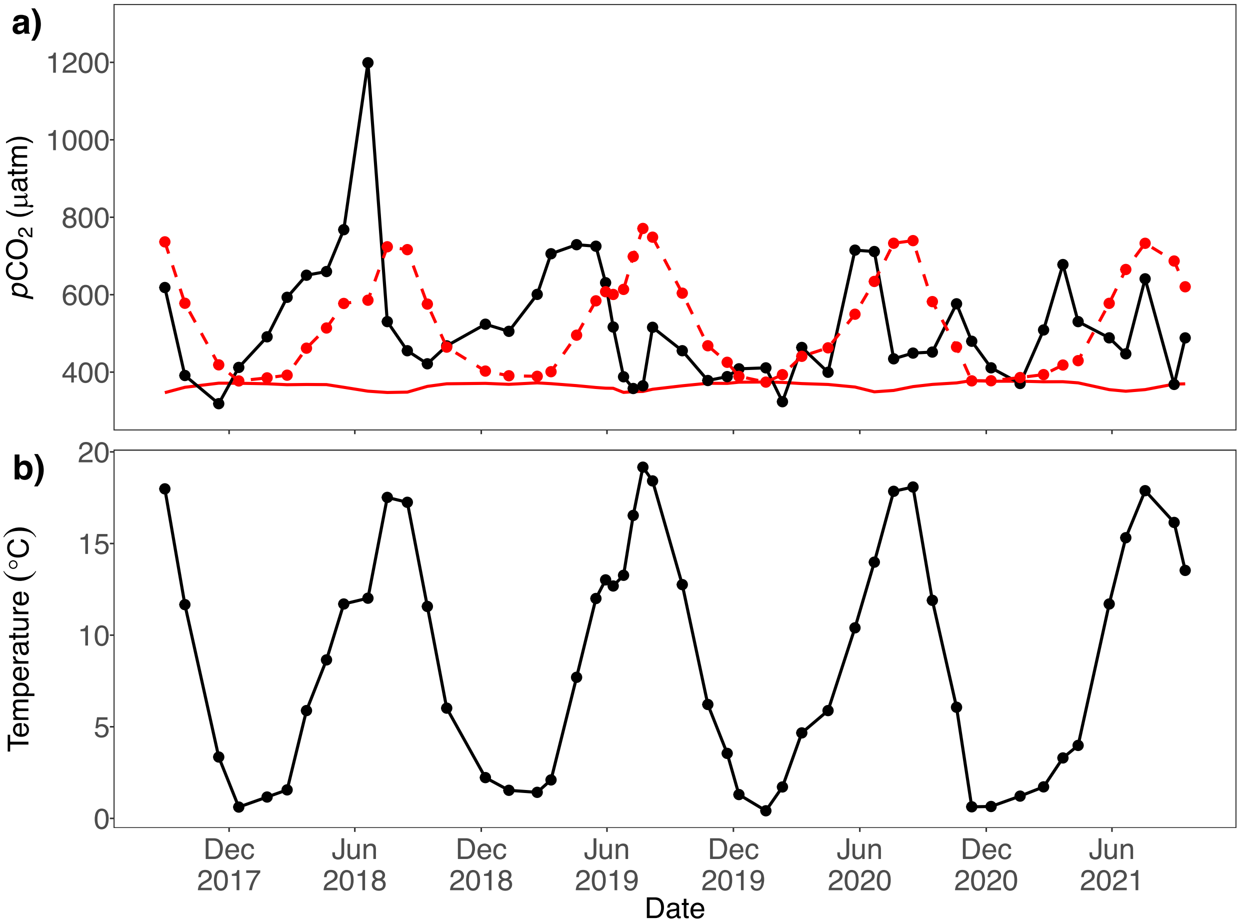

Figure S8. a) Timeseries of Riverine pCO_2 (solid black line) and temperature-driven pCO_2 (dashed red line) following Lynch et al. (2010). Data points are site-wide averages of the data presented in Figure 10 of the main text. The solid red line represents the atmospheric pCO_2. **b)** The average in situ temperature along the UCFR.

Appendix C

Supplemental Information for Chapter 4: Carbon Processing Domains: Seasonal and spatial controls on organic carbon in a montane river

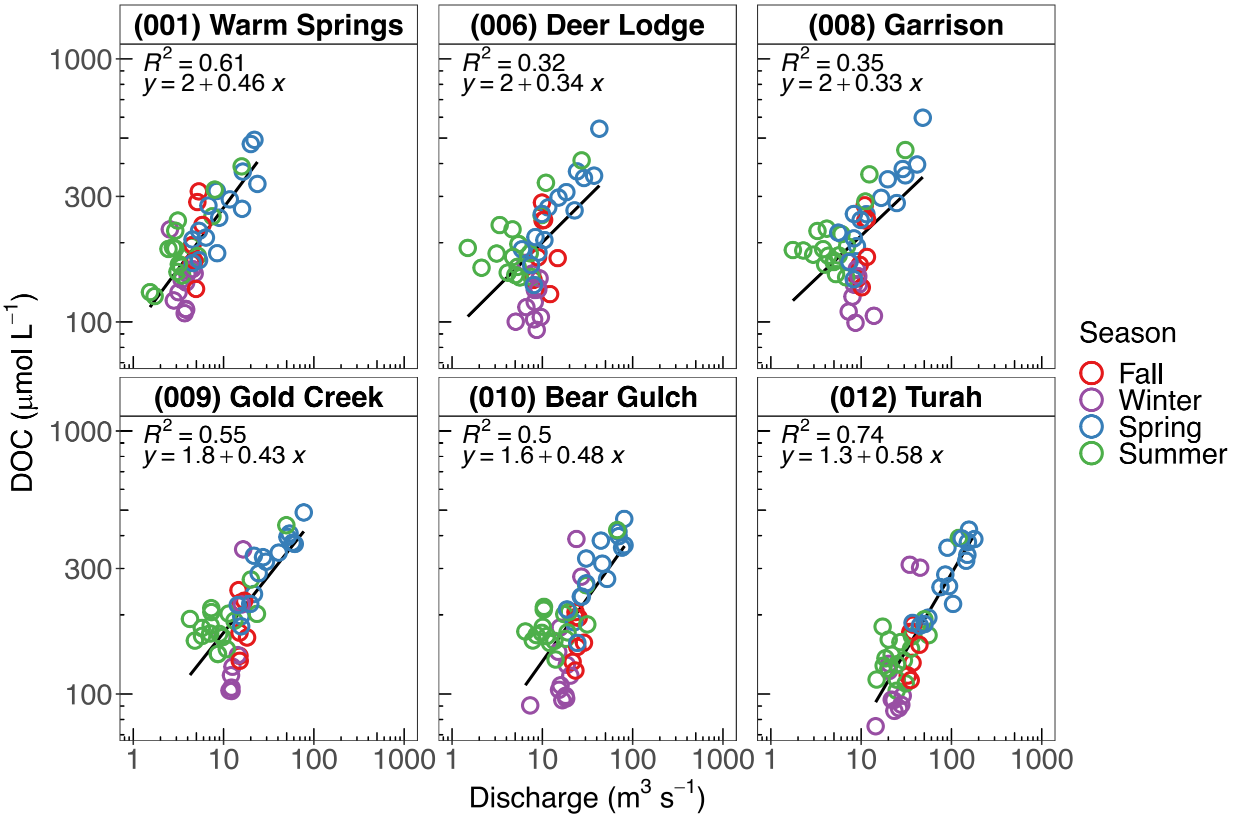

Figure S1. Log-log relationship of DOC as a function of discharge for each sampling site with a USGS gaging station. Individual points are colored by season and the coefficient of determination (R^2), and linear equation are presented in the top-left of each panel.

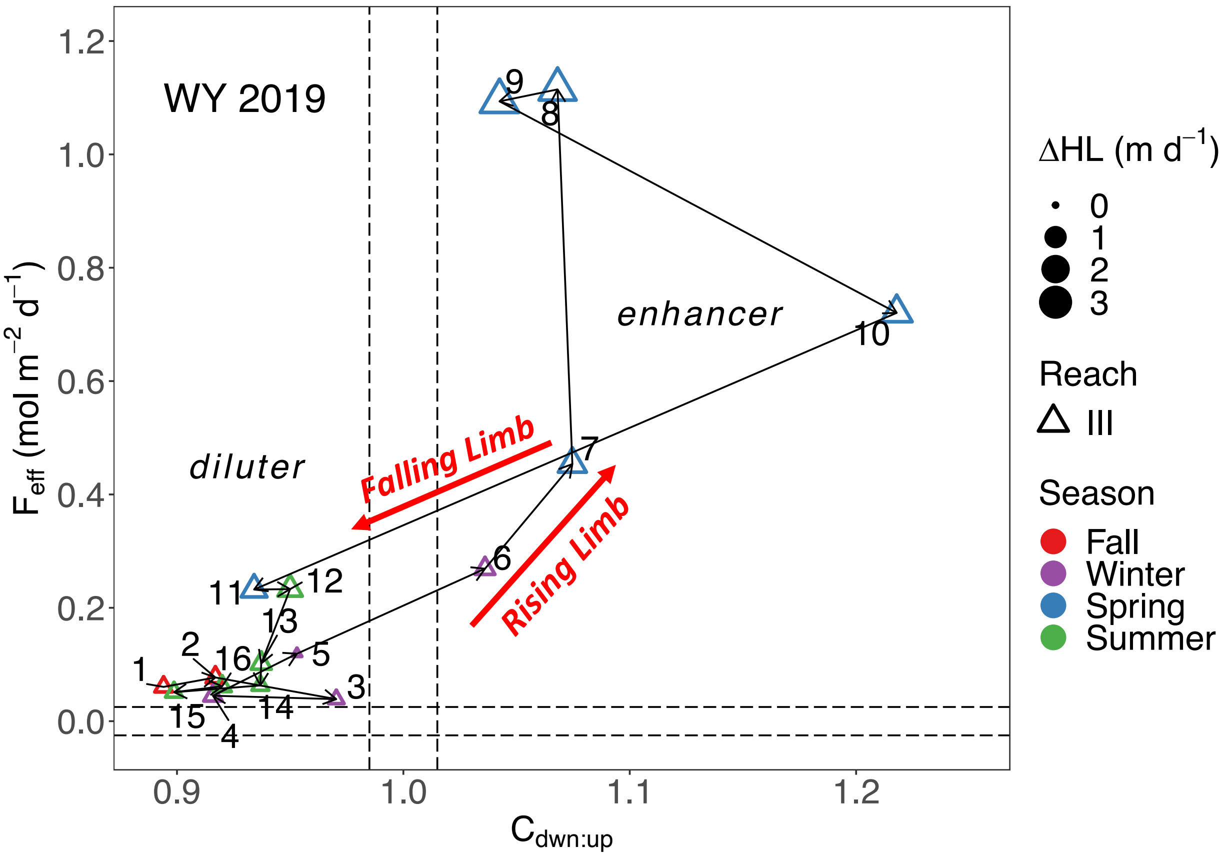

Figure S2. The processing domains for DOC in Reach III during water year 2019 as an example used to follow the progression of processing domains through seasons. The red text and lines labelled "Rising Limb" and "Falling Limb" refer to the nature of the hydrograph during this time and correspond to Figure 3b. Black numbers next to each point indicate order of data (i.e., 1 = October 2018, 10 = June 2019, 16 = September 2019). These data are taken from Figure 7 of the main text. Reaches are organized by unique symbols and each symbol is colored by season. Symbols are sized by the change in hydraulic load (ΔHL) presented in Figure 5 of the main text to depict changes in discharge. A complete list of processing domain labels can be found in Figure 7 of the main text. Black dashed lines represent the 95% null boundaries for $F_{eff} = 0$ and $C_{dwn:up} = 1$.

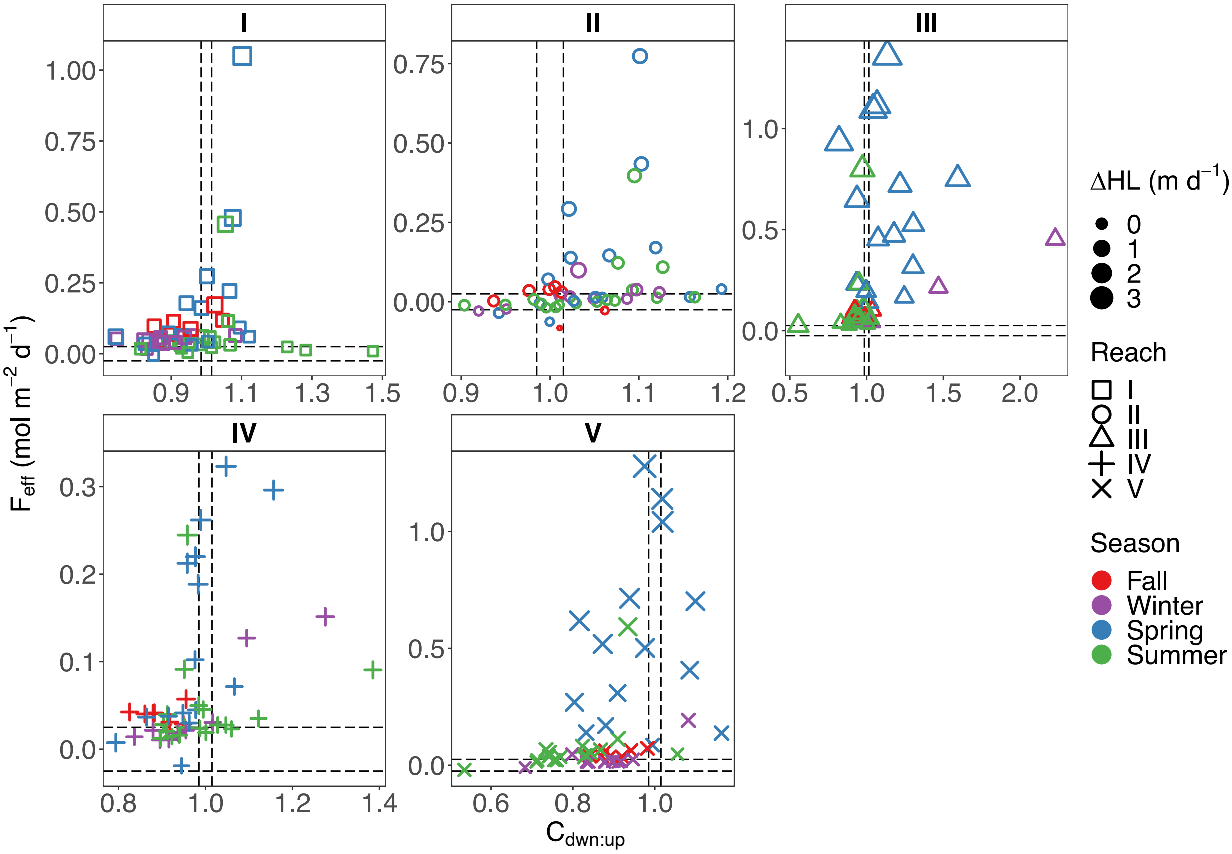

Figure S3. The processing domains for DOC for each reach in the UCFR. Note the change in scales of the x- and y-axes for each reach. Reaches are organized by unique symbols and each symbol is colored by season. Symbols are sized by the change in hydraulic load (ΔHL) presented in Figure 20 of the main text to depict changes in discharge for each reach. A complete list of processing domain labels can be found in Figure 21 of the main text. Black dashed lines represent the 95% null boundaries for $F_{eff} = 0$ and $C_{dwn:up} = 1$.

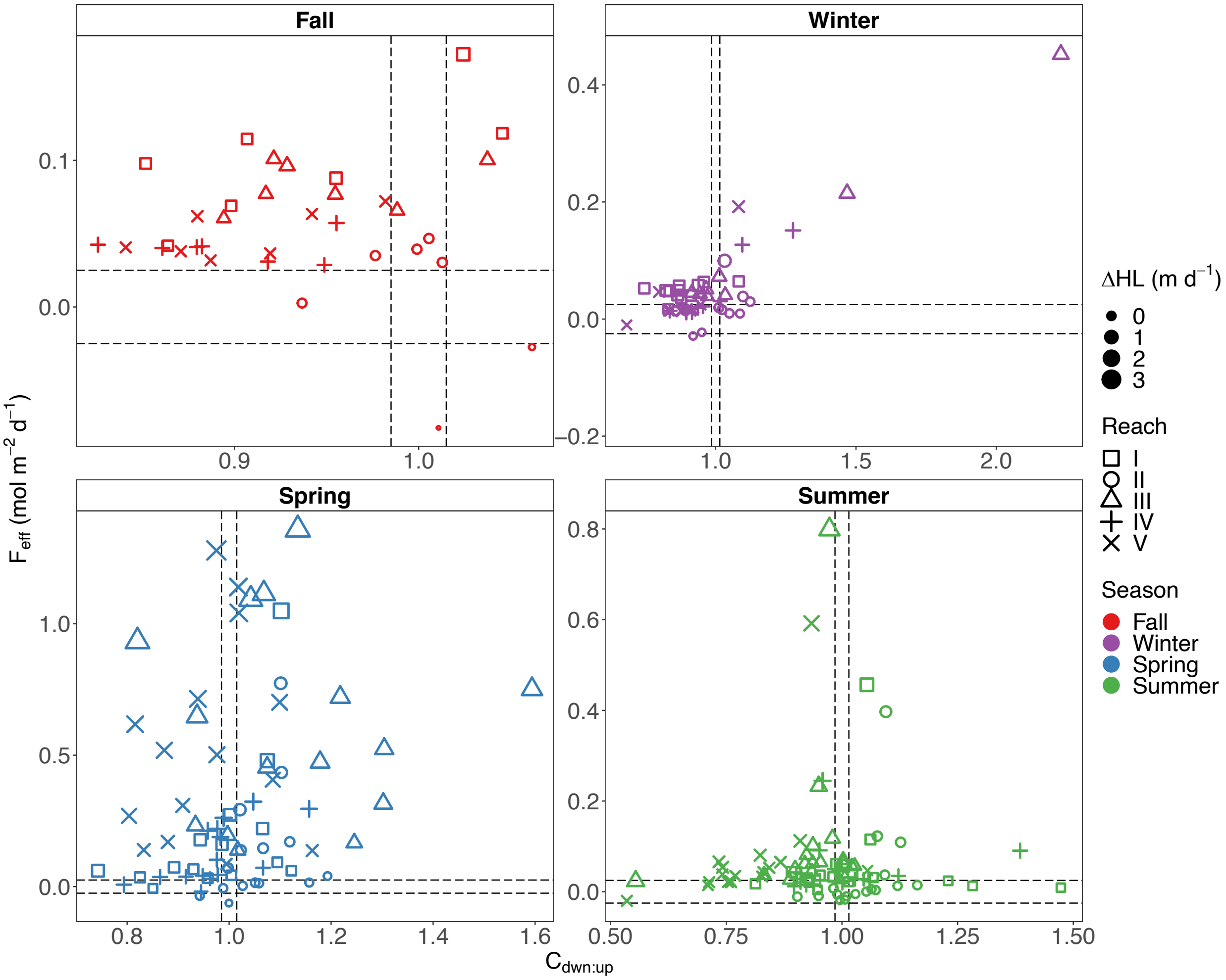

Figure S4. The processing domains for DOC for each season in the UCFR. Note the change in scales of the x- and y-axes for each season. Reaches are organized by unique symbols and each symbol is colored by season. Symbols are sized by the change in hydraulic load (ΔHL) presented in Figure 20 of the main text to depict changes in discharge for each reach. A complete list of processing domain labels can be found in Figure 21 of the main text. Black dashed lines represent the 95% null boundaries for $F_{eff} = 0$ and $C_{dwn:up} = 1$.

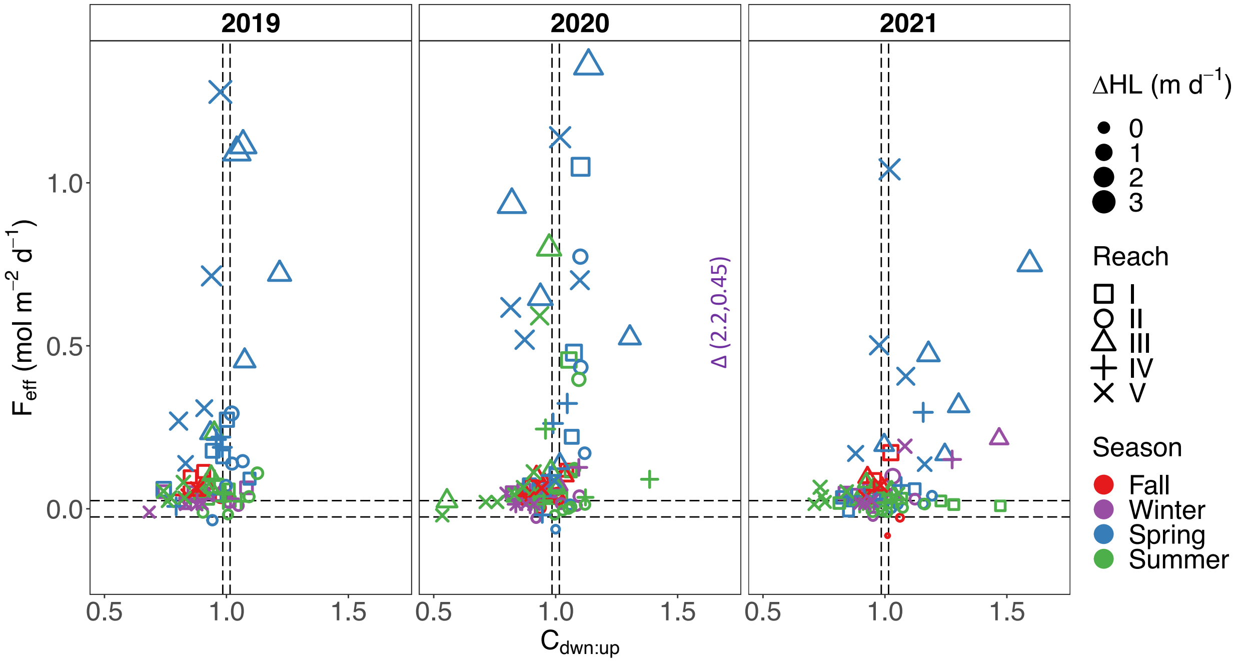

Figure S5. The processing domains for DOC in the UCFR for each water year. Reaches are organized by unique symbols and each symbol is colored by season. Symbols are sized by the change in hydraulic load (ΔHL) presented in Figure 20 of the main text to depict changes in discharge for each reach. A complete list of processing domain labels can be found in Figure 21 of the main text. Black dashed lines represent the 95% null boundaries for $F_{eff} = 0$ and $C_{dwn:up} = 1$. One point for Reach III (i.e., Δ) during water year 2020 is not plotted here because it dominates the x-axis scale. Its (x,y) coordinate is given in the 2020 subplot and colored purple to correspond to the season (i.e., winter) it represents.

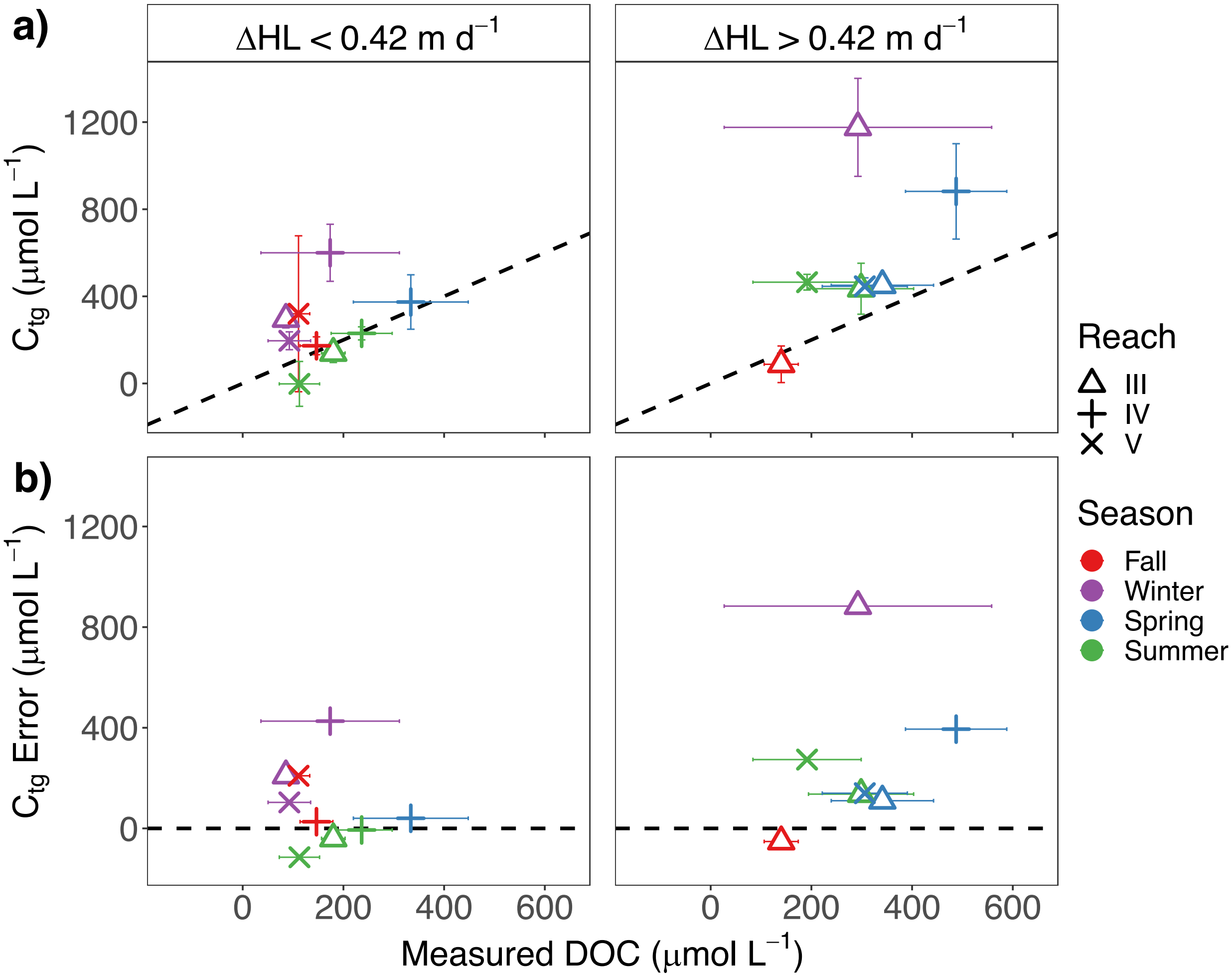

Figure S6. a) Comparison plots of C_{tg} and measured surface water samples of tributary DOC. Individual points are delineated by reach and season. The black dashed line is the 1:1 line and vertical and horizontal error bars represent the standard deviation of C_{tg} and measured tributary DOC samples, respectively. **b)** The error of estimated C_{tg} compared to measured tributary DOC. The black dashed line indicates zero error. Average C_{tg} error (estimated – measured) at $\Delta HL<0.42$ m d^{-1} is 95 ± 164 μmol L^{-1} while at $\Delta HL>0.42$ m d^{-1} it is 270 ± 304 μmol L^{-1}.

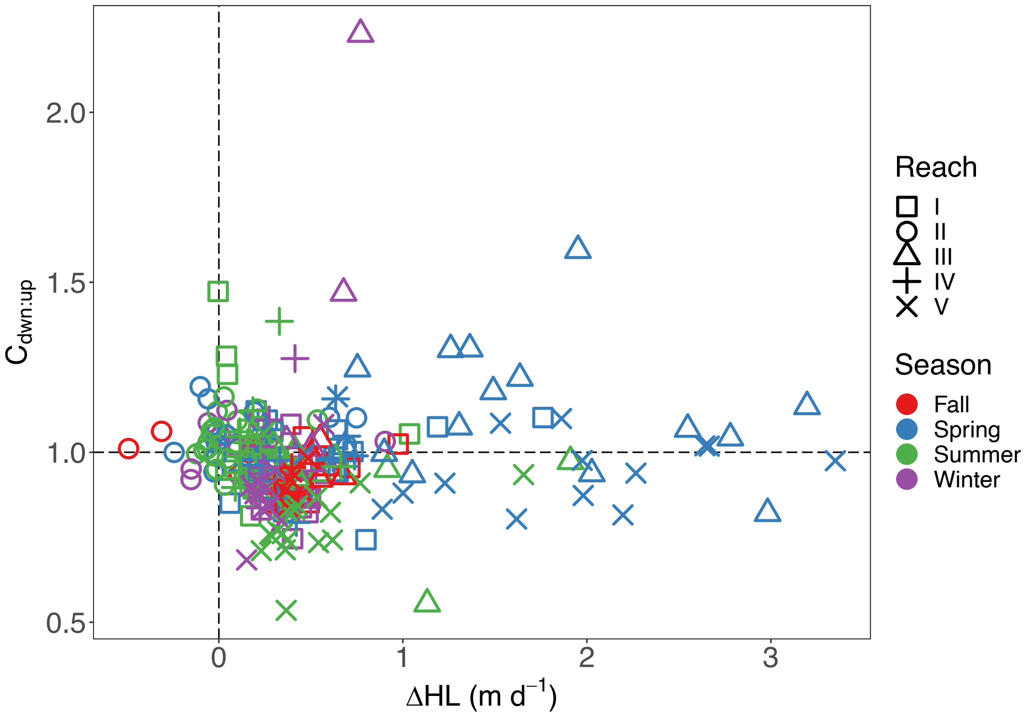

Figure S7. The relationship between ΔHL and $C_{dwn:up}$ for the DOC along the UCFR. Individual points are delineated by reach and season. The black dashed lines represent no change in discharge (ΔHL = 0) and relative concentration ($C_{dwn:up}$ = 1).

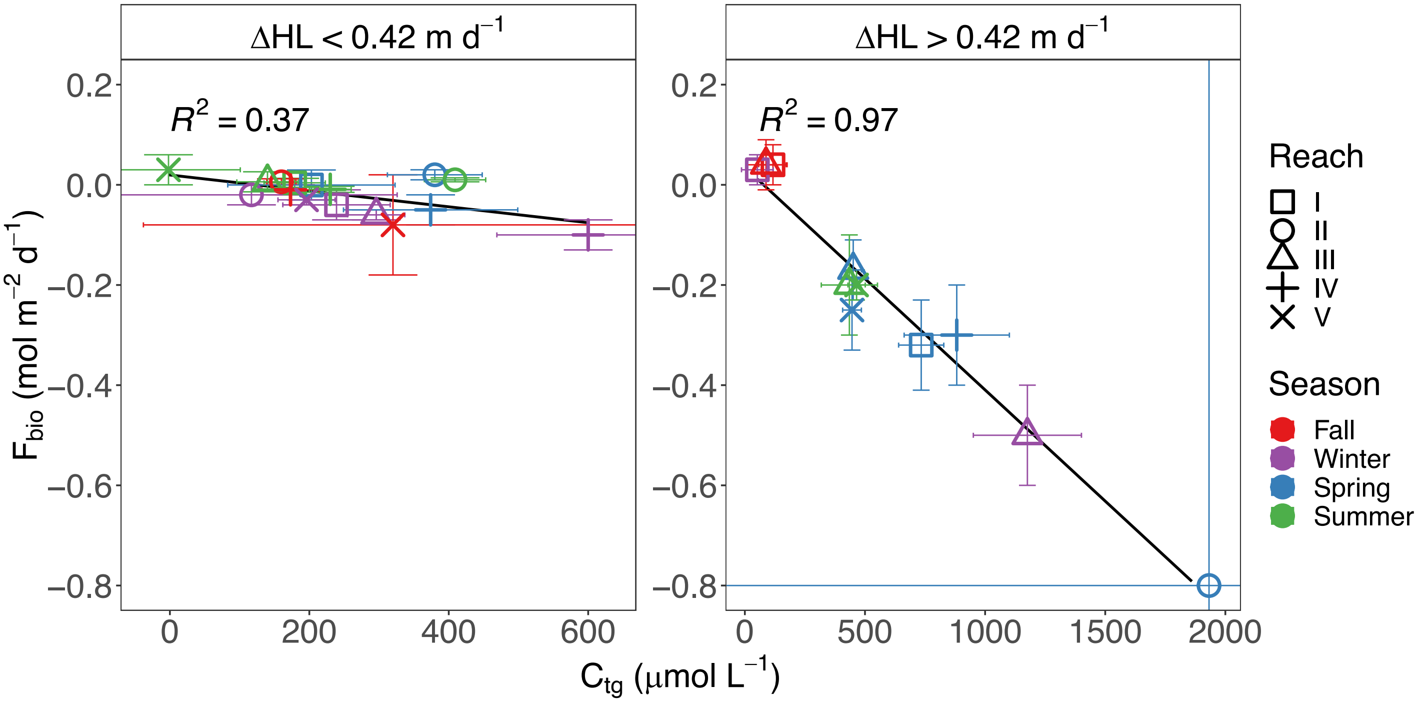

Figure S8. The relationship between derived measures of C_{tg} and F_{bio} along the UCFR separated by the breakpoint of ΔHL = 0.42 m d^{-1}. Individual points are delineated by reach and season. The lines of best fit are denoted by the solid black lines and the R^2 values are supplied in the upper right corner of each subplot. Vertical and horizontal error bars indicate the standard deviations of C_{tg} and F_{bio} for each point. Values are taken from Appendix C, Table S1.

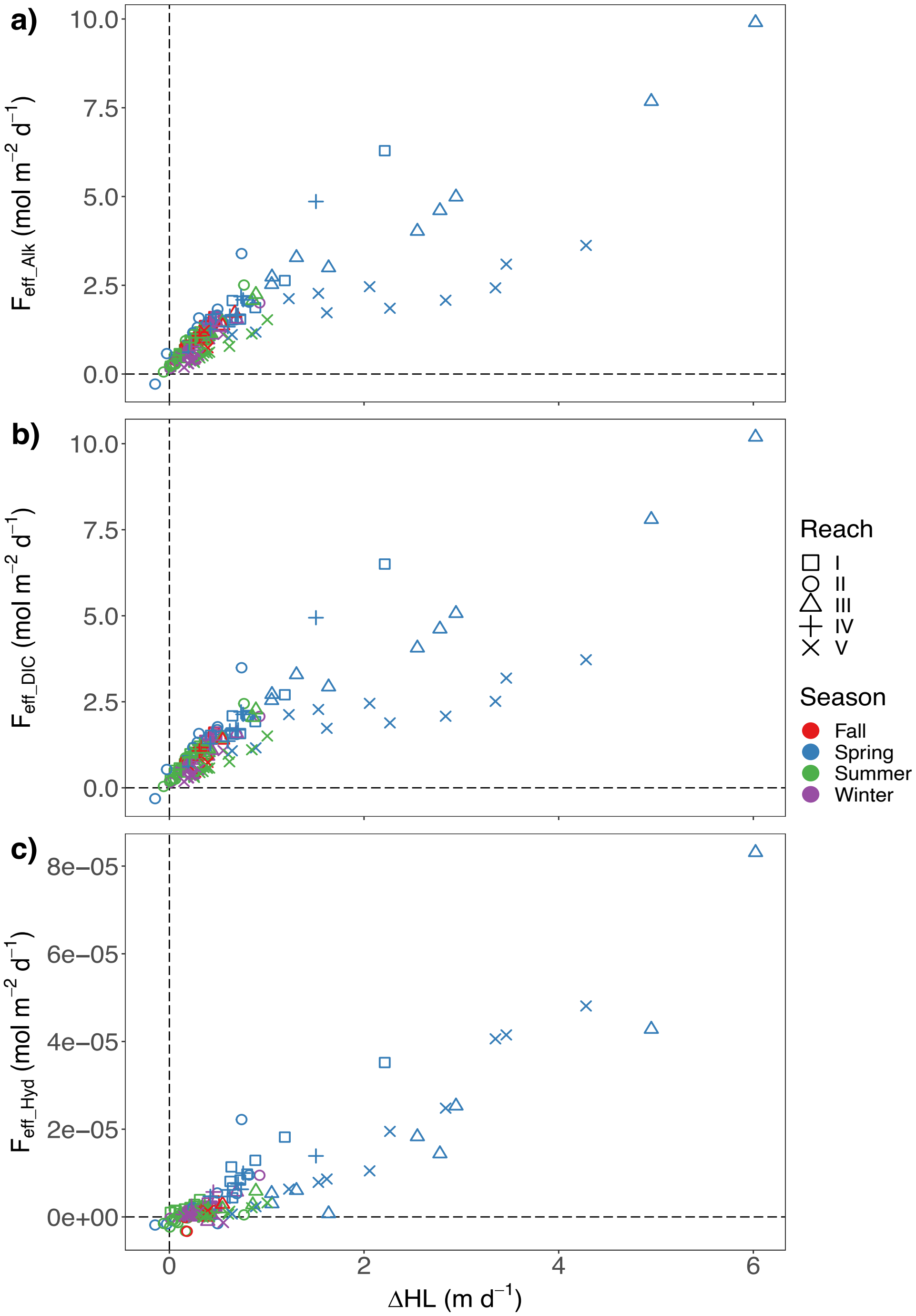

Figure S9. Effective solute flux (F_{eff}) for **a)** alkalinity (Alk), **b)** DIC, and **c)** hydrogen ion (Hyd) versus change in hydraulic load (ΔHL) across seasons and reaches in the UCFR. Reaches are represented by unique symbols colored by season. Black dashed lines represent limits for zero values. Data is for WY 2018-2020.

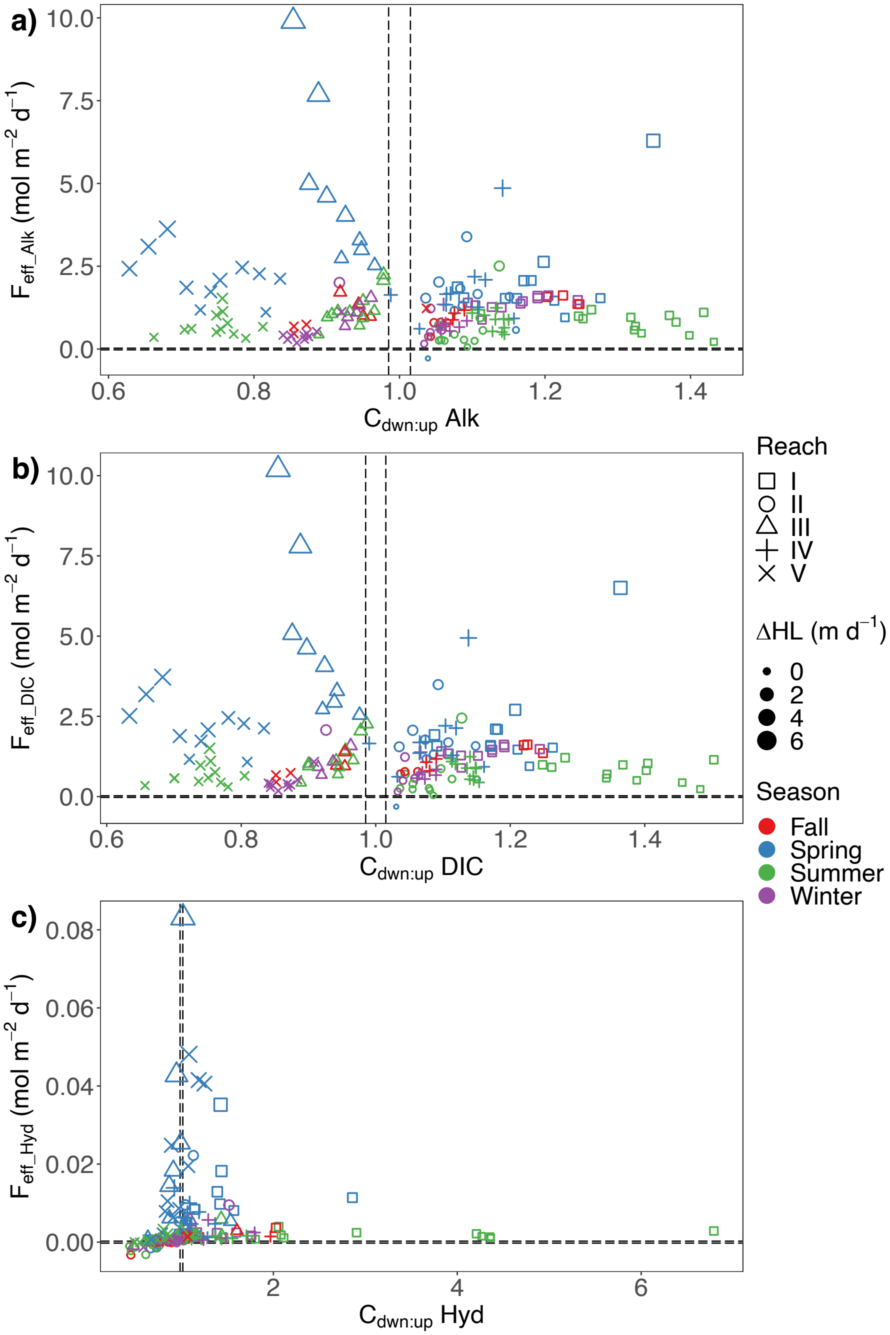

Figure S10. The processing domains for **a)** alkalinity (Alk), **b)** DIC, and **c)** hydrogen ion (Hyd) along the UCFR and include data from WY 2018-2020. Note the change in scales of the x- and y-axes for each parameter. Reaches are organized by unique symbols and each symbol is colored by season. Symbols are sized by the change in hydraulic load (ΔHL) presented in Figure 20 of the main text to depict changes in discharge for each reach. A complete list of processing domain labels can be found in Figure 21 of the main text. Black dashed lines represent the 95% null boundaries for $F_{eff} = 0$ and $C_{dwn:up} = 1$.

Table S1. Estimated C_{tg} and F_{bio} values based on linear regression analysis and organized by reach, season, and breakpoint ($\Delta HL = 0.42\ m\ d^{-1}$). NA indicates a value is not available.

Reach	C_{tg} ($\mu mol\ L^{-1}$)	F_{bio} ($mol\ m^{-2}\ d^{-1}$)	Season	ΔHL ($m\ d^{-1}$)
I	NA	NA	Fall	<0.42
I	239 ± 77^{NS}	-0.04 ± 0.03^{NS}	Winter	<0.42
I	203 ± 120^{NS}	-0.0004 ± 0.03^{NS}	Spring	<0.42
I	179 ± 44*	0.004 ± 0.009^{NS}	Summer	<0.42
II	160 ± 21*	0.006 ± 0.006^{NS}	Fall	<0.42
II	117 ± 209^{NS}	-0.02 ± 0.02^{NS}	Winter	<0.42
II	380 ± 68*	0.02 ± 0.01^{NS}	Spring	<0.42
II	409 ± 44*	0.01 ± 0.004*	Summer	<0.42
III	NA	NA	Fall	<0.42
III	296 ± 41*	-0.06 ± 0.01*	Winter	<0.42
III	NA	NA	Spring	<0.42
III	140 ± 44*	0.006 ± 0.02^{NS}	Summer	<0.42
IV	173 ± 41*	-0.01 ± 0.01^{NS}	Fall	<0.42
IV	600 ± 131*	-0.1 ± 0.03*	Winter	<0.42
IV	374 ± 125*	-0.05 ± 0.03^{NS}	Spring	<0.42
IV	230 ± 30*	-0.009 ± 0.006^{NS}	Summer	<0.42
V	320 ± 358^{NS}	-0.08 ± 0.1^{NS}	Fall	<0.42
V	196 ± 41*	-0.03 ± 0.01*	Winter	<0.42
V	NA	NA	Spring	<0.42
V	-2 ± 103^{NS}	0.03 ± 0.03^{NS}	Summer	<0.42
I	117 ± 59^{NS}	0.04 ± 0.04^{NS}	Fall	>0.42
I	52 ± 66^{NS}	0.03 ± 0.03^{NS}	Winter	>0.42
I	734 ± 94*	-0.32 ± 0.09*	Spring	>0.42
I	NA	NA	Summer	>0.42
II	NA	NA	Fall	>0.42
II	NA	NA	Winter	>0.42
II	1932 ± 2720^{NS}	-0.8 ± 1.9^{NS}	Spring	>0.42
II	NA	NA	Summer	>0.42
III	88 ± 84^{NS}	0.04 ± 0.05^{NS}	Fall	>0.42
III	1176 ± 225*	-0.5 ± 0.1*	Winter	>0.42
III	451 ± 34*	-0.17 ± 0.06*	Spring	>0.42
III	435 ± 117*	-0.2 ± 0.1^{NS}	Summer	>0.42
IV	NA	NA	Fall	>0.42
IV	NA	NA	Winter	>0.42
IV	882 ± 219*	-0.3 ± 0.1^{NS}	Spring	>0.42
IV	NA	NA	Summer	>0.42
V	NA	NA	Fall	>0.42
V	NA	NA	Winter	>0.42
V	446 ± 39*	-0.25 ± 0.08*	Spring	>0.42
V	465 ± 36*	-0.20 ± 0.03*	Summer	>0.42

^{NS}Not statistically different from zero *Statistically different from zero ($p<0.05$)

References

Abbott, B. W., G. Gruau, J. P. Zarnetske, F. Moatar, L. Barbe, Z. Thomas, O. Fovet, T. Kolbe, S. Gu, A.- C. Pierson-Wickmann, P. Davy, and G. Pinay (2018), Unexpected spatial stability of water chemistry in Headwater Stream Networks, *Ecology Letters*, *21*(2), 296–308, doi:10.1111/ele.12897.

Åberg, J., and M. Wallin. (2014), Evaluating a fast headspace method for measuring DIC and subsequent calculation of $p\mathrm{CO_2}$ in freshwater systems, *Inland Waters*, 4: 157–166. doi:10.5268/iw-4.2.694

Abril, G., F. Guérin, S. Richard, R. Delmas, C. Galy-Lacaux, P. Gosse, A. Tremblay, L. Varfalvy, M. A. Dos Santos, and B. Matvienko (2005), Carbon dioxide and methane emissions and the carbon budget of a 10-year old Tropical Reservoir (Petit Saut, French guiana), *Global Biogeochemical Cycles*, *19*(4), doi:10.1029/2005gb002457.

Abril, G., J.-M. Martinez, L. F. Artigas, and others (2014), Amazon River carbon dioxide outgassing fueled by wetlands, *Nature*, 505: 395–398. doi:10.1038/nature12797

Abril, G. et al. (2015), Technical note: Large overestimation of $p\mathrm{CO_2}$ calculated from pH and alkalinity in acidic, organic-rich freshwaters, *Biogeosciences*, *12*(1), 67–78, doi:10.5194/bg-12-67-2015.

Ågren, A., I. Buffam, K. Bishop, and H. Laudon (2010), Modeling stream dissolved organic carbon concentrations during spring flood in the Boreal Forest: A simple empirical approach for regional predictions, *Journal of Geophysical Research*, *115*(G1), doi:10.1029/2009jg001013.

Aho, K. S., J. D. Hosen, L. A. Logozzo, W. R. McGillis, and P. A. Raymond (2021), Highest rates of gross primary productivity maintained despite $\mathrm{CO_2}$ depletion in a temperate river network, *Limnology and Oceanography Letters*, 6: 200–206. doi:10.1002/lol2.10195

Aldridge, F. J., A. D. Chapman, C. L. Schelske, and R. W. Brody (1998), Interaction of light, nutrients and phytoplankton in a Blackwater River, St. Johns River, Florida, USA, *Internationale Vereinigung für theoretische und angewandte Limnologie: Verhandlungen*, *26*(4), 1665–1669, doi:10.1080/03680770.1995.11901012.

Alin, S. R., M. de Rasera, C. I. Salimon, J. E. Richey, G. W. Holtgrieve, A. V. Krusche, and A. Snidvongs (2011), Physical controls on carbon dioxide transfer velocity and flux in low-gradient river systems and implications for regional carbon budgets, *Journal of Geophysical Research*, *116*(G1), doi:10.1029/2010jg001398.

Amon, R. M., and R. Benner (1996), Bacterial utilization of different size classes of dissolved organic matter, *Limnology and Oceanography*, *41*(1), 41–51, doi:10.4319/lo.1996.41.1.0041.

Andrews, A., Kofler,J., Trudeau, M.E., Bakwin, P.S., Fisher, M.L., Sweeney, C., Desai, A.R., and NOAA ESRL (2017), Earth System Research Laboratory Carbon Cycle and Greenhouse Gases Group Continuous Measurements of CO_2, CO, and CH_4 from Tall Towers, 1992-Present, Version 1. NOAA National Centers for Environmental Information. doi: 10.7289/V57W69F2.

Annual Water Quality Report (AWQR) (2020), PDF, Missoula, MT. City of Missoula. Available from: https://www.ci.missoula.mt.us/DocumentCenter/View/52629/2020-CCR---Missoula-Water?bidId=

Appling, A. P., J. S. Read, L. A. Winslow, and others (2018a), The metabolic regimes of 356 rivers in the United States, *Scientific Data*, 5. doi:10.1038/sdata.2018.292

Appling, A. P., R. O. Hall, C. B. Yackulic, and M. Arroita (2018b), Overcoming equifinality: Leveraging long time series for stream metabolism estimation, *Journal of Geophysical Research: Biogeosciences*, 123: 624–645. doi:10.1002/2017jg004140

Arroita, M., A. Elosegi, and R. O. Hall (2019), Twenty years of daily metabolism show riverine recovery following sewage abatement, *Limnology and Oceanography*, 64. doi:10.1002/lno.11053

Asano, Y., T. Uchida, Y. Mimasu, and N. Ohte (2009), Spatial patterns of stream solute concentrations in a steep mountainous catchment with a homogeneous landscape, *Water Resources Research*, *45*(10), doi:10.1029/2008wr007466.

Atkinson, C. L., B. C. van Ee, Y. H. Lu, and W. Zhong (2019), Wetland floodplain flux: Temporal and spatial availability of organic matter and dissolved nutrients in an unmodified river, *Biogeochemistry*, *142*(3), 395–411, doi:10.1007/s10533-019-00542-z.

Aucour, A.-M., S. M. F. Sheppard, O. Guyomar, and J. Wattelet (1999), Use of ^{13}C to trace origin and cycling of inorganic carbon in the Rhône River system, *Chemical Geology*, *159*(1-4), 87–105, doi:10.1016/s0009-2541(99)00035-2.

Aufdenkampe, A. K., E. Mayorga, P. A. Raymond, J. M. Melack, S. C. Doney, S. R. Alin, R. E. Aalto, and K. Yoo (2011), Riverine coupling of biogeochemical cycles between land, oceans, and atmosphere, *Frontiers in Ecology and the Environment*, 9: 53–60. doi:10.1890/100014

Baker, M. A., H. M. Valett, and C. N. Dahm (2000), Organic carbon supply and metabolism in a shallow groundwater ecosystem, *Ecology*, *81*(11), 3133–3148, doi:10.1890/0012-9658(2000)081[3133:ocsami]2.0.co;2.

Baldwin, D. S., M. J. Colloff, S. M. Mitrovic, N. R. Bond, and B. Wolfenden (2016), Restoring dissolved organic carbon subsidies from floodplains to Lowland River Food Webs: A role for environmental flows?, *Marine and Freshwater Research*, *67*(9), 1387, doi:10.1071/mf15382.

Ball, J. W., and D. K. Nordstrom (1991), WATEQ4F -- User's manual with revised thermodynamic data base and test cases for calculating speciation of major, trace and redox elements in natural waters, *Open-File Report*, doi:10.3133/ofr90129

Baum, A., T. Rixen, and J. Samiaji (2007), Relevance of peat draining rivers in central Sumatra for the riverine input of dissolved organic carbon into the Ocean, *Estuarine, Coastal and Shelf Science*, *73*(3-4), 563–570, doi:10.1016/j.ecss.2007.02.012.

Berggren, M., L. Ström, H. Laudon, J. Karlsson, A. Jonsson, R. Giesler, A.-K. Bergström, and M. Jansson (2010), Lake secondary production fueled by rapid transfer of low molecular weight organic carbon from terrestrial sources to aquatic consumers, *Ecology Letters*, *13*(7), 870–880, doi:10.1111/j.1461-0248.2010.01483.x.

Bernal, S., A. Lupon, W. M. Wollheim, F. Sabater, S. Poblador, and E. Martí (2019), Supply, demand, and in-stream retention of dissolved organic carbon and nitrate during storms in Mediterranean forested headwater streams, *Frontiers in Environmental Science*, *7*, doi:10.3389/fenvs.2019.00060.

Bernhardt, E. S., and G. E. Likens (2002), Dissolved organic carbon enrichment alters nitrogen dynamics in a forest stream, *Ecology*, *83*(6), 1689–1700, doi:10.1890/0012-9658(2002)083[1689:docean]2.0.co;2.

Bianchi, T. S., T. Filley, K. Dria, and P. G. Hatcher (2004), Temporal variability in sources of dissolved organic carbon in the lower mississippi river, *Geochimica et Cosmochimica Acta*, *68*(5), 959–967, doi:10.1016/j.gca.2003.07.011.

Bockmon, E. E., and A. G. Dickson (2015), An inter-laboratory comparison assessing the quality of seawater carbon dioxide measurements, *Marine Chemistry*, 171: 36–43. doi:10.1016/j.marchem.2015.02.002

Boyer, E. W., G. M. Hornberger, K. E. Bencala, and D. M. McKnight (1997), Response characteristics of doc flushing in an Alpine catchment, *Hydrological Processes*, *11*(12), 1635–1647, doi:10.1002/(sici)1099-1085(19971015)11:12<1635::aid-hyp494>3.0.co;2-h.

Brardinoni, F., and M. A. Hassan (2006), Glacial erosion, evolution of river long profiles, and the organization of process domains in mountain drainage basins of coastal British Columbia, *Journal of Geophysical Research*, *111*(F1), doi:10.1029/2005jf000358.

Butman, D., and P. A. Raymond (2011), Significant efflux of carbon dioxide from streams and rivers in the United States, *Nature Geoscience*, 4: 839–842. doi:10.1038/ngeo1294

Byrne, R. H., G. Robert-Baldo, S. W. Thompson, and C. T. A. Chen (1988), Seawater pH measurements: An at-sea comparison of spectrophotometric and potentiometric methods, *Deep Sea Research Part A. Oceanographic Research Papers*, 35: 1405–1410. doi:10.1016/0198-0149(88)90091-x

Byrne, R. H., S. Mecking, R. A. Feely, and X. Liu (2010), Direct observations of basin-wide acidification of the North Pacific Ocean, *Geophysical Research Letters*, 37. doi:10.1029/2009gl040999

Chauvaud, L., J. K. Thompson, J. E. Cloern, and G. Thouzeau (2003), Clams as CO_2 generators: The *potamocorbula amurensis* example in San Francisco Bay, *Limnology and Oceanography*, *48*(6), 2086–2092, doi:10.4319/lo.2003.48.6.2086.

Chen, C.-T. A., T.-H. Huang, Y.-H. Fu, Y. Bai, and X. He (2012), Strong sources of CO_2 in upper estuaries become sinks of CO_2 in large river plumes, *Current Opinion in Environmental Sustainability*, 4: 179–185. doi:10.1016/j.cosust.2012.02.003

Choi, J., S. M. Hulseapple, M. H. Conklin, and J. W. Harvey (1998), Modeling CO_2 degassing and pH in a stream–aquifer system, *Journal of Hydrology*, 209: 297–310. doi:10.1016/s0022-1694(98)00093-6

Ciais, P., A. V. Borges, G. Abril, M. Meybeck, G. Folberth, D. Hauglustaine, and I. A. Janssens (2008), The impact of lateral carbon fluxes on the European Carbon Balance, *Biogeosciences*, *5*(5), 1259–1271, doi:10.5194/bg-5-1259-2008.

Coles, J. F., Riva-Murray, K., Van Metre, P. C., Button, D. T., Bell, A. H., Qi, S. L., Journey, C. A., and Sheibley, R. W (2019), Design and methods of the U.S. Geological Survey Northeast Stream Quality Assessment (NESQA): U.S. Geological Survey, *Open-File Report 2018–1183*, 46 p., https://doi.org/10.3133/ofr20181183.

Cole, J. J., and N. F. Caraco (2001), Carbon in catchments: Connecting terrestrial carbon losses with aquatic metabolism, *Marine and Freshwater Research*, 52: 101. doi:10.1071/mf00084

Cole, J. J., Y. T. Prairie, N. F. Caraco, and others (2007), Plumbing the global carbon cycle: Integrating inland waters into the terrestrial carbon budget, *Ecosystems*, 10: 172–185. doi:10.1007/s10021-006-9013-8

Cook, R.A., B. Gawne, R. Petrie, D.S. Baldwin, G.N. Rees, D.L. Nielsen, and N.S.P. Ning

(2015), River metabolism and carbon dynamics in response to flooding in a lowland river, *Marine and Freshwater Research*, *66*(10), 919, doi:10.1071/mf14199.

Cormier, S. M., S. P. Wilkes, and L. Zheng (2013), Relationship of land use and elevated ionic strength in Appalachian watersheds, *Environmental Toxicology and Chemistry*, 32: 296–303. doi:10.1002/etc.2055

Cory, R. M., C. P. Ward, B. C. Crump, and G. W. Kling (2014), Sunlight controls water column processing of carbon in Arctic Fresh Waters, *Science*, *345*(6199), 925–928, doi:10.1126/science.1253119.

Dai, M., Z. Yin, F. Meng, Q. Liu, and W.-J. Cai (2012), Spatial distribution of riverine DOC inputs to the ocean: An updated Global Synthesis, *Current Opinion in Environmental Sustainability*, *4*(2), 170–178, doi:10.1016/j.cosust.2012.03.003.

D'Andrilli, J., W. T. Cooper, C. M. Foreman, and A. G. Marshall (2015), An ultrahigh-resolution mass spectrometry index to estimate natural organic matter lability, *Rapid Communications in Mass Spectrometry*, *29*(24), 2385–2401, doi:10.1002/rcm.7400.

Dawson, J. J., D. Tetzlaff, M. Speed, M. Hrachowitz, and C. Soulsby (2011), Seasonal controls on DOC Dynamics in nested upland catchments in NE Scotland, *Hydrological Processes*, *25*(10), 1647–1658, doi:10.1002/hyp.7925.

DeGrandpre, M. D., T. R. Hammar, S. P. Smith, and F. L. Sayles (1995), In situ measurements of seawater $p\mathrm{CO}_2$, *Limnology and Oceanography*, 40: 969–975. doi:10.4319/lo.1995.40.5.0969

DeGrandpre, M. D., R. S. Spaulding, J. O. Newton, E. J. Jaqueth, S. E. Hamblock, A. A. Umansky, and K. E. Harris (2014), Considerations for the measurement of spectrophotometric pH for ocean acidification and other studies, *Limnology and Oceanography: Methods*, 12: 830–839. doi:10.4319/lom.2014.12.830

DeGrandpre, M. D., C. Z. Lai, M. L. Timmermans, R. A. Krishfield, A. Proshutinsky, and D. Torres (2019), Inorganic carbon and $p\mathrm{CO}_2$ variability during ice formation in the Beaufort Gyre of the Canada Basin, *Journal of Geophysical Research: Oceans*, 124: 4017–4028. doi:10.1029/2019jc015109

DeGrandpre, M.D. and F.L. Young (2021a), Water year 2017-18 monitoring of the inorganic carbon system (pH and total alkalinity) in the Upper Clark Fork River (Montana, USA) ver 1, Environmental Data Initiative, https://doi.org/10.6073/pasta/e0e56f55511e28bf3277e48c39149909

DeGrandpre, M.D. and F.L. Young (2021b), Water year 2019 monitoring of the inorganic carbon system (pH and total alkalinity) in the Upper Clark Fork River (Montana, USA) ver 1, Environmental Data Initiative, https://doi.org/10.6073/pasta/07a6d59c7a88c28deec55874f902f998

DeGrandpre, M.D. and F.L. Young (2021c), Water year 2020 monitoring of the inorganic carbon system (pH and total alkalinity) in the Upper Clark Fork River (Montana, USA) ver 1, Environmental Data Initiative, https://doi.org/10.6073/pasta/1686551524b835586d3e4ac2df170f94 (Accessed 2021-10-11).

DeGrandpre, M.D., F.L. Young, H.M. Valett, and C. Utzman (2021a), Concentration of dissolved organic carbon in water samples taken from the Upper Clark Fork River (Montana, USA) during water years 2017 and 2018 (1 Oct 2016 - 30 Sep 2018) ver 1, Environmental Data Initiative, https://doi.org/10.6073/pasta/8c210f2c3ab49612fc852f4b272c5144 (Accessed 2021-10-11).

DeGrandpre, M.D., F.L. Young, H.M. Valett, and C. Utzman (2021b), Concentration of dissolved organic carbon in water samples taken from the Upper Clark Fork River (Montana, USA) during water year 2019 (1 Oct 2018 - 30 Sep 2019) ver 1, Environmental Data Initiative, https://doi.org/10.6073/pasta/111eceba2dc9d13eb394d889e4841025 (Accessed 2022-01-06).

DeGrandpre, M.D., F.L. Young, H.M. Valett, and C. Utzman (2021c), Concentration of dissolved organic carbon in water samples taken from the Upper Clark Fork River (Montana, USA) during water year 2020 (1 Oct 2019 - 30 Sep 2020) ver 1, Environmental Data Initiative, https://doi.org/10.6073/pasta/0ce978dead958c0b0cfae8cdea0d7160 (Accessed 2022-01-06).

Dent, C. L., and N. B. Grimm (1999), Spatial heterogeneity of stream water nutrient concentrations over successional time, *Ecology*, *80*(7), 2283–2298, doi:10.1890/0012-9658(1999)080[2283:shoswn]2.0.co;2.

Dickson, A. G., C. L. Sabine, and J. R. Christian (2007), Guide to best practices for ocean CO_2 measurements, *North Pacific Marine Science Organization*.

Dodds, W. K. (2006), Eutrophication and trophic state in rivers and streams, *Limnology and Oceanography*, *51*(1part2), 671–680, doi:10.4319/lo.2006.51.1_part_2.0671.

Dodds, W. K., F. Tromboni, W. Aparecido Saltarelli, and D. G. Fernandes Cunha (2017), The root of the problem: Direct influence of riparian vegetation on estimation of stream ecosystem metabolic rates, *Limnology and Oceanography Letters*, 2: 9–17. doi:10.1002/lol2.10032

Drakare, S., P. Blomqvist, A.-K. Bergström, and M. Jansson (2002), Primary production and phytoplankton composition in relation to DOC input and bacterioplankton production in Humic Lake örträsket, *Freshwater Biology*, *47*(1), 41–52, doi:10.1046/j.1365-2427.2002.00779.x.

Duvert, C., D. E. Butman, A. Marx, O. Ribolzi, and L. B. Hutley (2018), CO_2 evasion along streams driven by groundwater inputs and geomorphic controls, *Nature Geoscience*, 11: 813–818. doi:10.1038/s41561-018-0245-y

Ensign, S. H., and M. W. Doyle (2006), Nutrient spiraling in streams and river networks, *Journal of Geophysical Research: Biogeosciences*, *111*(G4), doi:10.1029/2005jg000114.

Ensign, S. H., M. W. Doyle, and J. R. Gardner (2017), New strategies for measuring rates of environmental processes in rivers, lakes, and Estuaries, *Freshwater Science*, *36*(3), 453–465, doi:10.1086/692998.

Evans, C., and T. D. Davies (1998), Causes of concentration/discharge hysteresis and its potential as a tool for analysis of episode hydrochemistry, *Water Resources Research*, *34*(1), 129–137, doi:10.1029/97wr01881.

Finlay, J. C. (2001), Stable-carbon-isotope ratios of river biota: Implications for energy flow in Lotic Food Webs, *Ecology*, *82*(4), 1052, doi:10.2307/2679902.

Finlay, K., P. R. Leavitt, A. Patoine, A. Patoine, and B. Wissel (2010), Magnitudes and controls of organic and inorganic carbon flux through a chain of hard-water lakes on the Northern Great Plains, *Limnology and Oceanography*, *55*(4), 1551–1564, doi:10.4319/lo.2010.55.4.1551.

Fisher, S. G., L. J. Gray, N. B. Grimm, and D. E. Busch (1982), Temporal succession in a desert stream ecosystem following flash flooding, *Ecological Monographs*, *52*(1), 93–110, doi:10.2307/2937346.

French, C. R., J. J. Carr, E. M. Dougherty, L. A. K. Eidson, J. C. Reynolds, and M. D. DeGrandpre (2002), Spectrophotometric pH measurements of freshwater, *Analytica Chimica Acta*, 453: 13–20. doi:10.1016/s0003-2670(01)01509-4

Garnier, J., and G. Billen (2007), Production vs. respiration in river systems: An indicator of an "ecological status," *Science of The Total Environment*, *375*(1-3), 110–124, doi:10.1016/j.scitotenv.2006.12.006.

Godsey, S. E., J. W. Kirchner, and D. W. Clow (2009), Concentration-discharge relationships reflect chemostatic characteristics of US catchments, *Hydrological Processes*, *23*(13), 1844–1864, doi:10.1002/hyp.7315.

Gran, G. (1952), Determination of the equivalence point in potentiometric titrations, *Part II. The Analyst*, 77: 661. doi:10.1039/an9527700661

Gray, S. E., M. D. DeGrandpre, C. Langdon, and J. E. Corredor (2012), Short-term and seasonal pH, pCO_2 and saturation state variability in a coral-reef ecosystem, *Global Biogeochemical Cycles*, 26. doi:10.1029/2011gb004114

Griffin, B. A., and J. J. Jurinak (1973), Estimation of activity coefficients from the electrical conductivity of natural aquatic systems and soil extracts, *Soil Science*, 116: 26–30. doi:10.1097/00010694-197307000-00005

Griffith, M. B. (2014), Natural variation and current reference for specific conductivity and major ions in wadeable streams of the Conterminous USA, *Freshwater Science*, *33*(1), 1–17, doi:10.1086/674704.

Hall Jr., R. O., and H. L. Madinger (2018), Use of argon to measure gas exchange in turbulent mountain streams, *Biogeosciences*, *15*(10), 3085–3092, doi:10.5194/bg-15-3085-2018.

Heath, C. R., B. C. Leadbeater, and M. E. Callow (1995), Effect of inhibitors on calcium carbonate deposition mediated by freshwater algae, *Journal of Applied Phycology*, *7*(4), 367–380, doi:10.1007/bf00003794.

Hélie, J.-F., C. Hillaire-Marcel, and B. Rondeau (2002), Seasonal changes in the sources and fluxes of dissolved inorganic carbon through the St. Lawrence River—isotopic and chemical constraint, *Chemical Geology*, *186*(1-2), 117–138, doi:10.1016/s0009-2541(01)00417-x.

Herczeg, A. L., and R. H. Hesslein (1984), Determination of hydrogen ion concentration in softwater lakes using carbon dioxide equilibria, *Geochimica et Cosmochimica Acta*, 48: 837–845. doi:10.1016/0016-7037(84)90105-4

Hilton, R. G., A. Galy, and N. Hovius (2008), Riverine Particulate Organic Carbon from an active mountain belt: Importance of landslides, *Global Biogeochemical Cycles*, *22*(1), doi:10.1029/2006gb002905.

Holmes, R. M., J. W. McClelland, P. A. Raymond, B. B. Frazer, B. J. Peterson, and M. Stieglitz (2008), Lability of doc transported by Alaskan rivers to the Arctic Ocean, *Geophysical Research Letters*, *35*(3), doi:10.1029/2007gl032837.

Hood, E., M.N. Gooseff, and S.L. Johnson (2006), Changes in the character of stream water dissolved organic carbon during flushing in three small watersheds, Oregon, *Journal of Geophysical Research*, *111*(G1), doi:10.1029/2005jg000082.

Hope, D., S. M. Palmer, M. F. Billett, and J. J. Dawson (2001), Carbon dioxide and methane evasion from a temperate peatland stream, *Limnology and Oceanography*, *46*(4), 847–857, doi:10.4319/lo.2001.46.4.0847.

Hornberger, G. M., K. E. Bencala, and D. M. McKnight (1994), Hydrological controls on dissolved organic carbon during snowmelt in the Snake River near Montezuma, Colorado, *Biogeochemistry*, *25*(3), 147–165, doi:10.1007/bf00024390.

Hotchkiss, E. R., R. O. Hall Jr, R. A. Sponseller, D. Butman, J. Klaminder, H. Laudon, M. Rosvall, and J. Karlsson (2015), Sources of and processes controlling CO_2 emissions change with the size of streams and rivers, *Nature Geoscience*, 8: 696–699. doi:10.1038/ngeo2507

Huang, J., F. Yuan, G. Zeng, X. Li, Y. Gu, L. Shi, W. Liu, and Y. Shi (2017), Influence of pH on heavy metal speciation and removal from wastewater using micellar-enhanced ultrafiltration, *Chemosphere*, 173: 199–206. doi:10.1016/j.chemosphere.2016.12.137

Hunt, C. W., J. E. Salisbury, and D. Vandemark (2011), Contribution of non-carbonate anions to total alkalinity and overestimation of $p\mathrm{CO}_2$ in New England and New Brunswick rivers, *Biogeosciences*, 8: 3069–3076. doi:10.5194/bg-8-3069-2011

Illingworth, J. A. (1981), A common source of error in pH measurements, *Biochemical Journal*, 195: 259–262. doi:10.1042/bj1950259

IPCC (2022), Global warming of 1.5°C, doi:10.1017/9781009157940.

Jaffé, R., D. McKnight, N. Maie, R. Cory, W. H. McDowell, and J. L. Campbell (2008), Spatial and temporal variations in dom composition in ecosystems: The importance of long-term monitoring of optical properties, *Journal of Geophysical Research: Biogeosciences*, *113*(G4), doi:10.1029/2008jg000683.

Jansson, M., A.-K. Bergström, P. Blomqvist, and S. Drakare (2000), Allochthonous organic carbon and phytoplankton/bacterioplankton production relationships in Lakes, *Ecology*, *81*(11), 3250–3255, doi:10.1890/0012-9658(2000)081[3250:aocapb]2.0.co;2.

Jeong, J.-J., S. Bartsch, J.H. Fleckenstein, E. Matzner, J.D. Tenhunen, S.D. Lee, S.K. Park, and J.-H. Park (2012), Differential storm responses of dissolved and particulate organic carbon in a mountainous headwater stream, investigated by high-frequency, in situ optical measurements, *Journal of Geophysical Research: Biogeosciences*, *117*(G3), doi:10.1029/2012jg001999.

Johnson, M. S., M. F. Billett, K. J. Dinsmore, M. Wallin, K. E. Dyson, and R. S. Jassal (2009), Direct and continuous measurement of dissolved carbon dioxide in freshwater aquatic systems-method and applications, *Ecohydrology*, doi:10.1002/eco.95

Johnson, A. W. (2021), Development of a Novel In-Situ Chemical Sampler for Aquatic Systems, *Graduate Student Theses, Dissertations, & Professional Papers*. 11718. https://scholarworks.umt.edu/etd/11718

Jones, T. G., C. D. Evans, D. L. Jones, P. W. Hill, and C. Freeman (2016), Transformations in DOC along a source to sea continuum; impacts of photo-degradation, biological processes and mixing, *Aquatic Sciences*, *78*(3), 433–446, doi:10.1007/s00027-015-0461-0.

Junk, W. J., P. B. Bayley, and R. E. Sparks (1989), The Flood Pulse Concept in River-Floodplain Systems, *Canadian Special Publication of Fisheries and Aquatic Sciences*, *106*, 110–127.

Kadlec, R. H., and S. D. Wallace (2009), *Treatment wetlands*, CRC Press, Boca Raton, FL.

Kaplan, L. A., and T. L. Bott (1982), Diel fluctuations of DOC generated by algae in a Piedmont stream, *Limnology and Oceanography*, *27*(6), 1091–1100, doi:10.4319/lo.1982.27.6.1091.

Kanuri, V. V., D. R. Gijjapu, K. Munnooru, A. Sura, S. Patra, R. R. Vinjamuri, and R. Karri (2017), Scales and drivers of seasonal $p\mathrm{CO}_2$ dynamics and net ecosystem exchange along the coastal waters of southeastern Arabian Sea, *Marine Pollution Bulletin*, 121: 372–380. doi:10.1016/j.marpolbul.2017.06.016

Karlsson, J., S. Serikova, S. N. Vorobyev, G. Rocher-Ros, B. Denfeld, and O. S. Pokrovsky (2021), Carbon emission from Western Siberian Inland Waters, *Nature Communications*, *12*(1), doi:10.1038/s41467-021-21054-1.

Kaushal, S. S., and K. T. Belt (2012), The Urban Watershed Continuum: Evolving Spatial and temporal dimensions, *Urban Ecosystems*, *15*(2), 409–435, doi:10.1007/s11252-012-0226-7.

Khan, H., A. Laas, R. Marcé, M. Sepp, and B. Obrador (2021), Eutrophication and geochemistry drive pelagic calcite precipitation in lakes, *Water*, 13: 597. doi:10.3390/w13050597

Koenig, L. E., A. M. Helton, P. Savoy, E. Bertuzzo, J. B. Heffernan, R. O. Hall, and E. S. Bernhardt (2019), Emergent productivity regimes of River Networks, *Limnology and Oceanography Letters*, *4*(5), 173–181, doi:10.1002/lol2.10115.

Kyro, C. (2021), Nitrogen dynamics and transport along flowpaths in a rural wetland-stream complex, Division of Biological Sciences, Master's Thesis, University of Montana, Missoula, Montana.

Lai, C.-Z., M. D. DeGrandpre, B. D. Wasser, and others (2016), Spectrophotometric measurement of freshwater pH with purified meta-cresol purple and phenol red, *Limnology and Oceanography: Methods*, 15: 903–903. doi:10.1002/lom3.10210

Lewis, E., and D. W. R. Wallace (1998), Program developed for CO_2 system calculations, *ORNL/CDIAC-105, Carbon Dioxide Information Analysis Center, Oak Ridge National*

Laboratory, U.S. Department of Energy, Oak Ridge, Tennessee, doi:10.3334/CDIAC/otg.CO2SYS_DOS_CDIAC105

Li, M., C. Peng, M. Wang, W. Xue, K. Zhang, K. Wang, G. Shi, and Q. Zhu (2017), The Carbon Flux of Global Rivers: A re-evaluation of amount and spatial patterns, *Ecological Indicators*, *80*, 40–51, doi:10.1016/j.ecolind.2017.04.049.

Li, S., X. X. Lu, M. He, Y. Zhou, L. Li, and A. D. Ziegler (2012), Daily CO_2 partial pressure and CO_2 outgassing in the Upper Yangtze River Basin: A case study of the Longchuan River, China, *Journal of Hydrology*, *466-467*, 141–150, doi:10.1016/j.jhydrol.2012.08.011.

Li, X., M. I. García-Ibáñez, B. R. Carter, B. Chen, Q. Li, R. A. Easley, and W.-J. Cai (2020), Purified meta-cresol purple dye perturbation: How it influences spectrophotometric pH measurements, *Marine Chemistry*, 225: 103849. doi:10.1016/j.marchem.2020.103849

Liu, J., and G. Han (2021), Controlling factors of riverine CO_2 partial pressure and CO_2 outgassing in a large karst river under base flow condition, *Journal of Hydrology*, *593*, 125638, doi:10.1016/j.jhydrol.2020.125638.

Liu, S., D. E. Butman, and P. A. Raymond (2020), Evaluating CO_2 calculation error from organic alkalinity and pH measurement error in low ionic strength freshwaters, *Limnology and Oceanography: Methods*, 18: 606–622. doi:10.1002/lom3.10388

Liu, X., M. C. Patsavas, and R. H. Byrne (2011), Purification and characterization of meta-cresol purple for spectrophotometric seawater pH measurements, *Environmental Science & Technology*, 45: 4862–4868. doi:10.1021/es200665d

Liu, Z., C. Groves, D. Yuan, J. Meiman, G. Jiang, S. He, and Q. Li (2004), Hydrochemical variations during flood pulses in the south-west china peak cluster karst: Impacts of

$CaCO_3$–H_2O–CO_2 interactions, *Hydrological Processes*, *18*(13), 2423–2437, doi:10.1002/hyp.1472.

Lowry, C. S., J. S. Deems, S. P. Loheide II, and J. D. Lundquist (2010), Linking snowmelt-derived fluxes and groundwater flow in a high elevation meadow system, Sierra Nevada Mountains, California, *Hydrological Processes*, *24*(20), 2821–2833, doi:10.1002/hyp.7714.

Lueker, T. J., A. G. Dickson, and C. D. Keeling (2000), Ocean pCO_2 calculated from dissolved inorganic carbon, alkalinity, and equations for K_1 and K_2: validation based on laboratory measurements of CO_2 in gas and seawater at equilibrium, *Marine Chemistry*, 70: 105–119. doi:10.1016/s0304-4203(00)00022-0

Lynch, J. K., C. M. Beatty, M. P. Seidel, L. J. Jungst, and M. D. DeGrandpre (2010), Controls of riverine CO_2 over an annual cycle determined using direct, high temporal resolution pCO_2 measurements, *Journal of Geophysical Research*, 115. doi:10.1029/2009jg001132

Lynch, L. M., N. A. Sutfin, T. S. Fegel, C. M. Boot, T. P. Covino, and M. D. Wallenstein (2019), River channel connectivity shifts metabolite composition and dissolved organic matter chemistry, *Nature Communications*, *10*(1), doi:10.1038/s41467-019-08406-8.

Mallard, J., B. McGlynn, and T. Covino (2014), Lateral inflows, stream-groundwater exchange, and network geometry influence stream water composition, *Water Resources Research*, *50*(6), 4603–4623, doi:10.1002/2013wr014944.

Mann, C. J., and R. G. Wetzel (1995), Dissolved organic carbon and its utilization in a riverine wetland ecosystem, *Biogeochemistry*, *31*(2), doi:10.1007/bf00000941.

Mantoura, R. F. C., and E. M. S. Woodward (1983), Conservative behaviour of riverine dissolved organic carbon in the Severn Estuary: Chemical and geochemical implications, *Geochimica et Cosmochimica Acta*, *47*(7), 1293–1309, doi:10.1016/0016-7037(83)90069-8.

Martz, T. R., J. J. Carr, C. R. French, and M. D. DeGrandpre (2003), A submersible autonomous sensor for spectrophotometric pH measurements of natural waters, *Analytical Chemistry*, 75: 1844–1850. doi:10.1021/ac020568l

Mast, M. A., S. F. Murphy, D. W. Clow, C. A. Penn, and G. A. Sexstone (2016), Water-quality response to a high-elevation wildfire in the Colorado Front Range, *Hydrological Processes*, *30*(12), 1811–1823, doi:10.1002/hyp.10755.

McGuire, K. J., C. E. Torgersen, G. E. Likens, D. C. Buso, W. H. Lowe, and S. W. Bailey (2014), Network analysis reveals multiscale controls on Streamwater Chemistry, *Proceedings of the National Academy of Sciences*, *111*(19), 7030–7035, doi:10.1073/pnas.1404820111.

Middelburg, J. J. (2019), *Marine Carbon Biogeochemistry a primer for Earth System scientists*, Springer International Publishing, Cham.

Millero, F. J. (1979), The thermodynamics of the carbonate system in seawater, *Geochimica et Cosmochimica Acta*, 43: 1651–1661. doi:10.1016/0016-7037(79)90184-4

Minor, E. C., C. J. Tennant, and E. T. Brown (2019), A seasonal to interannual view of inorganic and organic carbon and pH in western Lake Superior, *Journal of Geophysical Research: Biogeosciences*, 124: 405–419. doi:10.1029/2018jg004664

Minshall, G. W. (1978), Autotrophy in stream ecosystems, *BioScience*, *28*(12), 767–771, doi:10.2307/1307250.

Montgomery, D. R. (1999), Process domains and the river continuum, *Journal of the American Water Resources Association*, *35*(2), 397–410, doi:10.1111/j.1752-1688.1999.tb03598.x.

Moore, J. N., and S. N. Luoma (1990), Hazardous wastes from large-scale metal extraction. A case study, *Environmental Science & Technology*, *24*(9), 1278–1285, doi:10.1021/es00079a001.

Moore, J. N., and H. W. Langner (2012), Can a river heal itself? natural attenuation of metal contamination in river sediment, *Environmental Science & Technology*, *46*(5), 2616–2623, doi:10.1021/es203810j.

Müller, B., J. S. Meyer, and R. Gächter (2015), Alkalinity regulation in calcium carbonate-buffered lakes, *Limnology and Oceanography*, 61: 341–352. doi:10.1002/lno.10213

Müller, J. D., B. Schneider, S. Aßmann, and G. Rehder (2017), Spectrophotometric pH measurements in the presence of dissolved organic matter and hydrogen sulfide, *Limnology and Oceanography: Methods*, 16: 68–82. doi:10.1002/lom3.10227

Nagorski, S. A. (2001), Spatial and temporal variations in the geochemistry of several western Montana streams and rivers, *Graduate Student Theses, Dissertations, & Professional Papers*, 9408, https://scholarworks.umt.edu/etd/9408

Neal, C., W. House, H. Jarvie, and A. Eatherall (1998), The significance of dissolved carbon dioxide in major lowland rivers entering the North Sea, *Science of The Total Environment*, *210-211*, 187–203, doi:10.1016/s0048-9697(98)00012-6.

Olid, C., V. Rodellas, G. Rocher-Ros, J. Garcia-Orellana, M. Diego-Feliu, A. Alorda-Kleinglass, D. Bastviken, and J. Karlsson (2022), Groundwater discharge as a driver of methane emissions from Arctic Lakes, , doi:10.5194/egusphere-egu22-12622.

Oren, R. A. M., C. -I. Hsieh, P. Stoy, J. Albertson, H. R. McCarthy, P. Harrell, and G. G. Katul (2006), Estimating the uncertainty in annual net ecosystem carbon exchange: spatial variation in turbulent fluxes and sampling errors in eddy-covariance measurements, *Global Change Biology*, 12: 883–896. doi:10.1111/j.1365-2486.2006.01131.x

Oviedo-Vargas, D., M. Peipoch, and C. Dow (2022), Metabolism and soil water viscosity control diel patterns of nitrate and doc in a low order temperate stream, *Journal of Geophysical Research: Biogeosciences*, *127*(5), doi:10.1029/2021jg006640.

Pagano, T., M. Bida, and J. Kenny (2014), Trends in levels of allochthonous dissolved organic carbon in natural water: A review of potential mechanisms under a changing climate, *Water*, *6*(10), 2862–2897, doi:10.3390/w6102862.

Parker, S. R., C. H. Gammons, S. R. Poulson, and M. D. DeGrandpre (2007), Diel variations in stream chemistry and isotopic composition of dissolved inorganic carbon, upper Clark Fork River, Montana, USA, *Applied Geochemistry*, 22: 1329–1343. doi:10.1016/j.apgeochem.2007.02.007

Parker, S.R., S.R. Poulson, M.G. Smith, C.L. Weyer, and K.M. Bates (2010), Temporal variability in the concentration and stable carbon isotope composition of dissolved inorganic and organic carbon in two Montana, USA Rivers, *Aquatic Geochemistry*, *16*(1), 61–84, doi:10.1007/s10498-009-9068-1.

Parkhurst, D. L., and C. A. J. Appelo (2013), Description of input and examples for PHREEQC version 3: a computer program for speciation, batch-reaction, one-dimensional transport, and inverse geochemical calculations, *Techniques and Methods*, doi:10.3133/tm6a43

Peipoch, M., E. Gacia, E. Bastias, A. Serra, L. Proia, M. Ribot, S. N. Merbt, and E. Martí (2016), Small-scale heterogeneity of microbial N uptake in streams and its implications at the ecosystem level, *Ecology*, *97*(5), 1329–1344, doi:10.1890/15-1210.1.

Peter, H., G. A. Singer, C. Preiler, P. Chifflard, G. Steniczka, and T. J. Battin (2014), Scales and drivers of temporal $p\mathrm{CO}_2$ dynamics in an Alpine stream, *Journal of Geophysical Research: Biogeosciences*, 119: 1078–1091. doi:10.1002/2013jg002552

Phillips, J., G. McKinley, V. Bennington, H. Bootsma, D. Pilcher, R. Sterner, and N. Urban (2015), The potential for CO_2-induced acidification in freshwater: A Great Lakes case study, *Oceanography*, 25: 136–145. doi:10.5670/oceanog.2015.37

Phlips, E. J., J. Hendrickson, E. L. Quinlan, and M. Cichra (2007), Meteorological influences on algal bloom potential in a nutrient-rich Blackwater River, *Freshwater Biology*, *52*(11), 2141–2155, doi:10.1111/j.1365-2427.2007.01844.x.

Plummer, L. N., and E. Busenberg, (1982), The solubilities of calcite, aragonite and vaterite in CO_2-H_2O solutions between 0 and 90°C, and an evaluation of the aqueous model for the system $CaCO_3$-CO_2-H_2O, *Geochimica et Cosmochimica Acta*, 46: 1011–1040. doi:10.1016/0016-7037(82)90056-4

Raymond, P. A., N. F. Caraco, and J. J. Cole (1997), Carbon dioxide concentration and atmospheric flux in the Hudson River, *Estuaries*, 20: 381. doi:10.2307/1352351

Raymond, P. A., J. E. Bauer, and J. J. Cole (2000), Atmospheric CO_2 evasion, dissolved inorganic carbon production, and net heterotrophy in the York River estuary, *Limnology and Oceanography*, 45: 1707–1717. doi:10.4319/lo.2000.45.8.1707

Raymond, P. A., and J. E. Bauer (2001), Riverine export of aged terrestrial organic matter to the North Atlantic Ocean, *Nature*, *409*(6819), 497–500, doi:10.1038/35054034.

Raymond, P. A., C. J. Zappa, D. Butman, and others (2012), Scaling the gas transfer velocity and hydraulic geometry in streams and small rivers, *Limnology and Oceanography: Fluids and Environments*, 2: 41–53. doi:10.1215/21573689-1597669

Raymond, P. A., J. Hartmann, R. Lauerwald, and others (2013), Global carbon dioxide emissions from inland waters, *Nature*, 503: 355–359. doi:10.1038/nature12760

Raymond, P. A., J. E. Saiers, and W. V. Sobczak (2016), Hydrological and biogeochemical controls on watershed dissolved organic matter transport: Pulse-shunt concept, *Ecology*, *97*(1), 5–16, doi:10.1890/14-1684.1.

Richey, J. E., J. M. Melack, A. K. Aufdenkampe, V. M. Ballester, and L. L. Hess (2002), Outgassing from Amazonian rivers and wetlands as a large tropical source of atmospheric CO_2, *Nature*, *416*(6881), 617–620, doi:10.1038/416617a.

Rocher-Ros, G., R. A. Sponseller, W. Lidberg, C. M. Mörth, and R. Giesler (2019), Landscape process domains drive patterns of CO_2 evasion from river networks, *Limnology and Oceanography Letters*, 4: 87–95. doi:10.1002/lol2.10108

Rocher-Ros, G., R. A. Sponseller, A. K. Bergström, M. Myrstener, and R. Giesler (2020), Stream metabolism controls diel patterns and evasion of CO_2 in Arctic streams, *Global Change Biology*, 26: 1400–1413. doi:10.1111/gcb.14895

Rocher-Ros, G., T. K. Harms, R. A. Sponseller, M. Väisänen, C. M. Mörth, and R. Giesler (2021), Metabolism overrides photo-oxidation in CO_2 dynamics of Arctic permafrost streams, *Limnology and Oceanography*, 66. doi:10.1002/lno.11564

Schmidt, T. S., W. H. Clements, K. A. Mitchell, S. E. Church, R. B. Wanty, D. L. Fey, P. L. Verplanck, and C. A. San Juan (2010), Development of a new toxic-unit model for the bioassessment of metals in streams, *Environmental Toxicology and Chemistry*, *29*(11), 2432–2442, doi:10.1002/etc.302.

Seidel, M. P., M. D. DeGrandpre, and A. G. Dickson (2008), A sensor for in situ indicator-based measurements of seawater pH, *Marine Chemistry*, 109: 18–28. doi:10.1016/j.marchem.2007.11.013

Shangguan, Q., C. Z. Lai, C. M. Beatty, F. L. Young, R. S. Spaulding, and M. D. DeGrandpre (2021), Autonomous in situ measurements of freshwater alkalinity, *Limnology and Oceanography: Methods*, 19: 51–66. doi:10.1002/lom3.10404

Shogren, A. J., J. P. Zarnetske, B. W. Abbott, F. Iannucci, A. Medvedeff, S. Cairns, M. J. Duda, and W. B. Bowden (2021), Arctic concentration–discharge relationships for dissolved organic carbon and nitrate vary with landscape and season, *Limnology and Oceanography*, *66*(S1), doi:10.1002/lno.11682.

Soares, M., E. S. Kritzberg, and J. Rousk (2017), Labile carbon 'primes' fungal use of nitrogen from submerged leaf litter, *FEMS Microbiology Ecology*, *93*(9), doi:10.1093/femsec/fix110.

Spencer, R. G., B. A. Pellerin, B. A. Bergamaschi, B. D. Downing, T. E. Kraus, D. R. Smart, R. A. Dahlgren, and P. J. Hernes (2007), Diurnal variability in riverine dissolved organic matter composition determined byin situ optical measurement in the San Joaquin River (California, USA), *Hydrological Processes*, *21*(23), 3181–3189, doi:10.1002/hyp.6887.

Spencer, R. G., G. R. Aiken, K. P. Wickland, R. G. Striegl, and P. J. Hernes (2008), Seasonal and spatial variability in dissolved organic matter quantity and composition from the Yukon River Basin, Alaska, *Global Biogeochemical Cycles*, *22*(4), doi:10.1029/2008gb003231.

Stanley, E. H., S. M. Powers, N. R. Lottig, I. Buffam, and J. T. Crawford (2012), Contemporary changes in dissolved organic carbon (DOC) in human-dominated rivers: Is there a role for

DOC Management?, *Freshwater Biology*, *57*, 26–42, doi:10.1111/j.1365-2427.2011.02613.x.

Stauffer, R. E. (1990), Electrode pH error, seasonal epilimnetic $p\mathrm{CO_2}$, and the recent acidification of the Maine lakes, *Water, Air, and Soil Pollution*, 50. doi:10.1007/bf00284788

Stets, E. G., D. Butman, C. P. McDonald, S. M. Stackpoole, M. D. DeGrandpre, and R. G. Striegl (2017), Carbonate buffering and metabolic controls on carbon dioxide in rivers, *Global Biogeochemical Cycles*, 31: 663–677. doi:10.1002/2016gb005578

Stumm, W., and J. J. Morgan (2008), Aquatic chemistry, Wiley.

Takahashi, T. et al. (2002), Global sea–air $\mathrm{CO_2}$ flux based on climatological surface ocean $p\mathrm{CO_2}$, and seasonal biological and temperature effects, *Deep Sea Research Part II: Topical Studies in Oceanography*, *49*(9-10), 1601–1622, doi:10.1016/s0967-0645(02)00003-6.

Takeshita, Y., K. S. Johnson, L. J. Coletti, H. W. Jannasch, P. M. Walz, and J. K. Warren (2020), Assessment of pH dependent errors in spectrophotometric pH measurements of seawater, *Marine Chemistry*, 223: 103801. doi:10.1016/j.marchem.2020.103801

Tank, J. L. et al. (2018), Partitioning assimilatory nitrogen uptake in streams: An analysis of stable isotope tracer additions across continents, *Ecological Monographs*, *88*(1), 120–138, doi:10.1002/ecm.1280.

Telmer, K., and J. Veizer (1999), Carbon fluxes, $p\mathrm{CO_2}$ and substrate weathering in a large Northern River Basin, Canada: Carbon Isotope Perspectives, *Chemical Geology*, *159*(1-4), 61–86, doi:10.1016/s0009-2541(99)00034-0.

Thorp, J. H., and M. D. Delong (1994), The riverine productivity model: An heuristic view of carbon sources and organic processing in large river ecosystems, *Oikos*, *70*(2), 305, doi:10.2307/3545642.

Thorp, J. H., and M. D. Delong (2002), Dominance of autochthonous autotrophic carbon in food webs of Heterotrophic Rivers, *Oikos*, *96*(3), 543–550, doi:10.1034/j.1600-0706.2002.960315.x.

Tockner, K., D. Pennetzdorfer, N. Reiner, F. Schiemer, and J. V. Ward (1999), Hydrological connectivity, and the exchange of organic matter and nutrients in a Dynamic River-floodplain system (Danube, Austria), *Freshwater Biology*, *41*(3), 521–535, doi:10.1046/j.1365-2427.1999.00399.x.

Tunaley, C., D. Tetzlaff, J. Lessels, and C. Soulsby (2016), Linking high-frequency Doc Dynamics to the age of connected water sources, *Water Resources Research*, *52*(7), 5232–5247, doi:10.1002/2015wr018419.

Uehlinger, U. (2006), Annual cycle and inter-annual variability of gross primary production and ecosystem respiration in a floodprone river during a 15-year period, *Freshwater Biology*, *51*(5), 938–950, doi:10.1111/j.1365-2427.2006.01551.x.

Ulseth, A. J., R. O. Hall, M. Boix Canadell, H. L. Madinger, A. Niayifar, and T. J. Battin (2019), Distinct air–water gas exchange regimes in low- and high-energy streams, *Nature Geoscience*, *12*(4), 259–263, doi:10.1038/s41561-019-0324-8.

U.S. EPA (2005), Method 415.3: Measurement of total organic carbon, dissolved organic carbon, and specific UV absorbance at 254 nm in source water and drinking water, *Environmental Monitoring Systems Laboratory*, Office of Research and Development.

Valett, H. M., M. Peipoch, and G. C. Poole (2022), Nutrient processing domains: Spatial and temporal patterns of material retention in running waters, *Freshwater Science*, doi:10.1086/719991.

Vannote, R. L., G. W. Minshall, K. W. Cummins, J. R. Sedell, and C. E. Cushing (1980), The River Continuum Concept, *Canadian Journal of Fisheries and Aquatic Sciences*, *37*(1), 130–137, doi:10.1139/f80-017.

Vaughan, M. C. et al. (2017), High-frequency dissolved organic carbon and nitrate measurements reveal differences in storm hysteresis and loading in relation to land cover and seasonality, *Water Resources Research*, *53*(7), 5345–5363, doi:10.1002/2017wr020491.

Wang, F., B. Wang, C.-Q. Liu, Y. Wang, J. Guan, X. Liu, and Y. Yu (2011), Carbon dioxide emission from surface water in Cascade Reservoirs–river system on the maotiao river, southwest of China, *Atmospheric Environment*, *45*(23), 3827–3834, doi:10.1016/j.atmosenv.2011.04.014.

Wang, Z. A., and W.-J. Cai (2004), Carbon dioxide degassing and inorganic carbon export from a marsh-dominated estuary (the Duplin River): A marsh CO_2 pump, *Limnology and Oceanography*, 49: 341–354. doi:10.4319/lo.2004.49.2.0341

Wang, Z. A., H. Moustahfid, A. V. Mueller, and others (2019), Advancing observation of ocean biogeochemistry, biology, and ecosystems with cost-effective in situ sensing technologies, *Frontiers in Marine Science*, 6. doi:10.3389/fmars.2019.00519

Wang, Z., J. P. Meador, and K. M. Y. Leung (2016), Metal toxicity to freshwater organisms as a function of pH: A meta-analysis, *Chemosphere*, 144: 1544–1552. doi:10.1016/j.chemosphere.2015.10.032

Weiss, R. F. (1974), Carbon dioxide in water and seawater: The solubility of a non-ideal gas, *Marine Chemistry*, 2: 203–215. doi:10.1016/0304-4203(74)90015-2

Westerhoff, P., and D. Anning (2000), Concentrations and characteristics of organic carbon in surface water in Arizona: Influence of Urbanization, *Journal of Hydrology*, *236*(3-4), 202–222, doi:10.1016/s0022-1694(00)00292-4.

Westhorpe, D. P., S. M. Mitrovic, D. Ryan, and T. Kobayashi (2010), Limitation of lowland riverine bacterioplankton by dissolved organic carbon and inorganic nutrients, *Hydrobiologia*, *652*(1), 101–117, doi:10.1007/s10750-010-0322-8.

Wilcock, R. J., and S. C. Chapra (2005), Diel changes of inorganic chemistry in a macrophyte-dominated, softwater stream, *Marine and Freshwater Research*, 56: 1165. doi:10.1071/mf05049

Worrall, F., and A. Lancaster (2005), The release of CO_2 from river waters – The contribution of excess CO_2 from groundwater, *Biogeochemistry*, *76*(2), 299–317, doi:10.1007/s10533-005-6449-4.

Yang, B., M. C. Patsavas, R. H. Byrne, and J. Ma (2014), Seawater pH measurements in the field: A DIY photometer with 0.01 unit pH accuracy, *Marine Chemistry*, 160: 75–81. doi:10.1016/j.marchem.2014.01.005

Yao, W., and R. H. Byrne (2001), Spectrophotometric determination of freshwater pH using bromocresol purple and phenol red, *Environmental Science & Technology*, 35: 1197–1201. doi:10.1021/es001573e

Yarnell, S., R. Peek, G. Epke, and A. Lind (2016), Management of the spring snowmelt recession in regulated systems, *JAWRA Journal of the American Water Resources Association*, *52*(3), 723–736, doi:10.1111/1752-1688.12424.

Young, F. L., Q. Shangguan, C. M. Beatty, M. D. Gilsdorf, and M. D. DeGrandpre (2022), Comparison of spectrophotometric and electrochemical pH measurements for calculating freshwater $p\mathrm{CO}_2$, *Limnology and Oceanography: Methods*, *20*(8), 514–529, doi:10.1002/lom3.10501.

Yuan, S., and M. D. DeGrandpre. 2008. Evaluation of indicator-based pH measurements for freshwater over a wide range of buffer intensities. Environmental Science & Technology **42**: 6092–6099. doi:10.1021/es800829x

Zou, J. (2017), Geochemical characteristics and organic carbon sources within the upper reaches of the Xi River, Southwest China during high flow, *Journal of Earth System Science*, *126*(1), doi:10.1007/s12040-016-0792-9.